EONS: A new biogeochemical model of Earth's oxygen, carbon, phosphorus, and nitrogen systems from the Archean to the present

J. E. Horne, & C. Goldblatt

2024

Geochemistry, Geophysics, Geosystems®

AGU ADVANCING EARTH AND SPACE SCIENCES

RESEARCH ARTICLE
10.1029/2023GC011252

EONS: A New Biogeochemical Model of Earth's Oxygen, Carbon, Phosphorus, and Nitrogen Systems From the Archean to the Present

J. E. Horne[1] and **C. Goldblatt**[1]

[1]School of Earth and Ocean Sciences, University of Victoria, Victoria, BC, Canada

Key Points:

- The first fully coupled evolutionary C-N-O-P box model spanning all major eons produces a surface oxygenation curve consistent with proxies
- The biosphere is a primary driver of Earth system evolution; increasing organic carbon burial and nutrient sequestration delay oxygen's rise
- The chemical composition of the atmosphere-ocean is never in steady state, due to the long timescales of geological and stellar evolution

Correspondence to:

J. E. Horne,
juliahorne@uvic.ca

Citation:

Horne, J. E., & Goldblatt, C. (2024). EONS: A new biogeochemical model of Earth's oxygen, carbon, phosphorus, and nitrogen systems from the Archean to the present. *Geochemistry, Geophysics, Geosystems*, *25*, e2023GC011252. https://doi.org/10.1029/2023GC011252

Received 25 SEP 2023
Accepted 7 FEB 2024

Abstract We present Earth's Oxygenation and Natural Systematics (EONS): a new, fully coupled biogeochemical model of the atmosphere, ocean, and their interactions with the geosphere, which can reproduce major features of Earth's evolution following the origin of life to the present day. The model, consisting of 257 unique fluxes between 96 unique chemical reservoirs, includes an interactive biosphere, cycles of carbon, nitrogen, phosphorus, and oxygen, and climate. A nominal model run initialized in the Eoarchean resolves emergent surface oxygenation, nutrient limitations, and climate feedbacks. The modeled atmosphere oxygenates in stepwise fashion over the course of the Proterozoic; a nearly billion year lag after the evolution of photosynthesis at 3.5 Ga is followed by a great oxidation event at 2.4 Ga, which appears to be caused by the gradual buildup of organic matter on the continents imposing nutrient limitation on the biosphere by removing key nutrients from the ocean system. The simple climate system shows significant temperature shifts punctuate the oxygenation process, implying that major biological transitions possibly destabilized Earth's climate. This work demonstrates that forward modeling the entirety of Earth's history with relatively few imposed boundary forcings is feasible, that the Earth system is not at steady state, and that our understanding of coupled C-N-P-O cycling as it functions today can explain much of the Earth's evolution.

Plain Language Summary The Earth is an interconnected system of biological, geological, and atmosphere-ocean chemical systems responding to and influencing one another. We have developed a new model of our planet's chemical evolution, Earth's Oxygenation and Natural Systematics (EONS); this first of its kind model encompasses the entire lifetime of Earth's biosphere and major evolutionary developments therein, including the emergence of oxygen producing organisms and the colonization of continents by plants. Our basic (nominal) model run, starting 4 billion years ago and allowing biogeochemical systems to dynamically evolve until the modern day, agrees with geochemical evidence for rising atmospheric oxygen in magnitude and timing. It successfully reproduces atmosphere-ocean chemistry and geologic systems in the modern context. Model output implies that the delay in oxygen's rise after the evolution of photosynthesis is caused by gradual burial of organic matter onto continents, depriving biological systems of key nutrients. Results also suggest that developments in the biosphere significantly disrupted Earth's climate. This model is a significant step forward in using coupled systematics to describe Earth's long-term evolution. This work demonstrates that our planet is an immensely intertwined web of chemical relationships in a constant state of change, but one that can be fundamentally disentangled and understood.

1. Introduction

The Earth has managed to maintain astonishing habitability through 4.5 billion years of existence, albeit with dramatically disruptive moments. Two major theories emerged to explain this observation, both of which color the following work: First, the *Gaia* hypothesis posited long-term climate and carbon system stabilization caused by biological feedbacks; an "adaptive control system to maintain the Earth in homeostasis" (Lovelock, 1972; Lovelock & Margulis, 1974). Second, the coupling between atmospheric carbon dioxide, temperature, and continental silicate weathering, wherein increases to atmospheric CO_2 and surface temperature enhance mineral dissolution and continental weathering in a process that sequesters carbon from the atmosphere as carbonate minerals (the WHAK feedback; Walker et al., 1981). In the decades since the development of these theories for Earth's evolution, models attempting to recreate the Earth system have continued to grow in complexity and in breadth of systems involved, yet all of these models are fundamentally in agreement: the Earth system as we understand it is the result of multifarious intertwined biological, geological, and climatic systems.

Modeling the Earth system in all its complexity is difficult. There has been significant focus on modeling oxygen and carbon systems through the Phanerozoic eon (Bergman et al., 2004; Berner, 2009; Lenton et al., 2018; Zeebe, 2012) where the geologic record is quite robust, with some models covering the Proterozoic (Alcott et al., 2019; Fennel et al., 2005) and Archean (Claire et al., 2006; Kharecha et al., 2005) where records are much more sparse. Higher resolution biogeochemical box models of the coupled C-N-O-P-S systems resolve ocean chemical evolution with over geologic timescales, but exclude mantle-surface interactions and anaerobic cycles applicable to the Archean (Ozaki et al., 2022). Models spanning Earth's history since the Hadean (Tajika & Matsui, 1990, 1992) have successfully resolved inorganic carbon cycle feedbacks and mantle volatile degassing, but do not include the biosphere. These models are broadly similar in form; they generally utilize fixed fluxes and numerous external forcings to evolve their chosen systems. All have added to the growing wealth of knowledge regarding the ultimate controls on Earth's evolutionary trajectory. None have recreated the coupled evolution of biotic and abiotic systems over the 4 billion years since life emerged.

Our modeling philosophy is to dynamically evolve the Earth system through time by including as many feedbacks as possible and by imposing as few external forcings as possible. The resulting Earth oxygenation and natural systematics (EONS) model is a first of its kind, fully coupled interactive biogeochemical box model of the evolution of the surface through the majority of Earth's history. We employ a forward modeling approach similar to that of the COPSE model (Bergman et al., 2004) but starting from Eoarchean conditions and using limited external forcings mainly focused on biosphere evolutionary transitions. The exchange of mass between the modeled atmosphere-ocean and geosphere reservoirs is described by fluxes in units of moles per year for the major elements we track (C, N, P, O, Fe, H) progressing the system of coupled ordinary differential equations (ODEs) through time into the preindustrial contemporary period. The entire model consists of 257 unique fluxes between 96 unique chemical reservoirs; our code is open source (see the Open Research section).

This manuscript is organized in the following manner: We provide a comprehensive description of the model components in Section 2. We present a nominal run of the EONS model and discuss the implications of output in Section 3. We present our conclusions and discuss uncertainties in Section 4.

2. Materials and Methods

The model description section is organized into the following subsections:

1. Conventions and notation
2. Reservoirs, species, and structure
3. Boundary forcings
4. Fluxes
   (a) Biosphere
   (b) Atmosphere-ocean chemistry
   (c) Geosphere
   (d) Mass movement
5. Climate
6. Differential equations and implementation
7. Initial conditions

As with any conceptual model of Earth system evolution, numerous assumptions and simplifications have been made. We explain these wherever possible through this section, and consider specific consequences in the results (Section 3). However, several underpinning assumptions are implicit in our judgment of what to include or exclude (Section 4.1); realistic limitations on the scope of the first version of a new model mean that not every cycle, process, or record can be included. For example,: we neglect the sulfur cycle, even though we know that to be important; we do not output carbon or nitrogen isotope records from the model, even though these would be a useful constraint; and most mantle processes are omitted. We anticipate these will be included in future versions of EONS.

2.1. Conventions and Notation

Our notation uses subscripts indicating x flux name, j for species, and i for reservoir. Fluxes are represented $F_{x,j,i}$ in units of mol/yr. Fluxes affecting only one or two species or occurring only in one reservoir drop the j and i terms.

Fluxes sensitive to environmental conditions or availability of reactants include half-saturation limitations, $L_{x,j,i}$, defined:

$$L_{x,j,i} = \frac{[j]_i}{[j]_i + k_{x,j}} \tag{1}$$

for half-saturation uptake values, $k_{\mathrm{x,j}}$ (Table A3).

Reservoirs are denoted by $R_{j,i}$ in units of moles. Reference sizes for reservoirs (typically modern) are denoted $R_{j,i,0}$ (Table A3). Timescales are denoted by τ_x and are in units of years.

Fractions, denoted by f_x or f_j, range between 0 and 1. The atmospheric fraction of certain species, particularly O_2 and CO_2, are measured in units of present atmospheric levels (PAL), defined by the model reservoir over the modern day reservoir:

$$f_j = \frac{R_{j,\mathrm{a}}}{R_{j,\mathrm{a},0}} \tag{2}$$

We do not use the f_j notation (i.e., f_{O_2}) to denote fugacity.

Multiples of modern day values (which may exceed 1) are χ_x, and are used to denote forcings in this model.

2.2. Reservoirs, Species, and Structure

The EONS model quantifies the transfer of carbon, nitrogen, oxygen, and phosphorus species between relevant biological and geological reservoirs on the Earth. The reservoirs are: (a) atmosphere, *a*; (b) surface ocean, *s*; (c) continental shelf (neritic) reactive sediments, *n*; (d) deep ocean, *d*; (e) pelagic reactive sediments, *z*; (f) unreactive sediments, *u*; (g) ocean crust, *o*; (h) continents, *c*; and (i) mantle, *m*.

Species are included in Table 1. We assume that charged nutrient species (i.e., NO_3^- and PO_4^{3-}) are assimilated in association with protons by primary producers to maintain electro-neutrality within their cells following the "nutrient-H^+–compensation principle" as described by Wolf-Gladrow et al. (2007).

Organic carbon (OC), nitrogen, and phosphorus are contained within a single molecule in Redfield ratio (106:16:1; see Section 2.4.1). We track these species in individual reservoirs as phosphate may vary from this ratio in sediments because of scavenging by decomposers in P-limited conditions (see Section 2.5.6). Organic C, N, and P also experience different effects of volcanism and metamorphism (see Sections 2.6.2.2 and 2.6.3), requiring more precise accounting in geologic boxes.

2.2.1. Nitrogen and Carbon Speciation

Reservoirs in the ocean boxes (*s* and *d*) as well as in the shelf and deep reactive sediments (*n* and *z*) for dissolved inorganic carbon (DIC), total alkalinity (TA), and reduced nitrogen (RN) are "aggregate" reservoirs, consisting of several species.

2.2.1.1. RN

Reduced nitrogen includes ammonium and ammonia in equilibrium.

$$NH_4^+ \rightleftharpoons NH_3 + H^+ \tag{3}$$

2.2.1.2. DIC

The DIC reservoir includes carbon dioxide, bicarbonate, and carbonate in equilibrium:

$$[\mathrm{DIC}] = [CO_2] + [HCO_3^-] + [CO_3^{2-}] \tag{4}$$

$$CO_2 + H_2O \rightleftharpoons H^+ + HCO_3^- \rightleftharpoons 2H^+ + CO_3^{2-} \tag{5}$$

Table 1
Model Species Summary

Species	Stochiometry	Reservoirs								
		a	*s*	*n*	*d*	*z*	*u*	*o*	*c*	*m*
Ammonia, organic nitrogen (ON)	NH_3	✓	✓	✓	✓	✓	✓		✓	
Ammonium	NH_4^+		✓	✓	✓	✓		✓	✓	✓
Total reduced nitrogen (RN)	$NH_3 + NH_4^+$		✓	✓	✓	✓				
Nitrate	HNO_3		✓	✓	✓	✓				
Dinitrogen	N_2	✓	✓	✓	✓	✓				
Carbon dioxide	CO_2	✓								
Methane	CH_4	✓	✓	✓	✓	✓				
Dissolved inorganic carbon (DIC)	$CO_2 + HCO_3^- + CO_3^{2-}$		✓	✓	✓	✓				
Total alkalinity (TA)	Equation 6		✓	✓	✓	✓				
Calcium carbonate	$CaCO_3$		✓	✓	✓	✓	✓	✓	✓	✓
Organic carbon (OC), living biomass (LB)	CH_2O		✓	✓	✓	✓	✓		✓	
Phosphoric acid, organic phosphorus (OP)	H_3PO_4		✓	✓	✓	✓		✓		
Carbonate- and silicate-bound phosphate (CP, SP)	H_3PO_4						✓		✓	✓
Oxygen	O_2	✓	✓	✓	✓	✓				
Ferrous iron	FeO		✓		✓					✓
Fayalite olivine	Fe_2SiO_4								✓	✓
Iron hydroxide	$Fe(OH)_3$		✓	✓	✓	✓	✓	✓	✓	
Fe(III)-phosphate	$FePO_4$		✓	✓	✓	✓				
Hematite	Fe_2O_3								✓	
Silicates	SiO_3								✓	✓
Water	H_2O	✓	✓	✓	✓	✓				

Note. A list of all of the species within the EONS model, and the reservoir boxes which they inhabit.

2.2.1.3. TA

TA reservoirs track the net anion concentration of an ocean/sediment box. Given the species tracked in the model, we adapt the explicitly conservative definition of TA from Dickson (1981) to include ammonia:

$$[TA] = [HCO_3^-] + 2[CO_3^{2-}] + [B(OH)_4^-] + [OH^-] + [NH_3] - [H^+] \quad (6)$$

In reality, phosphorus species are also included in the definition of alkalinity; as we only track one such species in this model (H_3PO_4), and since phosphorus species are relatively minor constituents in the TA balance in ocean waters, we ignore alkalinity effects from phosphorus reactions. All species, with the exception of $B(OH)_4^-$, are tracked with explicit aggregate reservoirs in the model; for total dissolved borate, we assume a constant oceanic concentration $\left([B_T]_i\right)$ according to box salinity, also constant (approximately 35‰; Zeebe & Wolf-Gladrow, 2001). Ocean salinity likely varied throughout geologic time (Albarede et al., 2020; Catling & Zahnle, 2020) and higher salinity could have contributed to a warm Archean climate (S. Olson et al., 2022). However, estimates of salinity for this period are unconstrained and modeling the evolution of ocean salinity is beyond the scope of this current work.

2.2.1.4. Equilibrium Speciation

The concentration of any species at a given time depends on the pH of the reservoir. Concentrations of the three carbon species as well as the two nitrogen species are found according to concentrations of hydrogen and hydroxyl ions ($[H^+]$ and $[OH^-]$) in each ocean and sediment box *i*.

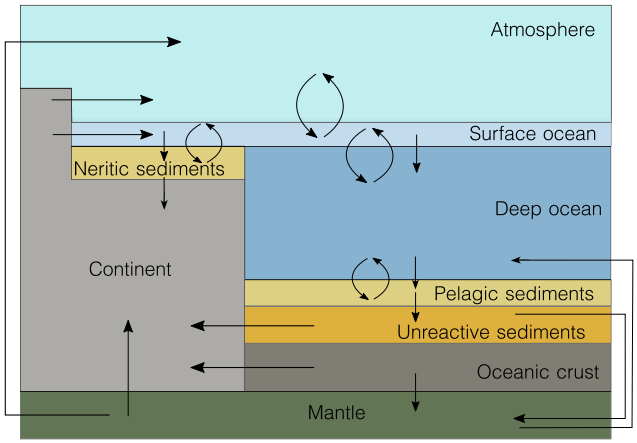

Figure 1. Model schematic. Schematic representation of the EONS model structure. Arrows denote direct reservoir interaction via fluxes.

$$[OH^-]_i = \frac{K_{W,i}}{[H^+]_i} \tag{7}$$

$$[CO_2]_i = \frac{[DIC]_i}{\left(1 + \frac{K_{1,i}}{[H^+]_i} + \frac{K_{1,i}K_{2,i}}{[H^+]_i^2}\right)} \tag{8}$$

$$[CO_3^{2-}]_i = \frac{[DIC]_i}{\left(1 + \frac{[H^+]_i}{K_{2,i}} + \frac{[H^+]_i^2}{K_{1,i}K_{2,i}}\right)} \tag{9}$$

$$[HCO_3^-]_i = \frac{[DIC]_i}{\left(1 + \frac{[H^+]_i}{K_{1,i}} + \frac{K_{2,i}}{[H^+]_i}\right)} \tag{10}$$

$$[NH_3]_i = \frac{[RN]_i}{\left(1 + \frac{[H^+]_i}{K_{N,i}}\right)} \tag{11}$$

$$[NH_4^+]_i = \frac{[NH_3]_i[H^+]_i}{K_{N,i}} \tag{12}$$

This system is solved using a sixth-order polynomial equation for the single set of positive roots, resolving the hydrogen concentration of box i (see Appendix B2). This polynomial has been modified from the fifth-order polynomial equation of Zeebe and Wolf-Gladrow (2001) in order to include the effects of ammonia-ammonium equilibrium on TA. The acid dissociation constants for protonation, hydration, boric acid, ion water product, and ammonia (K_1, K_2, K_B,K_W, and K_N, respectively) for these equations are functions of water salinity (S_i) and temperature (T_i; Zeebe & Wolf-Gladrow, 2001).

2.2.2. Model Structure

The EONS model is schematically represented in Figure 1. The modeled ocean system is split into four reservoirs: surface ocean, deep ocean, neritic (shelf) sediments, and pelagic sediments. The surface ocean includes the euphotic zone (100 m depth) above the deep ocean, as well as the ocean overlying the continental shelf. The midpoint pressure of the surface ocean box is set at 5 bars (a full depth 100 m), while the deep ocean reservoir has a pressure of 200 bars (full depth of 4 km). In the reactive sediments, pressure is assumed to be equivalent to the overlying ocean box (10 bars for n, 400 bars for z). Two box ocean models perform poorly in simultaneously reproducing phosphorus and oxygen concentrations in the modern ocean, which are well constrained (Sarmiento & Gruber, 2006); however, a two box ocean is sufficient for simulating generalized global concentrations for these dissolved species and this bias does not appear to strongly affect our results.

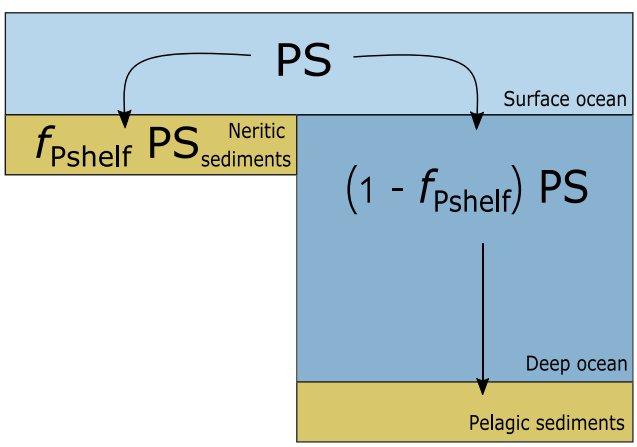

Figure 2. Shelf schematic. Schematic representation of how export and sedimentation of particulate species *PS* (organic matter, $CaCO_3$, or $Fe(OH)_3$) is apportioned using the f_{PShelf} fraction.

The most productive portion of the surface ocean covers the continental shelf. Although the shelf occupies a small, fixed fraction of the overall ocean surface area ($f_{Ashelf} = 0.08$) it hosts an outsized portion of total surface ocean productivity ($f_{Pshelf} = 0.3$; Yool & Fasham, 2001). Thus, the apportionment of biologically mediated particulate species (organic matter (OM), $CaCO_3$, and $Fe(OH)_3$ formed as a byproduct of photo-ferrotrophy) sinking out of the surface ocean into the shelf sediments or to deep ocean is controlled by this productivity fraction (see Figure 2).

2.3. Boundary Forcings

The EONS model evolves according to several time-dependent, imposed boundary forcings. These include mantle reductant outflux, continental erosion (emergence), solar flux, the evolution of oxygenic photosynthesis, the evolution of fungi, the emergence of large bodied organisms, and colonization of continents by plants. All time-dependent forcings are included Figure 3. In

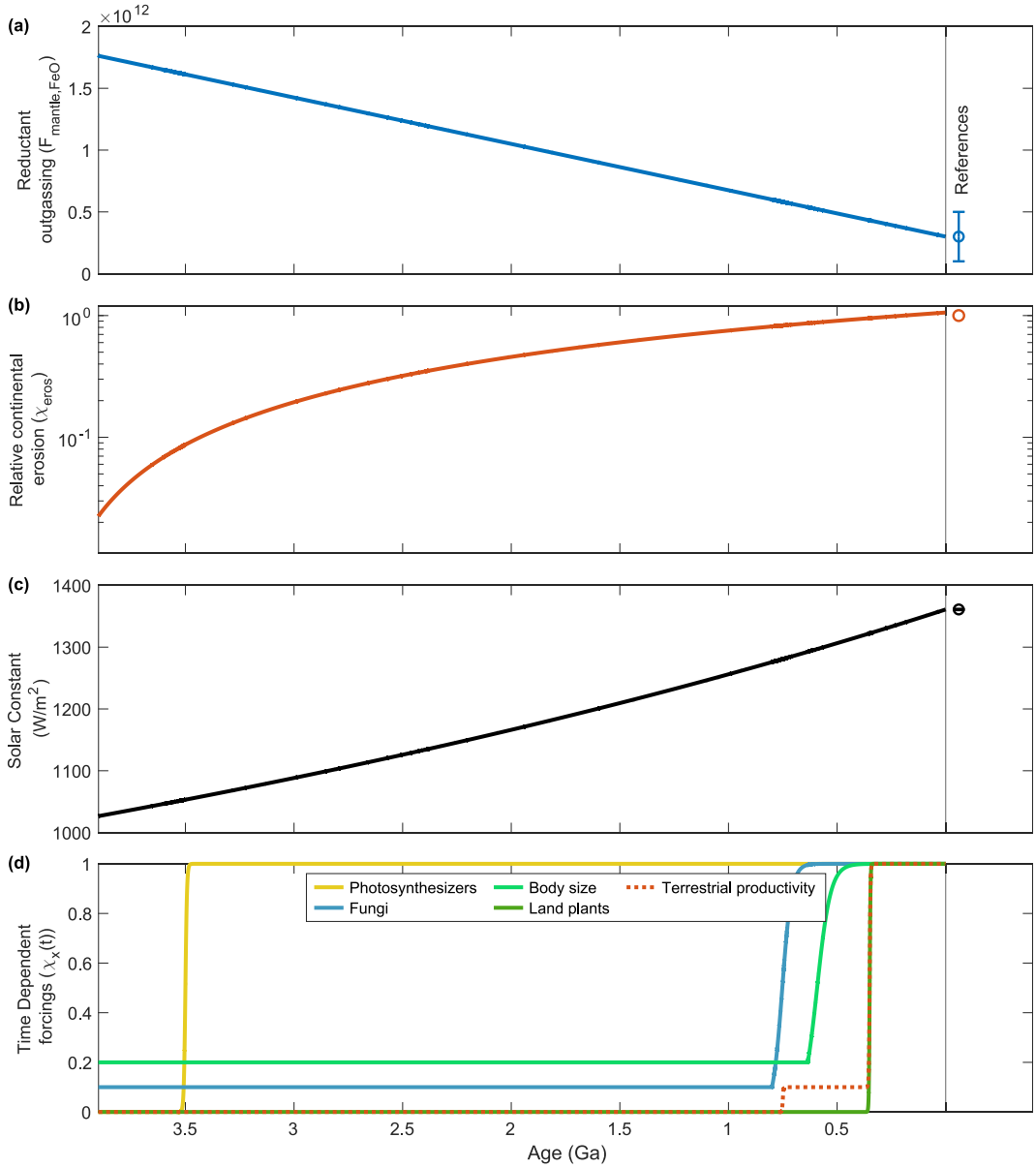

Figure 3. All model forcings (a) mantle reductant outgassing flux ($F_{mantle,FeO}$), prescribed to linearly decrease through time in Equation 13. (b) Relative continental erosion rate, a function of continental size (Equation 14). (c) The quasi-linear increasing solar flux function $S(t)$ in Equation 15. (d) Time-dependent biological transitions described in Equations 16–20. Modern estimates for reservoirs and fluxes are denoted with circles at the far right of each plot, with range estimates as vertical bars; the solid vertical line denotes the end of model output.

the following subsections, t denotes model time in units of years; in terms of our forward modeling approach, $t = 0$ at the start of the Archean (4 Ga) and $t = 4 \times 10^9$ at the modern era (0 Ga).

2.3.1. Mantle Reductant Outflux

The flux of reducing species from the Hadean mantle was likely higher than at present, due to increased heat and faster convection (Blichert-Toft & Albarede, 1994; Sleep & Zahnle, 2001). Reduced iron enters the deep ocean at hydrothermal vents at a rate constrained by modern day mantle outgassing estimates ($F_{mantle,Fe,0} = 3 \times 10^{11}$ mol Fe/yr; Holland, 2002). We impose a linear change in this forcing, decreasing from several times this value in the Archean (χ_{mantle}, see Table A3):

$$F_{\text{mantle,FeO}} = F_{\text{mantle,Fe,0}}\left(\chi_{\text{mantle}} + \frac{(1-\chi_{\text{mantle}})\,t}{4\times10^{9}}\right) \tag{13}$$

The value of χ_{mantle} is found by tuning the timing of the great oxidation event (GOE) (see Section 3.2.2). Because this forcing affects surface redox and because there is no strong evidence that the upper mantle was significantly more reducing in the Archean (Canil, 1997), we do not resolve a reduced iron reservoir in the mantle. Instead, we treat reduced iron output differently from the release of other species from the mantle, which evolve dynamically (Section 2.6.8) to allow for easier testing of different oxygenation scenarios without involving significant changes to outgassing of other mantle species. Explicit treatment of the evolution of mantle oxidation state would be an interesting future addition to EONS.

2.3.2. Continental Erosion

Over time, sediments sourced from continental erosion will accumulate in the deep ocean and cut off lower sediment layers from interacting with the water column; ergo, faster influx of sediments (higher erosion) results in shorter residence in the uppermost "reactive" layer. Sediment burial timescale affects the fraction of OM buried (and net oxygen production) as sedimentary burial competes with remineralization, making erosion an important factor to include in this model. Evidence indicates that erosional rates were lower in the Archean, given that the Archean crust was likely unable to support significant topography (Rey & Coltice, 2008), and increased to near modern rates with uplift by around 3 Ga (Reimink et al., 2021), and erosion is generally understood as a non-linear function of continental topography (Montgomery & Brandon, 2002). We relate erosion to continental emergence (the size of the continental silicate reservoir relative to modern) rather than topography, which we do not resolve:

$$\chi_{\text{eros}}(t) = \left(\frac{R_{\text{c,SiO3}}(t)}{R_{\text{c,SiO3,0}}}\right)^{\eta_{\text{topo}}} \tag{14}$$

where exponent $\eta_{\text{topo}} = -\frac{3}{2}$ represents a weak dependence of erosional rate on continental volume, assuming that low-lying Archean continents experienced a small fraction of modern erosion, while Proterozoic and younger continents achieved similar topographic relief and erosion to today. This curve assumes that continents emerge and begin eroding subaerially early in the Archean; this timing corresponds generally to continental growth models which estimate 50% of modern crustal volume by approximately 3.5 Ga (Hawkesworth et al., 2019), which is approximately when substantial continental shrinking initiates (Dhuime et al., 2018).

2.3.3. Solar Flux

Solar luminosity has increased from approximately 70% modern in the early Hadean at the initiation of nuclear fusion, a result of increasing solar core mass (Feulner, 2012; Gough, 1981; Sagan & Mullen, 1972). We approximate a quasi-linear function for solar flux through time with respect to modern value (S_0; see Table A3). The change in solar flux is formulated following Gough (1981) based on years from the present:

$$S = \left(1 - \frac{0.38\left(t - 4\times10^{9}\right)}{4.55\times10^{9}}\right)^{-1} S_0 \tag{15}$$

2.3.4. Timed Evolution of Photosynthesis

Model runs begin with no operational oxygenic photosynthesis, which we assume evolves sometime in the Archean; estimates range from 3.8 Ga to 2.5 Ga (Crowe et al., 2013; Lyons et al., 2014; J. M. Olson, 2006; Saito et al., 2003). Primary production in the biosphere via photo-ferrotrophy (Section 2.4.1.2) prevails until the end of the Eoarchean (3.6 Ga), when oxygenic photosynthesis develops and rapidly becomes dominant. We force this flux to gradually increase over a few million years along a sigmoidal population growth curve for global photosynthesizers with respect to the modern day, evolving from near zero to 1:

$$\chi_{\text{photo}}(t) = \begin{cases} 0 & t < 4 \times 10^8 \\ \dfrac{1}{1 + 10^{12} \exp\left(-\epsilon_{\text{photo}}\left(t - 4 \times 10^8\right)\right)} & t \geq 4 \times 10^8 \end{cases} \quad (16)$$

where the slope of the curve, ϵ_{photo}, is given in Table A3.

2.3.5. Timed Evolution of Fungi

Fungi, lichens, and plants selectively dissolve inorganic phosphate when it is depleted in soils or sorbed onto oxides, silicates, and calcium compounds (Lambers, 2022). The expansion of fungi onto continents after their evolution around 800 Ma (3.2×10^9 years in model time; Heckman et al., 2001; Lucking et al., 2009) is approximated by a population growth curve:

$$\chi_{\text{fungi}}(t) = \begin{cases} \dfrac{1}{10} & t < 3.2 \times 10^9 \\ \dfrac{1}{1 + 9 \exp\left(-\epsilon_{\text{fungi}}\left(t - 3.2 \times 10^9\right)\right)} & t \geq 3.2 \times 10^9 \end{cases} \quad (17)$$

where the slope of the curve, ϵ_{fungi}, is given in Table A3. Prior to the evolution of fungi, inorganic phosphorus weathering is 10 times slower than its modern rate. After the forced 50 million year expansion of fungi, these fluxes operate on a typical silicate or carbonate weathering timescale.

2.3.6. Timed Evolution of Large-Bodied Organisms

We correlate faster sinking rates of organic material with the evolution of large organisms in the Ediacaran (circa 635 Ma, approximately 3.36×10^9 years in model time) and assume that smaller Precambrian organisms sank at one fifth the rate of modern primary producers.

$$\chi_{\text{sink}}(t) = \begin{cases} \dfrac{1}{5} & t < 3.36 \times 10^9 \\ \dfrac{1}{1 + 4 \exp\left(-\epsilon_{\text{photo}}\left(t - 3.36 \times 10^9\right)\right)} & t \geq 3.36 \times 10^9 \end{cases} \quad (18)$$

The growth slow (ϵ_{photo}; see Equation 16) is provided in Table A3.

2.3.7. Timed Evolution of Land Plants

Vascular land plants enhance continental weathering in the breakdown of bedrock by root systems (Hoffland et al., 2004; Porder, 2019). This enhancement effects the silicate and carbonate weathering modifiers (Section 2.6.4.1), and is formulated as a sigmoidal population growth occurring at 400 Ma (approximately 3.6×10^9 years in model time). This curve is treated similarly to the rise of photosynthesizer populations:

$$\chi_{\text{plants}}(t) = \begin{cases} 0 & t < 3.6 \times 10^9 \\ \dfrac{1}{1 + 10^{12} \exp\left(-\epsilon_{\text{plant}}\left(t - 3.6 \times 10^9\right)\right)} & t \geq 3.6 \times 10^9 \end{cases} \quad (19)$$

where the slope of the curve, ϵ_{plant}, is given in Table A3. Prior to the evolution of land plants, weathering is not enhanced and has a weaker response to elevated atmospheric CO_2. After colonization in the Silurian period (443 Ma), all silicate and carbonate weathering fluxes are enhanced by a factor of 2.

2.3.8. Timed Evolution of the Terrestrial Biosphere

The modern terrestrial biosphere contributes approximately 50% of the global net primary productivity (Ciais et al., 2014). We represent the terrestrial biosphere as a fixed modern OC burial flux that increases with two steps,

the evolution of fungi and colonization of landmasses by plants, at approximately 700 Ma and 400 Ma respectively. We assume fungal evolution constitutes a 10% modern terrestrial biosphere, and land plants increase terrestrial carbon burial from that point to the modern level (reference parameter $F_{\text{terrprod},0} = 1 \times 10^{13}$ mol C/yr is tunable within an estimated range of $2.5 \times 10^{12} - 2 \times 10^{13}$ mol C/yr; Berner, 2009; Lenton et al., 2018). The fraction of modern terrestrial productivity is therefore a function of these other two forcings:

$$\chi_{\text{terr}}(t) = \begin{cases} 0 & t < 3.2 \times 10^9 \\ \frac{1}{10}\chi_{\text{fungi}} & 3.2 \times 10^9 \le t < 3.6 \times 10^9 \\ \frac{1}{10}\chi_{\text{fungi}} + \frac{9}{10}\chi_{\text{plant}} & t \ge 3.6 \times 10^9 \end{cases} \tag{20}$$

The prescribed terrestrial biosphere flux is treated (in mol C/yr):

$$F_{\text{terrprod}} = F_{\text{terrprod},0} f_{\text{CO}_2}^{\eta_w} \chi_{\text{terr}}(t) \tag{21}$$

where f_{CO_2} is the atmospheric level of CO_2 with respect to the modern day (PAL; see Section 2.1) and the exponent η_w describes the CO_2 power-law relationship for physical weathering by vascular plants (see Section 2.6.4.1). This limitation ensures terrestrial productivity decreases as CO_2 (and thus temperature) decreases. We assume 10% of the buried carbon is converted to methane in decomposition.

2.4. Fluxes: Biosphere

2.4.1. Primary Productivity

OM in the ocean/sediment boxes is housed in two reservoirs: living biomass (LB) and dead biomass, or particulate OC. Primary produces utilize CO_2, NH_3, HNO_3, and H_3PO_4 to generate OM and byproducts, such as O_2, and exist only in the surface ocean. We assign OM and remineralization stoichiometry according to Redfield et al. (1963):

$$\begin{aligned} \text{OM} &= (\text{CH}_2\text{O})_{106}(\text{NH}_3)_{16}(\text{H}_3\text{PO}_4) \\ &= \text{C}_{106}\text{H}_{263}\text{O}_{110}\text{N}_{16}\text{P} \end{aligned} \tag{22}$$

More recent measurements of OM stoichiometry deviate from this older ratio, particularly with respect to oxygen and hydrogen content (Anderson & Sarmiento, 1994); we use this stoichiometry because it is still commonly used in biogeochemical modeling.

Primary production in the model is based on photosynthesis, both oxygenic and anoxygenic (photo-ferrotrophic), and nutrient limited. We do not include chemolithoautotrophic organisms or metabolisms based on CO, S, and H_2 (Canfield et al., 2006; Kharecha et al., 2005; Ozaki et al., 2018; Sauterey et al., 2020; Watanabe et al., 2023), though these could be added to a future model version. In practice, this means that the start of our model run can be considered as the evolution of anoxygenic photosynthesis. As photoferrotrophy is confined to anoxic surface ocean conditions, it is only relevant for early Earth conditions (Crowe et al., 2008).

All biological production fluxes are limited by dimensionless nutrient sensitivities defined by fixed nitrogen, phosphate, and carbon surface ocean concentrations and half-saturation uptake values for their assimilation ($k_{j,\text{assim}}$; Table A3). Multiple nutrient limitations are used to resolve changing availability of P, N, and Fe species over geologic timescales and the alternating influence of P and N in particular as ultimate and proximal limiting nutrients (Tyrrell, 1999). Changing availability of N relative to P determines whether direct assimilation is favored over nitrogen fixation; the primacy of one production pathway over the other is determined by how close the ocean is to true Redfield ratio, 16N:1P. Surface ocean fixed nitrogen (all "bioavailable nitrogen," reduced and oxidized; $R_{\text{fixN}} = R_{\text{HNO3,s}} + R_{\text{RN,s}}$) and H_3PO_4 define a Redfield ratio sensitivity parameter:

$$L_{\text{Redf}} = \frac{R_{\text{fixN,s}}/R_{\text{H3PO4,s}}}{R_{\text{fixN,s}}/R_{\text{H3PO4,s}} + k_{\text{assim,NP}}} \tag{23}$$

where $R_{H3PO4,s}$ is the surface ocean reservoir of phosphate, and $k_{assim,NP}$ is a dimensionless half-saturation constant for the Redfield sensitivity (B. W. Johnson & Goldblatt, 2018). This parameter ensures that as the ratio of dissolved fixed N:P decreases, production shifts increasingly toward nitrogen fixation.

2.4.1.1. Oxygenic Photosynthesis

Nitrogen, carbon, and phosphate are incorporated into LB via photosynthetic biological assimilation, producing OM and oxygen. The stoichiometry of this assimilation flux depends on the source of nitrogen. When HNO_3 is used:

$$106CO_2 + 16HNO_3 + H_3PO_4 + 122H_2O \xrightarrow{h\nu} (CH_2O)_{106}(NH_3)_{16}(H_3PO_4) + 138O_2 \quad (24)$$

and when NH_3 is used:

$$106CO_2 + 16NH_3 + H_3PO_4 + 106H_2O \xrightarrow{h\nu} (CH_2O)_{106}(NH_3)_{16}(H_3PO_4) + 106O_2 \quad (25)$$

Phosphate is a limiting nutrient in the ocean. Therefore, the process of photosynthetic assimilation depends foremost on the surface reservoir of H_3PO_4:

$$F_{assim} = \frac{R_{H3PO4,s}}{\tau_{assim}} L_{assim,DIC} L_{Redf} r_{\frac{C}{P}} \chi_{photo}(t) \quad (26)$$

where τ_{assim} is the timescale of photosynthetic assimilation and $r_{\frac{C}{P}}$ is the Redfield ratio of carbon to phosphate (106:1), converting this flux to units of mol C/yr. Photosynthesis evolves after 3.6 Ga according to the population growth curve $\chi_{photo}(t)$; before this time, the term $\chi_{photo}(t) = 0$.

2.4.1.2. Photoferrotrophy

In anoxic surface waters, ferrous iron (Fe(II)) can be oxidized by iron-oxidizing bacteria. This is considered a possible source of the iron oxides (here simplified to iron hydroxide, $Fe(OH)_3$) which comprise the Archean BIFs, and may have been a significant component of early marine primary productivity (Canfield et al., 2006; Crowe et al., 2008; Kendall et al., 2012). This is also a pathway for transference of reducing power from iron to OC, which can then be oxidized and recycled by biological systems.

$$\begin{aligned} 4FeO + CO_2 + \frac{16}{106} \quad & NH_3 \quad + \frac{1}{106} H_3PO_4 + 11H_2O \\ & \xrightarrow{h\nu} \\ 4Fe(OH)_3 + \frac{1}{106}(CH_2O)_{106} \quad & (NH_3)_{16} \quad (H_3PO_4) + 5H_2O \end{aligned} \quad (27)$$

Photoferrotrophic production takes the form:

$$F_{ferrotrophy} = \frac{R_{FeO,s}}{\tau_{assim}} L_{assim,DIC} L_{assim,fixN} L_{assim,H3PO4} (1 - L_{anox,O2,s}) \quad (28)$$

This pathway requires anoxic conditions, and so has additional sensitivities to the degree of anoxicity of the reservoir ($L_{anox,O2,s}$), defined by the upper limit for dissolved oxygen concentration in an anoxic zone ($[O_2] < 6.2 \times 10^{-3}$ mol/m^3; Crowe et al., 2008) and availability of reduced fixed nitrogen ($L_{assim,\ fixN}$). Photoferrotrophs are more well adapted to growing under lower light, which may lend them an advantage over photosynthesizers in competition for upwelling phosphorus; such an advantage may have influenced photoferrotroph dominance over early oxygenic photosynthesizers (Jones et al., 2015; Ozaki et al., 2019); EONS does not resolve different water column depths for primary producer populations, so this nuance is not resolved.

2.4.1.3. Nitrogen Fixation

Atmospheric nitrogen is made available for biological incorporation via nitrogen fixation when biologically utilizable RN (NH_3) is depleted. We parameterize nitrogen fixation by oxygenic photosynthesizers (cyanobacteria) as:

$$N_2 + 3H_2O \rightarrow 2NH_3 + \frac{3}{2}O_2 \tag{29}$$

Newly fixed ammonia produced in this reaction is assumed to be immediately assimilated into biomass, via either photosynthetic assimilation pathway (Equations 25 or 27). The two-step process of fixation and assimilation yields a net reaction sequence:

$$106CO_2 + 8N_2 + H_3PO_4 + 130H_2O \rightarrow (CH_2O)_{106}(NH_3)_{16}(H_3PO_4) + 118O_2 \tag{30}$$

Photosynthetic fixation depends on the surface ocean reservoir of phosphate, DIC, and N_2, and is inversely proportional to surface ocean N:P ratio. In units of mol N/yr:

$$F_{\mathrm{fix,newN}} = \frac{R_{\mathrm{H3PO4,s}}}{\tau_{\mathrm{fix}}} L_{\mathrm{assim,DIC}} L_{\mathrm{fix,N2}} (1 - L_{\mathrm{Redf}}) \chi_{\mathrm{photo}}(t) \mathrm{r}_{\frac{N}{P}} \tag{31}$$

where $\mathrm{r}_{\frac{N}{P}}$ is the Redfield ratio of nitrogen to phosphorus uptake (16:1), τ_{fix} is the timescale for nitrogen fixation (estimated to be approximately 5 times longer than assimilation; Fennel et al., 2005). Uptake (or release) of other species ($j = CO_2$, H_3PO_4, O_2 and H_2O) associated with assimilation of newly fixed N is:

$$F_{\mathrm{fix,j}} = F_{\mathrm{fix,newN}} \mathrm{r}_{\left(\frac{j}{\mathrm{newN}}\right)} \tag{32}$$

Where $\mathrm{r}_{\left(\frac{j}{\mathrm{newN}}\right)}$ is the ratio of the other species to the moles of assimilated new NH_3 (Table A3).

Prior to the evolution of oxygenic photosynthesis, nitrogen fixation (Equation 29) occurs simultaneously with photoferrotrophy (Equation 27) using excess iron:

$$\begin{gathered} 472FeO + 106CO_2 + 8N_2 + H_3PO_4 + 1322H_2O \\ \xrightarrow{h\nu} \\ 472Fe(OH)_3 + (CH_2O)_{106} \quad (NH_3)_{16} \quad (H_3PO_4) + 484H_2O \end{gathered} \tag{33}$$

Anoxygenic fixation is measured in mols Fe/yr, and formulated:

$$F_{\mathrm{fixation,FeO}} = \frac{R_{\mathrm{FeO,s}}}{\tau_{\mathrm{fix}}} L_{\mathrm{assim,DIC}} L_{\mathrm{assim,H3PO4}} L_{\mathrm{fix,N2}} (1 - L_{\mathrm{Redf}}) \left(1 - \chi_{\mathrm{photo}}(t)\right) \tag{34}$$

The uptake of other species ($j = N_2$, CO_2, H_3PO_4, and H_2O) in this reduction process is treated:

$$F_{\mathrm{fixation,j}} = F_{\mathrm{fixation,FeO}} \mathrm{r}_{\frac{j}{\mathrm{FeO}}} \tag{35}$$

where $\mathrm{r}_{\frac{j}{\mathrm{FeO}}}$ is the ratio of the other species to the moles of iron (Table A3).

2.4.2. Nitrification

Nitrifiers use O_2 to convert NH_4^+ into HNO_3 (Gruber, 2008).

$$\begin{aligned} NH_4^+ + \tfrac{3}{2}O_2 &\longrightarrow NO_2^- + 2H^+ + H_2O \\ NO_2^- + \tfrac{1}{2}O_2 &\longrightarrow NO_3^- \\ \hline NH_4^+ + 2O_2 &\longrightarrow HNO_3 + H^+ + H_2O \end{aligned} \tag{36}$$

Nitrification cannot occur in acidic conditions (pH ≤ 6) and full nitrification requires an environmental pH of 7.2 (Hiatt & Grady, 2008). Thus, the nitrification flux depends on $[O_2]$, $[H^+]$, and $[NH_4^+]$ within a given ocean or reactive sediment box i (s, d, n, or z):

$$F_{\text{nit},i} = \frac{[NH_4^+]_i M_{\text{oc},i}}{\tau_{\text{nit}}} L_{\text{nit,O2},i}(1 - L_{\text{nit,H},i}) \tag{37}$$

where $M_{\text{oc},i}$ is the mass of water in reservoir i (kg), and τ_{nit} is the timescale in years for nitrification (Table A3).

2.4.3. Death of Living Biomass

Organic matter is transferred to the particulate OC reservoir when it dies.

$$F_{\text{death}} = \frac{R_{\text{LB}}}{\tau_{\text{death}}} \tag{38}$$

Biomass living and dead is tracked in units of moles of carbon.

2.4.4. OM Remineralization

Remineralization, or respiration, occurs in every ocean and sediment box containing OM ($i = s$, d, n, or z). This transformation follows either aerobic or anaerobic pathways depending on oxygen availability; these include ammonification, denitrification, and methanogenesis. Because we do not resolve a sulfur cycle, we do not include microbial sulfur reduction as a remineralization pathway, although this constitutes a major anaerobic metabolism in modern sediments (Jørgensen, 1977).

2.4.4.1. Aerobic Remineralization: Ammonification

In aerobic remineralization, particulate OC is oxidized by dissolved O_2 and returned to its nutrient components in Redfield ratio (Froelich et al., 1979), a reversal of oxygenic photosynthesis (Equation 25):

$$(CH_2O)_{106}(NH_3)_{16}(H_3PO_4) + 106O_2 \rightarrow 106CO_2 + 16NH_3 + H_3PO_4 + 106H_2O \tag{39}$$

Aerobic remineralization occurs when the ocean or sediment box i is sufficiently oxygenated, taking the form (in mol C/yr):

$$F_{\text{ammon},i} = \frac{R_{\text{OC},i}}{\tau_{\text{oxrm},i}} L_{\text{ammon,O2},i} \tag{40}$$

where $\tau_{\text{oxrm},i}$ denotes the timescale for aerobic remineralization (Table A3). In oxygenated waters, this remineralization pathway (ammonification) will dominate over the anaerobic pathways.

2.4.4.2. Anaerobic Remineralization: Denitrification and Methanogenesis

In the case of ocean anoxia, remineralization proceeds anaerobically along two different pathways. When it is available, nitrate is used by heterotrophic denitrifiers to oxidize OM (Berman-Frank et al., 2008; Froelich et al., 1979):

$$\begin{aligned} (CH_2O)_{106}(NH_3)_{16} \quad & (H_3PO_4) + \frac{424}{5}HNO_3 \\ & \rightarrow \\ 106CO_2 + \frac{212}{5}N_2 + 16 \quad & NH_3 + H_3PO_4 + \frac{742}{5}H_2O \end{aligned} \tag{41}$$

In the case that nitrate is not readily available, anaerobic remineralization is by methanogenesis:

$$(CH_2O)_{106}(NH_3)_{16}(H_3PO_4) \rightarrow 53CO_2 + 53CH_4 + 16NH_3 + H_3PO_4 \tag{42}$$

Both anaerobic remineralization fluxes return nutrients to the water column in similar fashion as aerobic remineralization, except that they occur over longer timescales ($\tau_{oxrm,i} < \tau_{axrm,i}$) approximating reduced energetic yield.

Our model quantifies the denitrification flux in an ocean/sediment box i (in mol C/yr):

$$F_{denit,i} = \frac{R_{OC,i}}{\tau_{axrm,i}}(1 - L_{ammon,O2,i})\, L_{denit,HNO3,i} \tag{43}$$

The uptake ratio for denitrification (r_{denit}), in terms of mol HNO_3 per mol OC, is 84.8:106.

Our model quantifies the methanogenesis flux (in mol C/yr) for box i:

$$F_{methgen,i} = \frac{R_{OC,i}}{\tau_{axrm,i}}(1 - L_{ammon,O2,i})\,(1 - L_{denit,HNO3,i}) \tag{44}$$

2.4.5. Methanotrophy

Methane is oxidized in ocean or sediment boxes by methanotrophs, converting it to CO_2 (Goldblatt et al., 2006):

$$CH_4 + 2O_2 \rightarrow CO_2 + 2H_2O \tag{45}$$

Methanotrophy is limited by the reservoir of CH_4 and dissolved oxygen in a box i (s, d, n, or z):

$$F_{mtrophy,i} = \frac{R_{CH4,i}}{\tau_{mtrophy}} L_{mtrophy,O2,i} \tag{46}$$

2.5. Fluxes: Atmosphere-Ocean Chemistry

2.5.1. Ammonia Photo-Oxidation and Photolysis

Ammonia is irreversibly destroyed by high-energy UV radiation in the atmosphere, generating N^{3-} and H^+:

$$\begin{aligned} NH_3 \quad & \xrightarrow{h\nu} NH_2^- + H^+ \\ NH_2^- \quad & \xrightarrow{h\nu} NH^{2-} + H^+ \\ NH^{2-} \quad & \xrightarrow{h\nu} N^{3-} + H^+ \end{aligned} \tag{47}$$

When oxygen is available, the produced hydrogen ions will react to generate water, with a net reaction:

$$2NH_3 + \frac{3}{2}O_2 \xrightarrow{6h\nu} N_2 + 3H_2O \tag{48}$$

We parameterize ammonia photo-oxidation:

$$F_{\text{ammox}} = \frac{R_{\text{NH3,a}}}{\tau_{\text{ammox}}(O_2)} \tag{49}$$

Photo-oxidation timescale ($\tau_{\text{ammox}}(O_2)$) is a function of oxygen level, such that the lifetime of NH_3 is extended in anoxic conditions:

$$\tau_{\text{ammox}}(O_2) = \tau_{\text{ammox},0}\frac{R_{\text{O2,a}}}{n_a} \tag{50}$$

Under anoxic conditions, we treat the stoichiometry of ammonia photodissociation (photolysis) as:

$$8NH_3 + 3CO_2 \xrightarrow{12h\nu} 4N_2 + 3CH_4 + 6H_2O \tag{51}$$

Ammonia photolysis is treated similarly to photo-oxidation, but without the sensitivity to oxygen and over a longer timescale:

$$F_{\text{pholys}} = \frac{R_{\text{NH3,a}}}{\tau_{\text{pholys}}} \tag{52}$$

2.5.2. Methane Photo-Oxidation

Methane is photo-oxidized through a variety of pathways (Claire et al., 2006; Garduno Ruiz et al., 2023; Pavlov et al., 2001), with a net stoichiometry of:

$$CH_4 + 2O_2 \xrightarrow{4h\nu} CO_2 + 2H_2O \tag{53}$$

This reaction is slowed by orders of magnitude once an ozone layer provides photochemical shielding (Claire et al., 2006; Garduno Ruiz et al., 2023; Goldblatt et al., 2006; Gregory et al., 2021). We parametrize this as:

$$F_{\text{methox}} = K_{\text{eff}}([CH_4][O_2])^{\frac{1}{2}} \tag{54}$$

The effective rate constant (K_{eff}) is fitted to model results from Garduno Ruiz et al. (2023) and is a product of CH_4 and O_2 atmospheric mixing ratios:

$$K_{\text{eff}} = 3 \times 10^{20}\left(4 \times 10^{3\left(\frac{-[O_2]}{[O_2]+10^{-4}}\right)^{\frac{2}{5}}}\right) \tag{55}$$

K_{eff} has units of mol O_2 yr^{-1}. This new parametrization is recommended over that used in Goldblatt et al. (2006) as it avoids a polynomial fit, which performed poorly outside of the fitted range.

2.5.3. Hydrogen Escape

Our model considers mildly reducing to oxidizing atmospheres, in which hydrogen-bearing species are minor atmospheric constituents. Hydrogen escape is therefore diffusion limited, and depends on the total hydrogen mixing ratio at the homopause (Hunten, 1973). We consider hydrogen escape to derive only from non-condensible species, CH_4 and NH_3, with stoichiometry:

$$\begin{array}{c} CH_4 \xrightarrow{4h\nu} C + 4H\uparrow \\ C + H_2O \longrightarrow \frac{1}{2}CO_2 + \frac{1}{2}CH_4 \\ \hline CH_4 + H_2O \xrightarrow{4h\nu} \frac{1}{2}CO_2 + \frac{1}{2}CH_4 + 4H\uparrow \end{array} \tag{56}$$

and

$$\begin{aligned} \mathrm{NH_3} &\xrightarrow{3h\nu} \mathrm{N} + 3\,\mathrm{H}\uparrow \\ 2\,\mathrm{N} &\longrightarrow \mathrm{N_2} \\ \hline 2\,\mathrm{NH_3} &\xrightarrow{6h\nu} \mathrm{N_2} + 6\,\mathrm{H}\uparrow \end{aligned} \tag{57}$$

These species are well-mixed, so the mixing ratio at the homopause is the general mixing ratio and hydrogen escape can be treated for gas j (in units of mol N/yr or mol C/yr, for NH_3 and CH_4 respectively):

$$F_{\mathrm{Hesc},j} = k_{\mathrm{Hesc}}[j]\frac{1}{\mathrm{H}_j} \tag{58}$$

where H_j is the number of H molecules per mole of gas j (i.e. $H_{NH3} = 3$) and k_{Hesc} is the average diffusion constant for H (in mol H/yr):

$$k_{\mathrm{Hesc}} = \frac{\left(5\times10^{13}\ \text{molecules cm}^{-2}\ \text{s}^{-1}\right)\left(3.15\times10^{7}\ \text{s yr}^{-1}\right)\left(100^2 A_E\right)}{N_{\mathrm{Av}}} \tag{59}$$

where A_E is the surface area of Earth (m^2) and N_{Av} is Avogadro's constant (6.02×10^{23} molecules mol^{-1}). See Table A3 for the value of k_{Hesc}.

We do not consider hydrogen escape derived from water, as in temperate atmospheres water is cold-trapped at the tropopause, so the homopause mixing ratio will be negligible. If the climatology of the model was expanded to consider hot and moist atmospheres, then a term for water-derived hydrogen escape would need to be added.

2.5.4. Calcium Carbonate Precipitation and Dissolution

Calcium carbonate ($CaCO_3$) is precipitated when an ocean reservoir is oversaturated with respect to the carbonate ion (CO_3^{2-}) and dissolves when undersaturated. In modern oceans this process is mediated by biology; we treat precipitation and dissolution as purely inorganic responses to ocean chemistry so as to keep our biosphere as simple as possible.

$$\mathrm{Ca^{2+}} + 2\,\mathrm{HCO_3^-} \underset{\Omega<1}{\overset{\Omega\geq1}{\rightleftharpoons}} \mathrm{CaCO_3} + \mathrm{CO_2} + \mathrm{H_2O} \tag{60}$$

Precipitation and dissolution fluxes are driven by $\left[CO_3^{2-}\right]$ and $[CaCO_3]$, respectively, in a given ocean or reactive sediment box ($i = s, d, n$, or z):

$$F_{\mathrm{precip},i} = \begin{cases} \dfrac{(\Omega_i - 1)^{\eta_{\mathrm{calc}}}\left[\mathrm{CO_3^{2-}}\right]_i M_{\mathrm{oc},i}}{\tau_{\mathrm{precip}}} & \Omega_i \geq 1 \\ 0 & \Omega_i < 1 \end{cases} \tag{61}$$

$$F_{\mathrm{diss},i} = \begin{cases} 0 & \Omega_i \geq 1 \\ \dfrac{(1 - \Omega_i)^{\eta_{\mathrm{diss}}} R_{\mathrm{CaCO3},i}}{\tau_{\mathrm{diss}}} & \Omega_i < 1 \end{cases} \tag{62}$$

where $R_{\mathrm{CaCO3},i}$ is the reservoir of $CaCO_3$ (in mol C), $M_{\mathrm{oc},i}$ is the mass of the box (kg), τ_{precip} and τ_{diss} are reaction timescales, and η_{calc} and η_{diss} are the thermodynamic rate powers of the calcification and dissolution reactions, respectively (Ridgwell et al., 2007; Zeebe, 2012). Calcium carbonate saturation state is calculated:

$$\Omega_i = \frac{\left[Ca^{2+}\right]_{i,0}\left[CO_3{}^{2-}\right]_i}{K_{sp,i}(T,S,P)} \quad (63)$$

where $\left[Ca^{2+}\right]_{i,0}$ is a fixed concentration (mol/kg) and K_{sp} is an acid dissociation constant (Zeebe & Wolf-Gladrow, 2001; appendix Appendix B, Table A3). We arbitrarily use aragonite saturation to calculate precipitation and dissolution fluxes, but calcite saturation could also be used for Equation 63.

2.5.5. Iron Photo-Oxidation

In an oxygenated surface ocean, reduced iron is converted into iron hydroxide (Braterman et al., 1983):

$$4FeO + O_2 + 11H_2O \xrightarrow{4h\nu} 4Fe(OH)_3 + 5H_2O \quad (64)$$

This flux is limited by ferrous iron availability and oxygen level:

$$F_{Fephotox} = \frac{R_{FeO,s}}{\tau_{photox}} L_{O2,anox,s} \quad (65)$$

where τ_{photox} is a timescale for the photo-oxidation reaction (see Table A3). This is unlikely a major source of iron oxides comprising Archean banded iron formations (BIFs; Konhauser, Amskold, et al., 2007) but is still an important pathway for abiological iron oxidation.

2.5.6. Organic Phosphate Scavenging

Some anaerobic bacteria are capable of selectively remineralizing phosphate from particulate OM (Van Cappellen & Ingall, 1994).

$$(CH_2O)_{106}(NH_3)_{16}(H_3PO_4) \rightarrow (CH_2O)_{106}(NH_3)_{16} + H_3PO_4(aq) \quad (66)$$

In laminated (anoxic) sediments, deviations from Redfield ratio C:P can exceed 10 times the regular ratio of 106:1 (Alcott et al., 2019; Van Cappellen & Ingall, 1994), implying that this scavenging is more energetically favored in anoxic sedimentary settings. We assume scavenging is primarily limited by the amount of available organically bound phosphate, and increases proportionally with the phosphorus supply limitation on primary production. For i = sediment boxes n or z:

$$F_{scav,i} = \frac{R_{OP,i}}{\tau_{sink,i}}(1 - L_{H3PO4,assim})(1 - L_{O2,anox,i}) f_{scav} \quad (67)$$

where f_{scav} is the maximum fraction of organic phosphorus (OP) scavenged (0.1).

2.5.7. Phosphate Adsorption Onto Iron

Phosphate can be adsorbed onto and buried within iron oxide deposits (Bjerrum & Canfield, 2002; Reinhard et al., 2017):

$$Fe(OH)_3 + H_3PO_4 \rightarrow FePO_4 + 3\ H_2O \quad (68)$$

This reaction depends heavily on low pH (allowing the speciation of orthophosphate, $PO_4{}^{3-}$), iron oxide reservoir, the concentration of phosphate (in mol kg^{-1}), and a speciation constant (k_{ads}, in units of kg mol^{-1}; Bjerrum & Canfield, 2002). For ocean boxes (i = s, d, n or z):

$$F_{\text{sorb},i} = \frac{R_{\text{FeOH3},i}}{\tau_{\text{sorb}}}[H_3PO_4]_i k_{\text{ads}}(1 - L_{\text{pH,sorb},i}) \quad (69)$$

As pH increases above neutral, the speciation (and thus absorption) of orthophosphate decreases. In reality, this reaction is also dependent on the dissolved silica concentration, which competes with phosphate for adsorption sites (Konhauser, Lalonde, et al., 2007). We do not resolve a silica cycle in this model, so we ignore that dependency in this formulation.

2.6. Fluxes: Geosphere

2.6.1. Sediment Burial

Reactive sediments (i) are eventually buried by overlying material and cut off from porewater; species buried in pelagic (z) sediments are transferred to "unreactive" sediments (u) cut off from ocean-atmosphere interaction, while species buried in shelf (n) sediments become part of the continent (c). Burial of particulate species ($j = CaCO_3$, $Fe(OH)_3$, $FePO_4$, OC, organic nitrogen (ON), SP, and OP) is treated:

$$F_{\text{burial},j,i} = \frac{R_{j,i}}{\tau_{\text{sink,i,0}}\chi_{\text{eros}}(t)} \quad (70)$$

where $\tau_{\text{sink,i,0}}$ is the modern residence time (yr) of reactive sediments. We do not track $FePO_4$ as a mineral species in the continent, instead burying this species as silicate-bound phosphate and iron oxide separately.

$$FePO_4 + 3\,H_2O \rightarrow Fe(OH)_3 + H_3PO_4 \quad (71)$$

Dissolved H_3PO_4 is buried after first being incorporated into apatite, via:

$$5\,Ca^{2+} + 3\,H_3PO_4 + 10\,HCO_3^- + H_2O \rightarrow Ca_5(PO_4)_3OH + 10\,H_2O + 10\,CO_2 \quad (72)$$

We avoid creating a separate carbonate reservoir and alkalinity effects during phosphorus speciation by simplifying Equation 72 to a mass movement flux only affecting phosphate:

$$H_3PO_4(aq) \rightarrow H_3PO4(s) \quad (73)$$

Phosphate's incorporation into apatite in the sediments proceeds at a rate proportional to its dissolved concentration, generating a long-term sink for inorganic phosphorus (Kraal et al., 2017). This flux is primarily controlled by the burial of carbonate, a small portion of which contains absorbed apatite minerals. For $i = n$ or z:

$$F_{\text{burial,PO4},i} = F_{\text{burial,CaCO3},i}\frac{[H_3PO_4]_i}{[H_3PO_4]_0}f_{\text{apatite}} \quad (74)$$

Co-precipitation of calcite and apatite requires specific environmental conditions (Knudsen & Gunter, 2002); as such, we use a conservative fraction ($f_{\text{apatite}} = 0.01$) for estimating the portion of carbonate buried with apatite. $[H_3PO_4]_0$ is a modern concentration of dissolved phosphate (1–2 μM; Talley, 2007; Koltermann et al., 2011).

2.6.2. Downgoing Material

At the intersection of oceanic and continental crust, three major pathways emerge for species in the ocean crust and unreactive sediments: accretion, subduction, or melting ($f_{\text{acc}} + f_{\text{sub}} + f_{\text{melt}} = 1$; see Table 2 and Figure 4). Melted materials are then either volatilized at arc volcanoes (Section 2.6.2.2) or recrystallized onto the continent (Section 2.6.2.3; $f_{\text{volc}} + f_{\text{cryst}} = f_{\text{melt}}$); thus, distribution is species dependent. Sediments are twice as likely to be scraped off and accreted compared to the underlying oceanic slab; correspondingly, ocean slab reservoirs are twice as likely to be subducted as overriding sediments.

Table 2
Subduction Zone Summary

Box	Accretion	Subduction	Melting
Unreactive sediments	$f_{acc,u} = 0.1$	$f_{sub,u} = 0.05$	$f_{melt} = 0.85$
Ocean crust	$f_{acc,o} = 0.05$	$f_{sub,o} = 0.1$	$f_{melt} = 0.85$

Note. The apportionment of downgoing materials in the unreactive sediments and oceanic slab.

2.6.2.1. Subduction and Accretion

Subduction of oceanic lithosphere requires, at least in part, negative buoyancy resulting from thermal contrast between the overriding ocean crust and the upper mantle; as such, a hotter younger crust would be more difficult to subduct, perhaps up to a factor of 2 in the Archean (Korenaga, 2006). Additionally, seafloor spreading rate has varied throughout geologic time as a function of mantle heat decay (Korenaga, 2010; Padhi et al., 2012). Rather than try to capture the complexities of crustal rheology and mantle evolution that truly control subduction for these species, we simply assume small, fixed fractions of the downgoing slab and sediments are subducted and that this subduction occurs at a fixed rate corresponding to modern seafloor spreading (approximately 10^8 years at present based on average age of modern oceanic crust; Müller et al., 2008).

Both subduction and accretion fluxes are simply residence-dependant mass transfers; for a species hosted in the unreactive sediments (j = OC, ON, OP, carbonate-bound phosphate (CP), SP, and $Fe(OH)_3$) these fluxes ($x = sub$ or acc) are:

$$F_{x,j} = \frac{R_{j,u}}{\tau_{sub}} f_{x,u} \tag{75}$$

where τ_{sub} is seafloor spreading/subduction timescale. For NH_4^+ hosted only in the oceanic crust, subduction and accretion are:

$$F_{x,NH4} = \frac{R_{NH4,o}}{\tau_{sub}} f_{x,o} \tag{76}$$

As it is hosted in both reservoirs, the total accretion/subduction flux for calcium carbonate includes the fraction from unreactive sediments and the fraction from the ocean slab:

$$F_{x,CaCO3} = \frac{f_{x,u} R_{CaCO3,u} + f_{x,o} R_{CaCO3,o}}{\tau_{sub}} \tag{77}$$

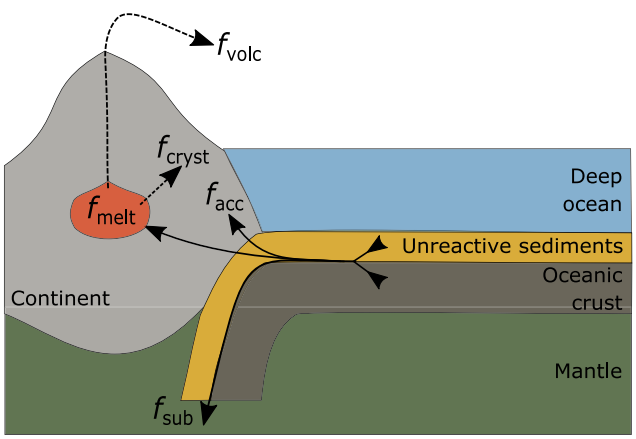

Figure 4. Subduction zone schematic. A schematic representation of model subduction zones, highlighting slab subduction, accretion, and melt fractions (f_{acc}, f_{sub}, and f_{melt}, respectively). Melt fraction is split into either a volcanic ($f_{volc,j}$) or crystalline ($f_{cryst,j}$) fraction, depending on species' volatility.

2.6.2.2. Volcanism

The downgoing slab and the accompanying unreactive sediments are exposed to flux melting and an assumed fraction of that melt ($f_{volc,j}$) can be volatilized at the arc front, releasing gases to the atmosphere. Organic matter in the unreactive sediments releases CO_2, CH_4, and NH_3 to the atmosphere (residual H_3PO_4 is recrystallized; see Section 2.6.2.3):

$$(CH_2O)_{106}(NH_3)_{16}(H_3PO_4) \xrightarrow{heat} 53\,CO_2\uparrow + 53\,CH_4\uparrow + 16\,NH_3\uparrow + H_3PO_4(c) \tag{78}$$

Calcium carbonate in both the sediments and the slab releases CO_2:

$$CaCO_3 + SiO_2 \xrightarrow{heat} CO_2\uparrow + CaSiO_3 \tag{79}$$

Silicate-bound ammonium in the slab releases NH_3:

$$(NH_4)_2SiO_3 \xrightarrow{heat} 2\,NH_3\uparrow + SiO_2 + H_2O \tag{80}$$

Volcanism occurs along an assumed timescale of subduction (τ_{sub}). Organic species (j = OC, ON) are hosted in the unreactive sediments and not in the slab, therefore:

$$F_{volc,j} = \frac{R_{j,u}}{\tau_{sub}} f_{volc,j} \tag{81}$$

Organic carbon fully volatilizes ($f_{volc,OC} = f_{melt}$) whereas ON is only partially volatilized. Calcium carbonate exists in both the sediments and the slab and fully volatilizes:

$$F_{volc,CaCO3} = \frac{R_{CaCO3,u} + R_{CaCO3,o}}{\tau_{sub}} f_{volc,CaCO3} \tag{82}$$

Silicate-bound NH_4^+ is only in the slab and is assumed to be partially volatilized, therefore:

$$F_{volc,NH4} = \frac{R_{NH4,o}}{\tau_{sub}} f_{volc,NH4} \tag{83}$$

2.6.2.3. Recrystallization

Species in the slab and sediments without volatile components, and those assumed only partially volatilized, are recrystallized onto the continent rather than outgassed to the atmosphere when exposed to flux melting. For species j in the unreactive sediments ($Fe(OH)_3$, SP, CP, OP, ON), this is formulated:

$$F_{cryst,j} = \frac{R_{j,u}}{\tau_{sub}} f_{cryst,j} \tag{84}$$

All of these species except ON are assumed to be exclusively recrystallized ($f_{cryst,j} = f_{melt}$); CP and OP are transferred to the silicate-bound (SP) reservoir. Organic-bound N is assumed partially recrystallized with the same fraction as NH_4^+; for NH_4^+ in the oceanic crust:

$$F_{cryst,NH4} = \frac{R_{NH4,o}}{\tau_{sub}} f_{cryst,NH4} \tag{85}$$

2.6.3. Metamorphism

Metamorphism from tectonic activity (uplift) or from exposure to intrusive volcanics volatilizes compounds from the continental reservoirs (j = $CaCO_3$, OC, ON, OP, or NH_4) along an assumed timescale (τ_{meta}):

$$F_{meta,j} = \frac{R_{j,c}}{\tau_{meta}} \tag{86}$$

The species associated with OM (CO_2, CH_4, and NH_3) are volatilized in Redfield ratio, with the exception of H_3PO_4, which we assume is instead transferred from the organic to the carbonate-bound reservoir (Ruttenberg, 2003). As these organic species are tracked in separate sediment and continental reservoirs, we remove the carbon and nitrogen volatiles from them separately. Organic carbon is volatilized as both CO_2 and CH_4, in a 50/50 split (the same stoichiometry used in volcanism, Equation 78). Inorganic carbon and nitrogen metamorphism assumes the same stoichiometry as volcanism (Equations 79 and 80).

2.6.4. Continental Crust Weathering

Weathering of continental reservoirs introduces DIC, alkalinity, RN, and H_3PO_4 to the surface ocean. Continental weathering reactions respond interactively to temperature and atmospheric composition.

2.6.4.1. Weathering Modifiers

Weathering fluxes are enhanced by atmospheric CO_2 and temperature (Bergman et al., 2004; Brady & Carroll, 1994; Rushby et al., 2018; Walker et al., 1981; Zeebe, 2012). The transfer of CO_2 from the atmosphere to the ocean (as DIC and alkalinity) via weathering is a vital negative feedback stabilizing the climate on geologic timescales (Walker et al., 1981). Temperature controls weathering by enhancing precipitation (runoff), dissolution rates for silicate and carbonate minerals (Brady & Carroll, 1994), as well as subsequent precipitation of $CaCO_3$ which ultimately sequesters atmospheric carbon (Walker et al., 1981). Terrestrial weathering is further driven by the formation of carbonic acid (biologically and abiologically) in soils, enhanced by higher pCO_2 and biological activity (Berner, 1991; Brady & Carroll, 1994).

We adapt the treatment of chemical weathering used in the COPSE (Bergman et al., 2004) and GEOCARB (Berner, 1991) models such that weathering here responds interactively to higher CO_2 and temperatures. For our purposes, it is important to consider the effects of plant vegetation (enhancing weathering); in the GEOCARB and COPSE models, pre-plant weathering sensitivity is assumed higher than weathering after plants evolve. We assume the same pre-plant CO_2 sensitivity used in those models, but allow evolution of plants to enhance weathering up to a factor of 2 times the pre-plant modifier (Ibarra et al., 2019). Thus, weathering modifiers are also time-dependent, and take the form $m_j(t, T, CO_2)$, for j indicating carbonate, subaerial (granitic), and seafloor (basaltic) reactions:

$$m_j = \Theta_j(T) f_{CO_2}^{\eta_w} \left(1 + \chi_{plants}(t)\right) \tag{87}$$

where f_{CO_2} is the atmospheric level of CO_2 with respect to the modern day (PAL) and the exponent η_w describes the CO_2 power-law relationship for weathering (between 0.2 and 0.5 for weak or strong control, respectively; Berner, 1991; Bergman et al., 2004; Sleep & Zahnle, 2001). Temperature-sensitive mineral dissolution, $\Theta_j(T)$, is an Arrhenius equation:

$$\Theta_j = \exp\left(\frac{E_j}{R}\left(\frac{1}{290} - \frac{1}{T}\right)\right) \tag{88}$$

where the term R is the gas constant and E_j is the activation energy of mineral dissolution (Table A3). We use specific minerals to characterize dissolution properties; continental carbonate dissolution uses dolomite (Herman & White, 1985), continental silicates uses diopside (Brady & Carroll, 1994; Schott et al., 1981), and seafloor basalts are enstatite and olivine (Schott et al., 1981; Wogelius & Walther, 1992).

Seafloor basalt weathering involves low-temperature off axis hydrothermal fluids (Coogan & Gillis, 2018) and depends on deep ocean temperature, assuming that hydrothermal fluids are at least 10°C hotter than the surrounding water, and dissolved CO_2 levels:

$$f_{dCO_2} = \frac{[CO_2]_z}{[CO_2]_{z,0}} \tag{89}$$

This term replaces f_{CO_2} in Equation 87 (Table A3).

Weathering enhancement from continental vegetation is modified from Bergman et al. (2004):

$$W_{plant}(t, CO_2) = \begin{cases} 0 & t \le 3.6 \times 10^9 \\ f_{plants}(t)\left(\frac{2 f_{CO_2}}{1 + f_{CO_2}}\right)^{0.4} & t > 3.6 \times 10^9 \end{cases} \tag{90}$$

where $f_{plant}(t)$ is an imposed sigmoidal growth curve for land plant population fraction (Section 2.3.7). We do not include the plant weathering enhancement in calculating the seafloor weathering modifier.

Terrestrial weathering is primarily limited by exposure of fresh rock surfaces and access to leached cations (West et al., 2005); this implies that chemical weathering processes have a maximum rate defined by physical erosion,

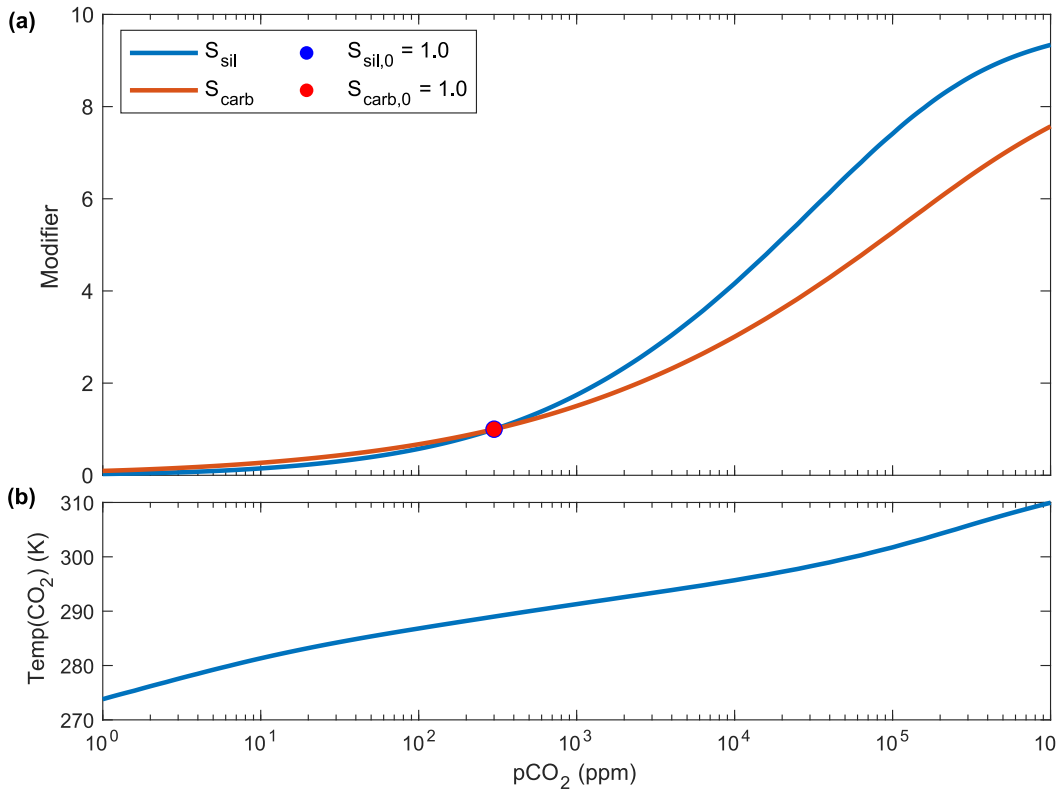

Figure 5. Weathering sensitivities (a) carbonate and silicate weathering sensitivities, S_{carb} and S_{sil} for different pCO_2 conditions; (b) temperature as a function of CO_2 partial pressure, calculated with Equation 125 using modern solar constant and partial pressures for CH_4, N_2, and NH_3. General sensitivities are calculated using Equations 87–91 and surface temperatures from CO_2 radiative forcing only. Reference modifiers for modern, pre-industrial pCO_2 (300 ppm) are plotted as circles.

perhaps up to 10 times modern, which cannot be exceeded (Mills et al., 2011). We normalize continental weathering modifiers with respect to modern CO_2, temperature, and vegetation conditions ($m_{j,0} = 1$ for 290 K and 280 ppm pCO_2), producing dimensionless weathering sensitivities:

$$S_j = a_w \frac{m_j}{m_j + b_w} \tag{91}$$

for species j being carbonate or silicate. The factors a_w and b_w are tuned to achieve a sensitivity range of 10 times the modern at higher temperatures and CO_2 levels (Figure 5). Seafloor weathering is limited by the rate of hydrothermal fluid flow through the basaltic ocean crust (Sleep & Zahnle, 2001), which we do not resolve; we normalize this flux to a modifier of 1 for present day:

$$S_{\mathrm{sfw}} = \frac{m_{\mathrm{sfw}}}{m_{\mathrm{sfw}} + 1} \tag{92}$$

2.6.4.2. Carbonate Weathering

Inorganic carbon and associated apatite minerals are weathered chemically by atmospheric CO_2 (Bergman et al., 2004; Zeebe, 2012):

$$\mathrm{CaCO_3(c) + H_2O + CO_2(a) \rightarrow Ca^{2+} + 2\,HCO_3^-(aq)} \tag{93}$$

Carbonate-bound phosphate in apatite ($Ca_3(PO_4)_2$) weathers:

$$\mathrm{Ca_3(PO_4)_2 + 3\,H_2O + 3\,CO_2(a) \rightarrow 3\,Ca^{2+} + 2\,H_3PO_4(aq) + 3\,CO_3^{2-}(aq)} \tag{94}$$

This is simplified to a transfer of phosphate from the continent to the oceans, without any affects on alkalinity in addition to regular carbonate weathering:

$$H_3PO_4(c) \rightarrow H_3PO_4(aq) \tag{95}$$

Carbonate weathering is generally:

$$F_{\text{wthr,CaCO3}} = \frac{R_{\text{CaCO3,c}}}{\tau_{\text{wcarb}}} S_{\text{carb}}(t, T, CO_2) \tag{96}$$

where τ_{wcarb} is the lifetime of continental carbonates (yr), which is shorter than the canonical lifetime of continents.

Carbonate-bound phosphate weathering is formulated (in mol P/yr):

$$F_{\text{wthr,CP}} = \frac{R_{\text{CP,c}}}{\tau_{\text{wcarb}}/\chi_{\text{fungi}}(t)} S_{\text{carb}}(t, T, CO_2) \tag{97}$$

Note that this weathering flux occurs over a modified carbonate weathering timescale which becomes equivalent to regular carbonate weathering only after the evolution of fungi late in the model run (see Section 2.3.5).

2.6.4.3. Silicate Weathering

Continental silicates are weathered by CO_2, generating clay minerals and transferring atmospheric carbon to the ocean. We treat silicate weathering as alteration of igneous rocks (approximated here as wollastonite, $CaSiO_3$):

$$CaSiO_3(c) + H_2O + 2\,CO_2(a) \rightarrow Ca^{2+} + 2\,HCO_3^-(aq) + SiO_2 \tag{98}$$

Igneous silicates contain significant NH_4^+, which substitutes for K + in muscovite and biotite ($KAl_2(AlSi_3O_{10})(OH)_2$) and alkali feldspars (Buddingtonite, $NH_4AlSi_3O_8$). We approximate this flux as buddingtonite weathering to kaolinite and silica, measured in units of mol N/yr:

$$\begin{aligned} 4\,NH_4AlSi_3O_8(c) + 6\,H_2O + 4\,CO_2(a) &\rightarrow 4\,NH_4AlSi_3O_8 + 4\,H_2CO_3 + 2\,H_2O \\ &\rightarrow 4\,NH_4^+ + Al_4Si_4O_{10}(OH)_8 + 8\,SiO_2 + 4\,HCO_3^- \end{aligned} \tag{99}$$

To reduce the use of untracked species (i.e., K and Al), we simplify to a stoichiometry that is broadly analogous to wollastonite weathering:

$$(NH_4)_2SiO_3(c) + 2\,CO_2(a) + H_2O \rightarrow 2\,NH_4^+(aq) + SiO_2 + 2\,HCO_3^-(aq) \tag{100}$$

Silicate-bound phosphorus weathering is treated the same as carbonate-bound phosphorus weathering (Equation 95), transferring continental SP to H_3PO_4 in the ocean without any effects on alkalinity.

We assume that a large portion of Earth's surface reduced iron reservoir is confined in continental silicates as fayalite olivine; fayalite is weathered by CO_2 as with other silicates but also oxidized when atmospheric O_2 becomes available, producing hematite:

$$Fe_2SiO_4 + CO_2(a) + H_2O + \frac{1}{2}O_2(a) \rightarrow Fe_2O_3(c) + H_2CO_3(aq) + SiO_2 \tag{101}$$

The magnitude of subaerial silicate weathering is dictated by the size of the crustal silicate reservoir (i.e., the size of the continents), which is parameterized to grow directly from mantle input and thus broadly scales with CO_2 outgassing. In units of mols CO_2/yr:

$$F_{\text{wthr,sil}} = 2\frac{R_{\text{SiO3,c}}}{\tau_{\text{wsil}}} S_{\text{sil}}(t, T, CO_2) \tag{102}$$

where τ_{wsil} is the timescale of silicate weathering, essentially the lifetime of the continents. Silicate-bound ammonium is similarly treated (in mol N/yr):

$$F_{\mathrm{wthr,NH4}} = \frac{R_{\mathrm{NH4,c}}}{\tau_{\mathrm{wsil}}} S_{\mathrm{sil}}(t, T, \mathrm{CO_2}) \tag{103}$$

Silicate-bound phosphorus weathering is partially controlled by selective dissolution of silicate-bound phosphate by fungi, lichens, and plants (Lambers, 2022). Thus, phosphate weathering will be slower than modern rates prior to the evolution of fungi (circa 700 Ma; see Section 2.3.5). In mol P/yr:

$$F_{\mathrm{wthr,SP}} = \frac{R_{\mathrm{SP,c}}}{\tau_{\mathrm{wsil}}/\chi_{\mathrm{fungi}}(t)} S_{\mathrm{sil}}(t, T, \mathrm{CO_2}) \tag{104}$$

In the modern context when $\chi_{\mathrm{fungi}}(t) = 1$, this flux occurs over the same timescale as regular silicate weathering.

Reduced iron (fayalite) weathers along the canonical silicate timescale but is limited by the availability of oxygen:

$$F_{\mathrm{wthr,Feox}} = \frac{R_{\mathrm{Fe2SiO4,c}}}{\tau_{\mathrm{wsil}}} \sqrt{f_{\mathrm{O_2}}} S_{\mathrm{sil}}(t, T, \mathrm{CO_2}) \tag{105}$$

Unlike other weathering fluxes, this does not include transport of the product, hematite, to the oceans; rather, it remains in a new continental reservoir.

2.6.4.4. Oxidative Weathering

Organic matter is removed from the continental reservoir (c) via oxidative weathering when oxygen is plentiful in the atmosphere (Bergman et al., 2004).

$$(\mathrm{CH_2O})_{106}(\mathrm{NH_3})_{16}(\mathrm{H_3PO_4})(c) + 106\,\mathrm{O_2(a)} \rightarrow 106\,\mathrm{CO_2} + 16\,\mathrm{NH_3} + \mathrm{H_3PO_4} + 106\,\mathrm{H_2O} \tag{106}$$

Oxidative weathering occurs along a specific timescale (τ_{woxi}) and takes the form (for species j indicating OC, ON, OP):

$$F_{\mathrm{wthr},j} = \frac{R_{j,\mathrm{c}}}{\tau_{\mathrm{woxi}}} \sqrt{f_{\mathrm{O_2}}} \tag{107}$$

2.6.5. Reverse Weathering

Reverse weathering is essentially the reverse of silicate weathering (Equation 98), forming authigenic clay at the expense of porewater alkalinity:

$$\mathrm{Ca^{2+}} + 2\,\mathrm{HCO_3^-} + \mathrm{SiO_2} \rightarrow \mathrm{CaSiO_3} + 2\,\mathrm{CO_2} + \mathrm{H_2O} \tag{108}$$

We base our formulation for this reaction on that of Isson and Planavsky (2018) with a few simplifications. For $i = n$ or z:

$$F_{\mathrm{revwthr},i} = 2k_{\mathrm{rw},i}(\mathrm{pH}_i)[\mathrm{Si}]_0 V_i \tag{109}$$

where V_i is the volume of reactive sediment porewaters (in $\mathrm{m^3}$), $[\mathrm{Si}]_0$ is the concentration of silica in modern porewaters ($\leq$0.1 $\mathrm{mol/m^3}$; Isson & Planavsky, 2018), and term $k_{\mathrm{rw},i}(\mathrm{pH}_i)$ is the estimated modern rate of reverse weathering, determined by porewater pH (units $\mathrm{yr^{-1}}$):

$$k_{\mathrm{rw},i} = 1.01 \times 10^{-19} \mathrm{pH}_i^{22.4} \tag{110}$$

Reverse weathering is multiplied by 2 to equate the moles of silica (not tracked) to moles bicarbonate consumed in the reaction. We assume a simpler sensitivity to silica concentrations than that of Isson and Planavsky (2018) since the pH-sensitivity of the rate parameter k_{rw} is a much stronger control on the overall reaction rate and we keep dissolved silica constant (see Table A3).

2.6.6. Seafloor Weathering

Dissolved CO_2 reacts with seafloor basalts in hydrothermal settings, precipitating carbonate minerals in ocean crust (Sleep & Zahnle, 2001):

$$CO_2(aq) + CaSiO_3 \rightarrow CaCO_3 + SiO_2 \tag{111}$$

Seafloor weathering here is based on an estimated modern rate (k_{sfw} in units of mol C/yr; Mills et al., 2014; Gillis & Coogan, 2011) and responds to deep ocean and pelagic sediment dissolved [CO_2] (Section 2.6.4.1):

$$F_{sfw} = k_{sfw} S_{sfw}\left(t, [CO_2]_z\right) \tag{112}$$

This flux bolsters the silicate weathering climate feedback when continental surface area is lower, and at present is estimated to operate at a similar magnitude as carbon degassing a mid-ocean ridges (Coogan & Gillis, 2013). Therefore it is likely that this flux was a significant component of the carbon-silicate feedback in the Archean (Hayes & Waldbauer, 2006; Sleep & Zahnle, 2001).

2.6.7. Hydrothermal Alteration

Ammonium is incorporated into silicate minerals-primarily biotite-during hydrothermal alteration (Holloway & Dahlgren, 2002). We treat this as cation exchange within ocean crust, where NH_4^+ replaces K^+ (untracked) and using the simplified N-silicate stoichiometry described in Section 2.6.4.3. Stoichiometrically:

$$2\,NH_4^+(aq) + SiO_2 + 2\,HCO_3^- \rightarrow (NH_4)_2SiO_3 + 2\,CO_2(aq) + H_2O \tag{113}$$

Hydrothermal incorporation depends on pelagic sediment porewater (NH_4^+), the rate of hydrothermal flow, and (because this is a symbolic alteration of silicates) is sensitive to CO_2 and temperature. Our flux formulation is similar to that used by B. W. Johnson and Goldblatt (2018):

$$F_{hyd} = \left[NH_4^+\right]_z \rho_{oc} k_{hyd} S_{sfw}\left(t, [CO_2]_z\right) \tag{114}$$

where ρ_{oc} is the density of ocean waters (in kg/m^3), and k_{hyd} is an estimated volumetric flow rate for hydrothermal vents, in units of m^3/yr.

2.6.8. Mantle Outgassing and Plumes

The entirety of modern continental reservoirs for N and C and 95% of silicate-bound phosphate, Fe_2SiO_4, and SiO_3 are initially contained within the mantle reservoir (m) and are gradually transferred to the surface either as outgassing volatiles (for carbon and nitrogen) or in the form of plume emplacement onto continental bodies (for phosphorus, iron, and silicate species). The flux of species j depends on the mantle overturn rate (τ_{mantle}):

$$F_{mantle,j} = \frac{f_m R_{j,m}}{\tau_{mantle}} \tag{115}$$

where $f_m = 0.1$ is a tunable parameter, here assuming that only 10% of the upper mantle is outgassing/erupting. Carbon and nitrogen species are released in both reduced (CH_4 and NH_3) and neutral forms (CO_2 and N_2). For species $j = CH_4$ or NH_3 and $j^* = C$ or N:

$$F_{mantle,j} = f_{red} F_{mantle,j^*} \tag{116}$$

and for species $j = CO_2$ or N_2:

$$F_{\text{mantle},j} = \left(1 - f_{\text{red}}\right) F_{\text{mantle},j^*} \tag{117}$$

where $f_{\text{red}} = 0.01$ is the fraction of total element outgassed as a reduced species.

2.7. Fluxes: Exchanges

2.7.1. Air-Sea Gas Exchange

Atmospheric gases ($j = N_2$, NH_3, CO_2, CH_4, and O_2) exchange via diffusion with the surface ocean (s) using the stagnant boundary approximation of Liss (1974), following B. W. Johnson and Goldblatt (2018):

$$F_{\text{air-sea},j} = \frac{D_j}{d_{\text{sl}}} A_{\text{s}} \left(C_{j,\text{s}} - \kappa_j(T) P_j\right) \tag{118}$$

A positive flux is toward the atmosphere, and negative is into the ocean. D_j is the diffusion constant of each species and d_{sl} is the thickness of the stagnant boundary layer, thus giving the gas-phase transfer velocity (m/yr); A_{s} is the surface area of the ocean; $C_{j,\text{s}}$ is the concentration of species j in the surface ocean and is calculated by dividing the species reservoir (R_j, s) by the surface ocean volume (V_{s}); P_j is the partial pressure for gas j in the atmosphere, calculated (in Pa):

$$P_j = R_{j,\text{a}} \frac{P_0}{n_0} \tag{119}$$

where $n_0 = 1.8 \times 10^{20}$ mol in present atmosphere and $P_0 = 101{,}325$ Pa per atmosphere. A temperature dependent Henry's Law constant for species j ($\kappa_j(T)$; mol $m^3 Pa^{-1}$) is calculated according to Sander (2015):

$$\kappa_j(T) = \kappa_{0,j} \exp\left(\nu_j \left[\frac{1}{T} - \frac{1}{T_0}\right]\right) \tag{120}$$

where T is the surface temperature in Kelvin, $\kappa_{0,j}$ is the Henry's Law constant at the reference temperature ($T_0 = 298.15$ K), and $\nu_j = -\Delta_{\text{sol}} H/R$, a constant value for each species within relatively small temperature deviations from T_0 (see Table A3 for these values).

2.7.2. Ocean Mixing

All dissolved species (j) in the ocean boxes ($i = s$ or d) are transferred between the two in accordance with concentration gradients via volumetric water flux (B. W. Johnson & Goldblatt, 2018):

$$F_{\text{mix},j,i} = Q\left(\frac{R_{j,i}}{V_i} - \frac{R_{j,i^*}}{V_{i^*}}\right) \tag{121}$$

V_i is the volume of the ocean box (m^3) and Q is the volumetric flow rate (m^3/yr), which is calculated by dividing the deep ocean volume, V_{d}, by the deep ocean water lifetime, τ_{oc}.

2.7.3. Export

Particulate species in the surface ocean sink into the deep ocean according to the relative productivity fraction of the shelf versus the open ocean (f_{Pshelf}; see Section 2.7.5). During their descent, OC and $CaCO_3$ are susceptible to remineralization or dissolution, respectively. For species j (OC, $CaCO_3$, and $Fe(OH)_3$) this flux is generally:

$$F_{\text{export},j} = \frac{R_{j,\text{s}}}{\tau_{\text{export},j}} \left(1 - f_{\text{Pshelf}}\right) \tag{122}$$

Export timescales differ between these species: OC sinking is modified here by the size of organisms relative to the modern day ($\tau_{\text{export,OC}} = \tau_{\text{sink,s}}/\chi_{\text{sink}}(t)$), a boundary forcing. Sinking calcium carbonate in the surface ocean is 10 times faster than particulate OC sinking, accounting for increased ballast $\left(\tau_{\text{export,CaCO3}} = \frac{1}{10}\tau_{\text{sink,s}}/\chi_{\text{sink}}(t)\right)$; therefore nearly 90% of inorganic carbon escapes significant dissolution and is exported from the surface ocean (Emerson & Hedges, 2008). Particulate iron species sink at an average rate of 2×10^4 m/yr with no dependency on body size ($\tau_{\text{export,FeOH3}} = \frac{d_s}{2\times10^4}$; Thompson et al., 2019).

2.7.4. Diffusion Into Sediments

Dissolved species (j = N_2, RN, HNO_3, H_3PO_4, O_2, CH_4, TA, DIC) diffuse into and out of the porewaters of reactive sediments (i^* = n or z) from the overlying surface or deep ocean (i = s or d) according to the concentration gradient between those two reservoirs (Boudreau, 1996).

$$F_{\text{diff},j,i^*} = \left(\frac{[j]_i - [j]_{i^*}}{h_z}\right)\lambda_j A_{i^*} \tag{123}$$

where $[j]$ denotes a species concentration in units of (mol m^{-3}), λ_j is the diffusion coefficient (m^2/yr) for species j (Table A3), and h_z is the length of diffusion (0.01 m). A_{i^*} is either the surface area of the ocean (and pelagic sediments for diffusion into z) or the surface area of the continental shelf (for diffusion into n), in m^2.

2.7.5. Sedimentation

Particulate species (j = OC, $CaCO_3$, and $Fe(OH)_3$) suspended in the surface or deep ocean reservoirs (i = s or d) eventually settle into underlying sediments (neritic or pelagic, respectively; i^* = n or z) along depth-dependent timescales:

$$F_{\text{sed},j,i^*} = \frac{R_{j,i}}{\tau_{\text{sed},i,j(t)}} f_{\text{sed},i^*} \tag{124}$$

Sedimentation timescales differ between species similarly to export (Section 2.7.3): OC and carbonate sinking rates are modified by the size of organisms relative to the modern day ($\tau_{\text{sed},i,\text{OC}} = \tau_{\text{sink,i}}/\chi_{\text{sink}}(t)$ and $\tau_{\text{sed},i,\text{CaCO3}} = \frac{1}{10}\tau_{\text{sink,i}}/\chi_{\text{sink}}(t)$). Particulate iron sinks faster no dependency on body size ($\tau_{\text{sed},i,\text{FeOH3}} = \frac{d_i}{2\times10^4}$; Thompson et al., 2019). All particulates in the deep ocean settle into the pelagic sediments ($f_{\text{sed,z}} = 1$); neritic sediments gain the un-exported fraction of particulate matter sinking out of the surface ocean ($f_{\text{sed,n}} = f_{\text{Pshelf}}$).

2.8. Climate

We base our parameterization of surface temperature on a radiative equilibrium, gray atmosphere model (Goody & Yung, 1995), fitting the thermal optical depth to the strength of the greenhouse effect similar to Lenton (2000). We include linear water vapor feedback, but for simplicity do not include non-linearities such as the runaway greenhouse effect or ice-albedo feedback. The change in Earth's surface temperature associated with an increase in the partial pressure of greenhouse gases depends on the amount of greenhouse forcing (GF) that each gas exerts (in W/m^2). Greenhouse forcing is correlated to gas mixing ratio by interpolating onto the line-by-line radiative transfer data from Byrne and Goldblatt (2014); total GF is the sum of all greenhouse gases ($GF_t = GF_{NH_3} + GF_{CO_2} + GF_{CH_4}$).

Radiative balance for the surface under a gray atmosphere is:

$$\sigma T^4 = (1-\alpha)\left(\frac{S(t)}{4}\right)\left(1 + \frac{3}{4}\gamma_{IR}\right) \tag{125}$$

where σ is the Stefan-Boltzmann constant (W $m^{-2}K^{-4}$), T is surface temperature (K), α is planetary albedo, and $S(t)$ is solar flux forcing (Wm^{-2}), which increases quasi-linearly through time (see Section 2.3.3; Table A3). We parameterize thermal optical depth:

$$\gamma_{IR} = f_{N2}^{q}(a_T(T-250) + b_T GF_t) \tag{126}$$

Constants a_T and b_T are fitted to the radiative transfer data from Byrne and Goldblatt (2014) by solving two simultaneous equations for surface temperature $T = 289$ K maintained by GF under (a) modern pCO_2 and solar flux (300 ppm and 1,361 Wm^{-2}) and (b) Archean pCO_2 and solar flux (45,000 ppm and 1,020 Wm^{-2} at 4 Ga; Goldblatt et al., 2021). This fitting yields a climate sensitivity of 2.6 K per CO_2 doubling. Pressure broadening of absorption spectra, $f_{N_2}^{q}$, is a function of the atmospheric N_2 level relative to modern, with constant q fitted to increase surface temperature by 4.4°C per pN_2 doubling at 2.5 Ga (Goldblatt et al., 2009; Table A3). Temperature change then relates to the difference in radiative fluxes, scaled by surface area (A_E, in m^2), ocean mass (M_{oc}, in kg), and water's specific heat capacity (c_p, in J kg^{-1} K^{-1}):

$$\left.\frac{dT}{dt}\right|_{GHF} = \frac{A_E}{M_{oc}c_p}\left((1-\alpha)\left(\frac{S(t)}{4}\right)\left(1+\frac{3}{4}\gamma_{IR}\right) - \sigma T^4\right) \tag{127}$$

Surface ocean temperature is assumed equal to the atmospheric temperature ($T_s = T$). The temperature of the neritic (shelf) reactive sediments (T_n) reflects surface ocean temperatures, but 5°C colder. The temperature of the deep ocean and underlying reactive sediments (T_d and T_z) are assumed to be 15°C and 17°C degrees colder than the surface, respectively (277–278 K or 4–5°C in the deep ocean, 275.5 K or 2.5°C in sediments given a modern surface ocean temperature of 20°C; Tromp et al., 1995).

2.9. Differential Equations

The EONS model is comprised of a series of ODEs that evolve the aforementioned surface reservoirs of the Earth system through time. The model is written in Matlab and uses the in-built ode15s solver for stiff systems.

The model is run in two steps because the transition to operational oxygenic photosynthesis is rather dramatic. The model is run initially with initial conditions for the Eoarchean for 400 million years without oxygenic photosynthesis. We then restart the model run with the output from the first 400 million years as initial conditions, this time allowing operational photosynthesis. This restarted model run then proceeds for 3.6 billion years, and then the two runs are spliced together to create one continuous evolutionary curve.

2.9.1. Atmosphere

$$\frac{dR_{NH3,a}}{dt} = F_{air\text{-}sea,NH3} + f_{red}F_{mantle,N} + F_{volc,NH4} + F_{meta,NH4} + \frac{16}{106}(F_{volc,OC} + F_{meta,OC}) - F_{ammox} - F_{pholys} - F_{Hesc,NH3} \tag{128}$$

$$\frac{dR_{N2,a}}{dt} = F_{air\text{-}sea,N2} + \frac{1}{2}\left(\left(1-f_{red}\right)F_{mantle,N} + F_{ammox} + F_{pholys} + F_{Hesc,NH3}\right) \tag{129}$$

$$\frac{dR_{CO2,a}}{dt} = F_{air\text{-}sea,CO2} + \left(1-f_{red}\right)F_{mantle,C} + F_{meta,CaCO3} + F_{volc,CaCO3} + \frac{1}{2}(F_{meta,OC} + F_{volc,OC} + F_{methox} + F_{Hesc,CH4}) - F_{wthr,CaCO3} - F_{wthr,sil} - F_{wthr,NH4} - F_{wthr,Feox} - \frac{3}{8}F_{pholys} - \frac{19}{20}F_{terrprod} \tag{130}$$

$$\frac{dR_{O2,a}}{dt} = F_{air\text{-}sea,O2} + F_{terrprod} - F_{methox} - F_{wthr,oxi} - \frac{3}{4}F_{ammox} - \frac{1}{2}F_{wthr,Feox} \tag{131}$$

$$\frac{dR_{CH4,a}}{dt} = F_{air\text{-}sea,CH4} + f_{red}\,F_{mantle,C} + \frac{3}{8}F_{pholys} + \frac{1}{2}F_{meta,OC} + \frac{1}{2}F_{volc,OC} + \frac{1}{20}F_{terrprod} - \frac{1}{2}F_{methox} - F_{Hesc,CH4} \quad (132)$$

$$\frac{dR_{H2O,a}}{dt} = F_{methox} + \frac{3}{2}F_{ammox} + \frac{3}{4}F_{pholys} + \frac{1}{2}F_{meta,NH4} + \frac{1}{2}F_{volc,NH4} - F_{Hesc,CH4} - F_{wthr,CaCO3} - F_{wthr,sil} - \frac{1}{2}F_{wthr,NH4} - F_{wthr,Feox} - F_{terrprod} \quad (133)$$

2.9.2. Surface Ocean

$$\frac{dR_{N2,s}}{dt} = F_{mix,N2,s} + \frac{42}{106}F_{denit,s} - F_{fixation,N2} - \frac{1}{2}F_{fix,newN} - F_{air\text{-}sea,N2} - F_{diff,N2,n} \quad (134)$$

$$\frac{dR_{RN,s}}{dt} = F_{mix,RN,s} + F_{wthr,NH4} + F_{wthr,ON} + \frac{16}{106}(F_{ammon,s} + F_{denit,s} + F_{methgen,s}) - \frac{16}{106}f_{RN}\,F_{assim} - \frac{4}{106}F_{ferrotrophy} - F_{nit,s} - F_{diff,RN,n} - F_{air\text{-}sea,NH3} \quad (135)$$

$$\frac{dR_{HNO3,s}}{dt} = F_{mix,HNO3,s} + F_{nit,s} - \frac{16}{106}(1 - f_{RN})\,F_{assim} - \frac{84.4}{106}F_{denit,s} - F_{diff,HNO3,n} \quad (136)$$

$$\frac{dR_{H3PO4,s}}{dt} = F_{mix,H3PO4,s} + F_{wthr,OP} + F_{wthr,SP} + F_{wthr,CP} - F_{fix,H3PO4} - F_{fixation,H3PO4} + \frac{1}{106}(F_{ammon,s} + F_{denit,s} + F_{methgen,s} - F_{assim}) - \frac{1}{424}F_{ferrotrophy} - F_{sorb,s} - F_{diff,H3PO4,n} \quad (137)$$

$$\frac{dR_{LB,s}}{dt} = F_{assim} + F_{fix,CO2} + F_{fixation,CO2} + \frac{1}{4}F_{ferrotrophy} - F_{death} \quad (138)$$

$$\frac{dR_{ON,s}}{dt} = \frac{16}{106}(F_{death} - F_{ammon,s} - F_{denit,s} - F_{methgen,s} - F_{export,OC} - F_{sed,OC,n}) \quad (139)$$

$$\frac{dR_{OP,s}}{dt} = \frac{1}{106}(F_{death} - F_{ammon,s} - F_{denit,s} - F_{methgen,s} - F_{export,OC} - F_{sed,OC,n}) \quad (140)$$

$$\frac{dR_{OC,s}}{dt} = F_{death} - F_{ammon,s} - F_{denit,s} - F_{methgen,s} - F_{export,OC} - F_{sed,OC,n} \quad (141)$$

$$\frac{dR_{CaCO3,s}}{dt} = F_{precip,s} - F_{diss,s} - F_{export,CaCO3} - F_{sed,CaCO3,n} \quad (142)$$

$$\frac{dR_{TA,s}}{dt} = F_{mix,TA,s} + F_{wthr,sil} + 2F_{wthr,CaCO3} + 2F_{diss,s} + F_{wthr,NH4} + F_{wthr,ON} + \frac{16}{106}(1 - f_{RN})\,F_{assim} + \frac{16}{106}(F_{ammon,s} + F_{denit,s} + F_{methgen,s}) + \frac{84.4}{106}F_{denit,s} - \frac{16}{106}f_{RN}\,F_{assim} - \frac{4}{106}F_{ferrotrophy} - 2F_{precip,s} - 2F_{nit,s} - F_{diff,TA,n} - F_{air\text{-}sea,NH3} \quad (143)$$

$$\frac{dR_{DIC,s}}{dt} = F_{mix,DIC,s} + 2F_{wthr,CaCO3} + F_{wthr,sil} + F_{wthr,oxi} + F_{wthr,NH4} + F_{wthr,Feox} + F_{ammon,s} + F_{denit,s} + \frac{1}{2}F_{methgen,s} + F_{mtrophy,s} + F_{diss,s} - F_{assim} - F_{fix,CO2} - F_{fixation,CO2} - \frac{1}{4}F_{ferrotrophy} - F_{precip,s} - F_{air\text{-}sea,CO2} - F_{diff,DIC,n} \quad (144)$$

$$\frac{dR_{CH4,s}}{dt} = F_{mix,CH4,s} + \frac{1}{2}F_{methgen,s} - F_{mtrophy,s} - F_{air\text{-}sea,CH4} - F_{diff,CH4,n} \quad (145)$$

$$\frac{dR_{O2,s}}{dt} = F_{mix,O2,s} + \left(\frac{138}{106}(1 - f_{RN}) + f_{RN}\right)F_{assim} + F_{fix} - 2F_{nit,s} - F_{ammon,s} - 2F_{mtrophy,s} - \frac{1}{4}F_{Fephotox} - F_{air\text{-}sea,O2} - F_{diff,O2,n} \quad (146)$$

$$\frac{dR_{H2O,s}}{dt} = F_{wthr,oxi} + F_{wthr,Feox} + F_{ammon,s} + \frac{148.4}{106}F_{denit,s} + F_{nit,s} + 2F_{mtrophy,s} + F_{precip,s} + 3F_{sorb,s} - \left(\frac{122}{106}(1 - f_{RN}) + f_{RN}\right)F_{assim} - F_{fix,H2O} - F_{fixation,H2O} - \frac{7}{4}F_{ferrotrophy} - \frac{6}{4}F_{Fephotox} - F_{diss,s} \quad (147)$$

$$\frac{dR_{FeO,s}}{dt} = F_{mix,FeO,s} - F_{ferrotrophy} - F_{fixation,FeO} - F_{Fephotox} \quad (148)$$

$$\frac{dR_{FeOH3,s}}{dt} = F_{ferrotrophy} + F_{fixation,FeO} + F_{Fephotox} - F_{sorb,s} - F_{export,FeOH3} - F_{sed,FeOH3,n} \quad (149)$$

$$\frac{dR_{FePO4,s}}{dt} = F_{sorb,s} - F_{export,FePO4} - F_{sed,FePO4,n} \quad (150)$$

2.9.3. Neritic Sediments

$$\frac{dR_{N2,n}}{dt} = F_{diff,N2,n} + \frac{42}{106}F_{denit,n} \quad (151)$$

$$\frac{dR_{RN,n}}{dt} = F_{diff,RN,n} + \frac{16}{106}(F_{ammon,n} + F_{denit,n} + F_{methgen,n}) - F_{nit,n} \quad (152)$$

$$\frac{dR_{HNO3,n}}{dt} = F_{diff,HNO3,n} + F_{nit,n} - \frac{84.4}{106}F_{denit,n} \quad (153)$$

$$\frac{dR_{H3PO4,n}}{dt} = F_{diff,H3PO4,n} + \frac{1}{106}(F_{ammon,n} + F_{denit,n} + F_{methgen,n}) + F_{scav,n} - F_{sorb,n} - F_{burial,PO4,n} \quad (154)$$

$$\frac{dR_{ON,n}}{dt} = \frac{16}{106}(F_{sed,OC,n} - F_{ammon,n} - F_{denit,n} - F_{methgen,n}) - F_{burial,ON,n} \quad (155)$$

$$\frac{dR_{OP,n}}{dt} = \frac{1}{106}(F_{sed,OC,n} - F_{ammon,n} - F_{denit,n} - F_{methgen,n}) - F_{burial,OP,n} - F_{scav,n} \quad (156)$$

$$\frac{dR_{OC,n}}{dt} = F_{sed,OC,n} - F_{ammon,n} - F_{denit,n} - F_{methgen,n} - F_{burial,OC,n} \quad (157)$$

$$\frac{dR_{CaCO3,n}}{dt} = F_{sed,CaCO3,n} + F_{precip,n} - F_{diss,n} - F_{burial,CaCO3,n} \quad (158)$$

$$\frac{dR_{TA,n}}{dt} = F_{diff,TA,n} + 2F_{diss,n} + \frac{84.4}{106}F_{denit,n} + \frac{16}{106}(F_{ammon,n} + F_{denit,n} + F_{methgen,n}) - 2F_{precip,n} - F_{revwthr,n} - 2F_{nit,n} \quad (159)$$

$$\frac{dR_{DIC,n}}{dt} = F_{diff,DIC,n} + F_{ammon,n} + F_{denit,n} + \frac{1}{2}F_{methgen,n} + F_{mtrophy,n} + F_{diss,n} - F_{precip,n} \quad (160)$$

$$\frac{dR_{CH4,n}}{dt} = F_{diff,CH4,n} + \frac{1}{2}F_{methgen,n} - F_{mtrophy,n} \quad (161)$$

$$\frac{dR_{O2,n}}{dt} = F_{diff,O2,n} - 2F_{nit,n} - F_{ammon,n} - 2F_{mtrophy,n} \quad (162)$$

$$\frac{dR_{H2O,n}}{dt} = F_{ammon,n} + \frac{148.4}{106}F_{denit,n} + F_{nit,n} + 2F_{mtrophy,n} + F_{precip,n} + \frac{1}{2}F_{revwthr,n} + 3(F_{sorb,n} - F_{burial,FePO4,n}) - F_{diss,n} \quad (163)$$

$$\frac{dR_{FeOH3,n}}{dt} = F_{sed,FeOH3,n} - F_{sorb,n} - F_{burial,FeOH3,n} \quad (164)$$

$$\frac{dR_{FePO4,n}}{dt} = F_{sed,FePO4,n} + F_{sorb,n} - F_{burial,FePO4,n} \quad (165)$$

2.9.4. Deep Ocean

$$\frac{dR_{N2,d}}{dt} = F_{mix,N2,d} + \frac{42}{106}F_{denit,d} - F_{diff,N2,z} \quad (166)$$

$$\frac{dR_{RN,d}}{dt} = F_{mix,RN,d} + \frac{16}{106}(F_{ammon,d} + F_{denit,d} + F_{methgen,d}) - F_{nit,d} - F_{diff,RN,z} \quad (167)$$

$$\frac{dR_{HNO3,d}}{dt} = F_{mix,HNO3,d} + F_{nit,d} - \frac{84.4}{106}F_{denit,d} - F_{diff,HNO3,z} \quad (168)$$

$$\frac{dR_{H3PO4,d}}{dt} = F_{mix,H3PO4,d} + \frac{1}{106}(F_{ammon,d} + F_{denit,d} + F_{methgen,d}) - F_{sorb,d} - F_{diff,H3PO4,z} \quad (169)$$

$$\frac{dR_{Nod}}{dt} = \frac{16}{106}(F_{export,OC} - F_{ammon,d} + F_{denit,d} + F_{methgen,d} + F_{sed,OC,z}) \quad (170)$$

$$\frac{dR_{OP,d}}{dt} = \frac{1}{106}(F_{export,OC} - F_{ammon,d} + F_{denit,d} + F_{methgen,d} + F_{sed,OC,z}) \quad (171)$$

$$\frac{dR_{OC,d}}{dt} = F_{export,OC} - F_{ammon,d} - F_{denit,d} - F_{methgen,d} - F_{sed,OC,z} \quad (172)$$

$$\frac{dR_{CaCO3,d}}{dt} = F_{export,CaCO3} + F_{precip,d} - F_{diss,d} - F_{sed,CaCO3,z} \quad (173)$$

$$\frac{dR_{TA,d}}{dt} = F_{mix,TA,d} + 2F_{diss,d} + \frac{16}{106}(F_{ammon,d} + F_{denit,d} + F_{methgen,d}) + \frac{84.4}{106}F_{denit,d} - 2F_{precip,d} - 2F_{nit,d} - F_{diff,TA,z} \quad (174)$$

$$\frac{dR_{DIC,d}}{dt} = F_{mix,DIC,d} + F_{ammon,d} + F_{denit,d} + \frac{1}{2}F_{methgen,d} + F_{mtrophy,d} + F_{diss,d} - F_{precip,d} - F_{diff,DIC,z} \quad (175)$$

$$\frac{dR_{CH4,d}}{dt} = F_{mix,CH4,d} + \frac{1}{2}F_{methgen,d} - F_{mtrophy,d} - F_{diff,CH4,z} \quad (176)$$

$$\frac{dR_{O2,d}}{dt} = F_{mix,O2,d} - 2F_{nit,d} - F_{ammon,d} - 2F_{mtrophy,d} - F_{diff,O2,z} \quad (177)$$

$$\frac{dR_{H2O,d}}{dt} = F_{ammon,d} + \frac{148.4}{106}F_{denit,d} + F_{nit,d} + 2F_{mtrophy,d} + F_{precip,d} + 3F_{sorb,d} - F_{diss,d} \quad (178)$$

$$\frac{dR_{FeO,d}}{dt} = F_{mantle,Fe} + F_{mix,FeO,d} \quad (179)$$

$$\frac{dR_{FeOH3,d}}{dt} = F_{export,FeOH3} - F_{sorb,d} - F_{sed,FeOH3,z} \quad (180)$$

$$\frac{dR_{FePO4,d}}{dt} = F_{export,FePO4} + F_{sorb,d} - F_{sed,FePO4,z} \quad (181)$$

2.9.5. Pelagic Sediments

$$\frac{dR_{N2,z}}{dt} = F_{diff,N2,z} + \frac{42}{106}F_{denit,z} \quad (182)$$

$$\frac{dR_{RN,z}}{dt} = F_{diff,RN,z} + \frac{16}{106}(F_{ammon,z} + F_{denit,z} + F_{methgen,z}) - F_{nit,z} - F_{hyd} \quad (183)$$

$$\frac{dR_{HNO3,z}}{dt} = F_{diff,HNO3,z} + F_{nit,z} - \frac{84.4}{106}F_{denit,z} \quad (184)$$

$$\frac{dR_{H3PO4,z}}{dt} = F_{diff,H3PO4,z} + \frac{1}{106}(F_{ammon,z} + F_{denit,z} + F_{methgen,z}) + F_{scav,z} - F_{sorb,z} - F_{burial,PO4,z} \quad (185)$$

$$\frac{dR_{ON,z}}{dt} = \frac{16}{106}(F_{sed,OC,z} - F_{ammon,z} - F_{denit,z} - F_{methgen,z}) - F_{burial,ON,z} \quad (186)$$

$$\frac{dR_{OP,z}}{dt} = \frac{1}{106}(F_{sed,OC,z} - F_{ammon,z} - F_{denit,z} - F_{methgen,z}) - F_{burial,OP,z} - F_{scav,z} \quad (187)$$

$$\frac{dR_{OC,z}}{dt} = F_{sed,OC,z} - F_{ammon,z} - F_{denit,z} - F_{methgen,z} - F_{burial,OC,z} \quad (188)$$

$$\frac{dR_{CaCO3,z}}{dt} = F_{sed,CaCO3,z} + F_{precip,z} + \frac{1}{2}F_{sfw} - F_{diss,z} - F_{burial,CaCO3,z} \quad (189)$$

$$\frac{dR_{TA,z}}{dt} = F_{diff,TA,z} + 2F_{diss,z} + \frac{16}{106}(F_{ammon,z} + F_{denit,z} + F_{methgen,z}) + \frac{84.4}{106}F_{denit,z} - 2F_{precip,z} - F_{revwthr,z} - 2F_{nit,z} - F_{hyd} \quad (190)$$

$$\frac{dR_{DIC,z}}{dt} = F_{diff,DIC,z} + F_{ammon,z} + F_{denit,z} + \frac{1}{2}F_{methgen,z} + F_{mtrophy,z} + F_{diss,z} - F_{precip,z} - F_{sfw} \quad (191)$$

$$\frac{dR_{CH4,z}}{dt} = F_{diff,CH4,z} + \frac{1}{2}F_{methgen,z} - F_{mtrophy,z} \quad (192)$$

$$\frac{dR_{O2,z}}{dt} = F_{diff,O2,z} - 2F_{nit,z} - F_{ammon,z} - 2F_{mtrophy,z} \quad (193)$$

$$\frac{dR_{H2O,z}}{dt} = F_{ammon,z} + \frac{148.4}{106}F_{denit,z} + F_{nit,z} + 2F_{mtrophy,z} + F_{precip,z} + \frac{1}{2}F_{revwthr,z} + 3(F_{sorb,z} - F_{burial,FePO4,z}) + \frac{1}{2}F_{hyd} - F_{diss,z} \quad (194)$$

$$\frac{dR_{FeOH3,z}}{dt} = F_{sed,FeOH3,z} - F_{sorb,z} - F_{burial,FeOH3,z} \quad (195)$$

$$\frac{dR_{FePO4,z}}{dt} = F_{sed,FePO4,z} + F_{sorb,z} - F_{burial,FePO4,z} \quad (196)$$

2.9.6. Unreactive Sediments

Note: the term $r_o = \frac{R_{CaCO3,o}}{R_{CaCO3,u}+R_{CaCO3,o}}$, the ratio of $CaCO_3$ contained within the ocean crust versus the total $CaCO_3$ in both unreactive sediments and ocean crust.

$$\frac{dR_{SP,u}}{dt} = F_{burial,FePO4,z} - F_{acc,SP} - F_{subduct,SP} - F_{cryst,SP} \quad (197)$$

$$\frac{dR_{CP,u}}{dt} = F_{burial,PO4,z} - F_{acc,CP} - F_{subduct,CP} - F_{cryst,CP} \quad (198)$$

$$\frac{dR_{ON,u}}{dt} = F_{burial,ON,z} - F_{acc,ON} - F_{volc,ON} - F_{subduct,ON} - F_{cryst,ON} \quad (199)$$

$$\frac{dR_{OP,u}}{dt} = F_{burial,OP,z} - F_{acc,OP} - F_{subduct,OP} - F_{cryst,OP} \quad (200)$$

$$\frac{dR_{OC,u}}{dt} = F_{burial,OC,z} - F_{volc,OC} - F_{acc,OC} - F_{subduct,OC} \quad (201)$$

$$\frac{dR_{CaCO3,u}}{dt} = F_{burial,CaCO3,z} - (1 - r_o)(F_{volc,CaCO3} - F_{acc,CaCO3} - F_{subduct,CaCO3}) \quad (202)$$

$$\frac{dR_{FeOH3,u}}{dt} = F_{burial,FeOH3,z} + F_{burial,FePO4,z} - F_{acc,FeOH3} - F_{subduct,FeOH3} - F_{cryst,FeOH3} \quad (203)$$

2.9.7. Continental Crust

$$\frac{dR_{NH4,c}}{dt} = F_{acc,NH4} + F_{cryst,NH4} + F_{cryst,ON} - F_{wthr,NH4} - F_{meta,NH4} \quad (204)$$

$$\frac{dR_{SP,c}}{dt} = F_{mantle,P} + F_{burial,FePO4,n} + F_{acc,SP} + F_{cryst,CP} + F_{cryst,SP} + F_{cryst,OP} - F_{wthr,SP} \quad (205)$$

$$\frac{dR_{CP,c}}{dt} = F_{burial,PO4,n} + F_{acc,CP} + F_{meta,OP} - F_{wthr,CP} \quad (206)$$

$$\frac{dR_{ON,c}}{dt} = F_{burial,ON,n} + F_{acc,ON} - \frac{16}{106}F_{wthr,oxi} - F_{meta,OC} \quad (207)$$

$$\frac{dR_{OP,c}}{dt} = F_{burial,OP,n} + F_{acc,OP} - \frac{1}{106}F_{wthr,oxi} - F_{meta,OP} \quad (208)$$

$$\frac{dR_{OC,c}}{dt} = F_{burial,OC,n} + F_{acc,OC} + \frac{9}{10}F_{terrprod} - F_{wthr,oxi} - F_{meta,OC} \quad (209)$$

$$\frac{dR_{CaCO3,c}}{dt} = F_{burial,CaCO3,n} + F_{acc,CaCO3} - F_{wthr,CaCO3} - F_{meta,CaCO3} \quad (210)$$

$$\frac{dR_{Fe2SiO4,c}}{dt} = F_{mantle,Fe2SiO4} - F_{wthr,Feox} \quad (211)$$

$$\frac{dR_{FeOH3,c}}{dt} = F_{burial,FeOH3,n} + F_{burial,FePO4,n} + F_{acc,FeOH3} + F_{cryst,FeOH3} \quad (212)$$

$$\frac{dR_{Fe2O3,c}}{dt} = F_{wthr,Feox} \quad (213)$$

$$\frac{dR_{SiO3,c}}{dt} = F_{mantle,SiO3} \quad (214)$$

2.9.8. Oceanic Crust

$$\frac{dR_{NH4,o}}{dt} = F_{hyd} - F_{volc,NH4} - F_{acc,NH4} - F_{subduct,NH4} - F_{cryst,NH4} \quad (215)$$

$$\frac{dR_{CaCO3,o}}{dt} = F_{sfw} - r_o\left(F_{volc,CaCO3} - F_{acc,CaCO3} - F_{subduct,CaCO3}\right) \quad (216)$$

2.9.9. Upper Mantle

$$\frac{dR_{N,m}}{dt} = F_{subduct,NH4} + F_{subduct,ON} - F_{mantle,N} \quad (217)$$

$$\frac{dR_{P,m}}{dt} = F_{subduct,CP} + F_{subduct,OP} + F_{subduct,SP} - F_{mantle,P} \quad (218)$$

$$\frac{dR_{C,m}}{dt} = F_{subduct,CaCO3} + F_{subduct,OC} - F_{mantle,C} \quad (219)$$

$$\frac{dR_{Fe,m}}{dt} = F_{subduct,FeOH3} - F_{mantle,FeO} - 2F_{mantle,Fe2SiO4} \quad (220)$$

$$\frac{dR_{SiO3,m}}{dt} = -F_{mantle,SiO3} \quad (221)$$

2.9.10. Temperature

$$\frac{dT}{dt} = \frac{A_E}{M_{oc}c_p}\left((1-\alpha)\left(\frac{S(t)}{4}\right)\left(1+\frac{3}{4}\gamma_{IR}\right) - \sigma T^4\right) \quad (222)$$

2.9.11. Mass Conservation

These differential equations account for oxygen and hydrogen atoms lost and gained from fluxes including hydrogen escape to space, species that we do not explicitly track (such as SiO_2 or CaO) and speciation changes in

the otherwise unresolved mantle reservoir. Species lost from resolved reservoirs are added and species gained from unresolved reservoirs are subtracted.

$$\frac{dR_{H,x}}{dt} = F_{Hesc,H} - F_{cryst,ON} + 2F_{subduct,OC} + 3(F_{subduct,CP} + F_{subduct,SP} + F_{subduct,OP} - F_{mantle,P} + F_{subduct,ON} - f_{red} F_{mantle,N} + F_{subduct,FeOH3}) + 4(F_{subduct,NH4} - f_{red} F_{mantle,C}) \quad (223)$$

$$\frac{dR_{O,x}}{dt} = \frac{1}{2}(F_{revwthr,n} + F_{revwthr,z} + F_{hyd} - F_{wthr,sil} - F_{wthr,NH4} - F_{meta,NH4} - F_{volc,NH4}) + F_{subduct,OC} + F_{volc,CaCO3} + F_{meta,CaCO3} - F_{sfw} - F_{mantle,FeO} + 2(F_{wthr,Feox} - (1 - f_{red}) F_{mantle,C}) + 3(F_{subduct,CaCO3} + F_{subduct,FeOH3}) + 4(F_{subduct,CP} + F_{subduct,SP} + F_{subduct,OP} - F_{mantle,P} - F_{mantle,Fe2SiO4}) \quad (224)$$

2.10. Initial Conditions

The EONS model is run over 4 billion years from a initial starting point assumed to be characteristic of the Eoarchean, when life emerges. Initial conditions and model parameters and constants are included in the appendix. Many reservoirs are initialized at 0 mol; exceptions are noted in Table A1. We start with an Eoarchean solar flux (1,020 Wm^{-2}), higher mantle reductant influx ($\chi_{mantle} = 6$), and assume continental bodies at 5% modern emergence.

Carbon starts in the atmosphere as CO_2, and we assume higher atmospheric partial pressure is bolstered by higher ocean concentrations of DIC and alkalinity with no calcium carbonate. There is no OC in any reservoir, and atmosphere-ocean CH_4 starts at very low concentrations under the assumption of no biological source prior to 4 Ga. Nitrogen at the surface is mostly in the form of atmospheric or dissolved N_2, with some dissolved RN in the ocean and sediment reservoirs and no nitrate. Dissolved H_3PO_4 concentrations are low (0.2 μM; Bjerrum & Canfield, 2002). We further assume ferruginous ocean conditions ([FeO] = 10–7,000 μM; Swanner et al., 2020). Continents contain 5% of modern surface silicate-bound phosphorus, reduced iron, and SiO_3. All carbon, nitrogen, phosphorus, iron, and silicate not initialized in the atmosphere-ocean continents begins in the mantle.

3. Results: A Nominal Run of EONS

We present a run of EONS, which is initialized for Eoarchean (4 Ga) conditions, and runs through Earth history. This run reproduces the major features of Earths geochemical evolution with minimal forcings applied and ends with a good reproduction of preindustrial conditions. We refer to this as the nominal run.

The following sections detail tuning requirements for producing such a run, organized by major systems (biosphere, atmosphere, ocean, etc). We overview the model output for the system as it changes through time in stages, bracketed by the major transition events:

1. Eoarchean (4–3.5 Ga, up to initialization of photosynthesis)
2. Paleo-through Neo- Archean (3.5–2.3 Ga, up to the GOE)
3. Paleo-to middle Neo- Proterozoic (2.3–0.8 Ga, up to evolution of fungi)
4. Cryogenian (0.8–0.65 Ga, up to evolution of large organisms)
5. Ediacaran (0.65–0.4 Ga, up to evolution of vascular plants)
6. Devonian through modern (0.4 Ga - present)

We then discuss implications for understanding the Earth system as a whole. We highlight where the nominal run succeeds and falls short, and explain why key tuning choices were made and their implications for future experiments and further model refinement. Many of the chemical changes on the Earth's surface in the model run can be attributed to evolutionary developments; as such, we frame our discussion of the Earth system by first characterizing the evolutionary trajectory of the biosphere.

Table 3
Figure Color Scheme Summary

Species	Stochiometry	Color
Ammonia, organic nitrogen (ON)	NH_3	
Ammonium and total reduced N (RN)	NH_4^+	
Nitrate	HNO_3	
Dinitrogen	N_2	
Carbon dioxide and silicate	CO_2 and SiO_3	
Methane and organic carbon (OC)	CH_4 and CH_2O	
Dissolved inorganic carbon (DIC)	$CO_2 + HCO_3^- + CO_3^{2-}$	
Total alkalinity (TA)	Equation 6	
Calcium carbonate	$CaCO_3$	
Dissolved phosphoric acid, organic phosphorus (OP)	H_3PO_4	
Silicate-bound phosphate (SP) and Fe(III)-phosphate	H_3PO_4 and $FePO_4$	
Carbonate-bound phosphate (CP)	H_3PO_4	
Oxygen	O_2	
Ferrous iron and hydrogen	FeO and H	
Fayalite olivine and hematite	Fe_2SiO_4 and Fe_2O_3	
Iron hydroxide	$Fe(OH)_3$	

Note. A list of all of the species and their corresponding colors used in the model output figures. In general: red/oranges = nitrogen; greens = carbon; blues = phosphorus; yellows = oxygen; purples = iron. Some colors represent multiple species which are not plotted in the same figures.

We use a consistent color scheme for all evolution figures, where line colors correspond to species (either in the reservoir or produced/used in the flux being shown; Table 3). We denote estimates for fluxes and reservoirs given in the literature with symbols and error bars corresponding with a model output line. References for these estimates are provided in appendix Table A2. Model output excludes a 10 million year spin-up period, during which the atmosphere and oceans equilibrate.

3.1. Biosphere Evolution

The modeled biosphere is detailed in Figure 6, and described in detail in the following sections. The relative availability of key nutrients is shown in Figure 7.

3.1.1. Biosphere: Chronology

3.1.1.1. Stage 1

The pre-oxygenic photosynthesis biosphere is limited by reduced iron availability. Reduced iron levels gradually decrease as photoferrotrophy balances with mantle influx (Figure 6a), bringing the Eoarchean biosphere to a pseudo-steady state production flux of nearly 1×10^{12} mol C/yr at the end of this stage (Figure 6b). Phosphorus levels increase as iron levels equilibrate and from increasing continental weathering influx (Figure 6a). Fixation grows the available fixed nitrogen reservoir to approximately one tenth the modern surface reservoir at pseudo-steady state (Figures 6a and 6c). Figure 7 shows biosphere limitation by the relative availability of nitrogen to phosphorus; nitrogen is out of Redfield ratio with respect to phosphorus, resulting in increased productivity by anoxygenic nitrogen fixation. Both fixed N and phosphorus levels increase (Figure 6a) until the end of this stage due to photoferrotrophy being more strongly limited by reduced iron.

Remineralization is dominated by methanogenesis due to absent dissolved oxygen or nitrate (Figure 6d) returning most OC produced in productivity back to the dissolved nutrient reservoirs, with very little carbon buried as organics (Figure 6e). During this stage, the fraction of total (inorganic and organic) carbon buried as organic materials (f_{org}) is a function of extensive carbonate burial (discussed further in Section 3.6.1.1) as well as extended residence timescales in the reactive sediments from lower continental erosion (Section 2.3.2) and smaller organisms sinking more slowly out of the surface and deep oceans (Section 2.3.6); resulting extensive remineralization keeps burial efficiency (the percent of total productivity buried) low (Figure 6f).

3.1.1.2. Stage 2

Oxygenic photosynthesis evolves and rapidly dominates the biosphere, causing significant nutrient limitation through to the GOE as OM is preferentially buried in anoxic sediments. When the photosynthesizer population reaches its full extent following a growth period (Section 2.3.4) dissolved phosphorus level drops, bringing the ocean N:P closer to Redfield ratio, and the system enters a stage of significant phosphorus limitation for the next billion years (Figure 7). In this period, photosynthesis levels reach a pseudo-steady state level of approximately 1×10^{14} mol C/yr and OC burial fraction rises to approximately 3% (Figures 6b and 6e) as OC burial becomes increasingly more efficient (Figure 6f). Nitrogen fixation responds to phosphorus availability and nitrogen levels correspondingly plateau (Figure 6c), but the production of oxygen allows nitrification to expand the nitrate reservoir, which rapidly grows to approximately 10% of the total fixed nitrogen reservoir (Figure 6a). A transient peak in HNO_3 appears as increasing phosphorus limitation leads to a decline in demand for fixed N. Nitrate then declines to a new pseudo-steady state as denitrification rises in response; the availability of dissolved oxygen expands remineralization beyond methanogenesis to include ammonification (Figure 6d).

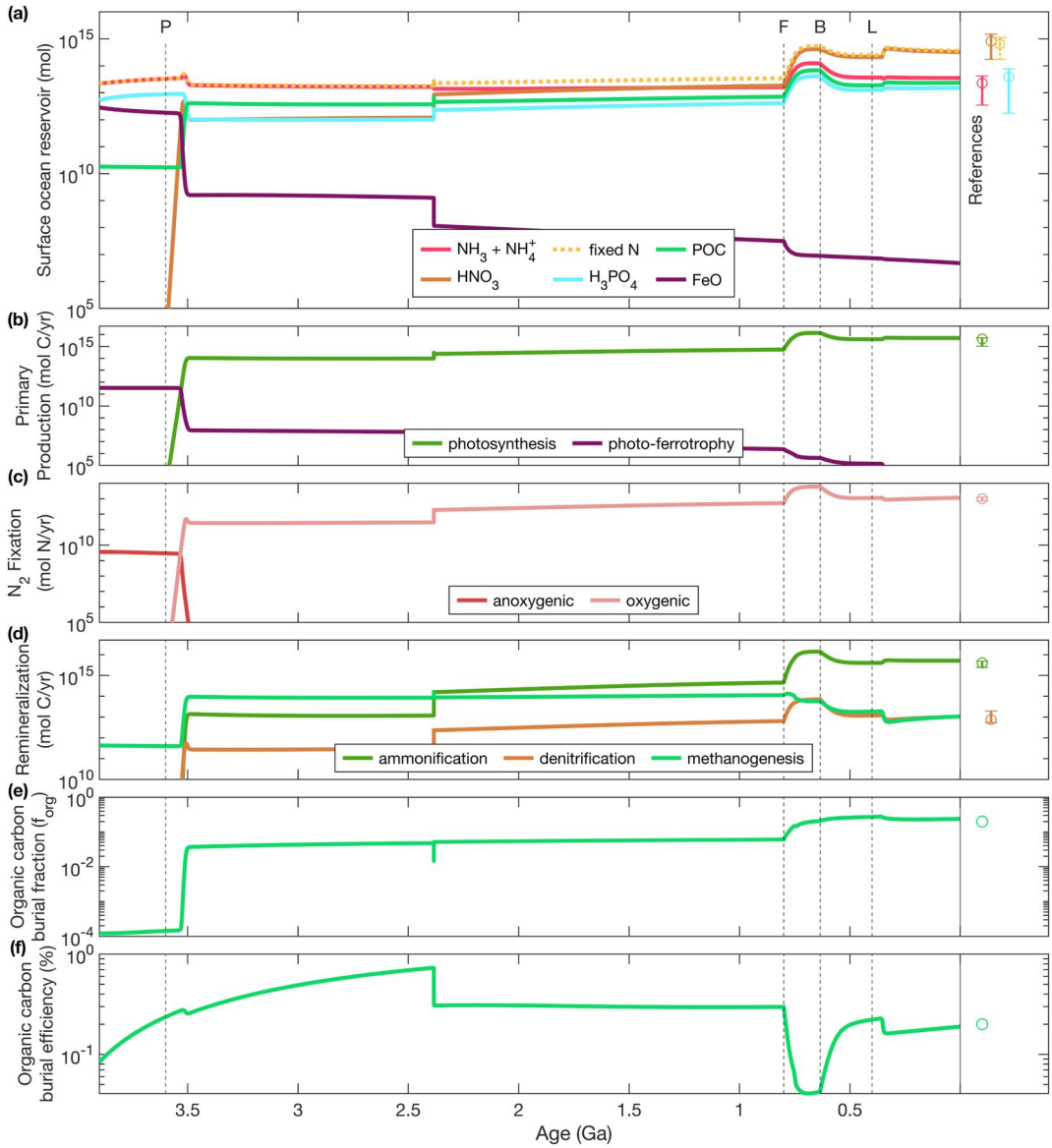

Figure 6. The evolution of biology. (a) All surface ocean nutrients; (b–d) primary production, nitrogen fixation, and remineralization fluxes (summed across all ocean/sediment reservoirs), respectively; (e) organic carbon (OC) burial fraction (f_{org}); (f) OC burial efficiency (total burial flux over primary production). Modern estimates for reservoirs and fluxes are denoted with symbols at the far right of each plot, with range estimates as vertical bars (citations in Table A2); the solid vertical line denotes the end of model output. Black dashed vertical lines denote forced evolutionary transitions: *P* for oxygenic photosynthesis, *F* for fungi, *B* for increased body sizes, and *L* for vascular land plants.

3.1.1.3. Stage 3

The post-GOE biosphere is denoted by a rapid shift toward aerobic processes (ammonification) at the expense of anaerobic processes (photo-ferrotrophy, methanogenesis; see Figures 6b and 6d) with a corresponding rise in oxygenated nutrients (nitrate) over reduced nutrients (ammonia/ammonium, FeO; see Figure 6a). The oxygen transition is further demarcated by a transient dip in OC burial (Figure 6e) as remineralization becomes more efficient along aerobic pathways (and because of perturbations within the carbonate system, discussed further in Section 3.6.1.2). Nitrogen increasingly becomes the limiting nutrient over this transition as denitrification increases (Figures 6d and 7). The post-GOE biosphere is characterized by a slow increase in nutrient availability (due to increased oxidative weathering) and a continuous decline in reduced nutrient reservoirs (Figure 6a). Organic carbon burial increases in lockstep with photosynthesis (Figure 6e), causing a persistent if slow expansion of the atmospheric oxygen reservoir (Section 3.2.1.3); stagnating burial efficiency suggests that

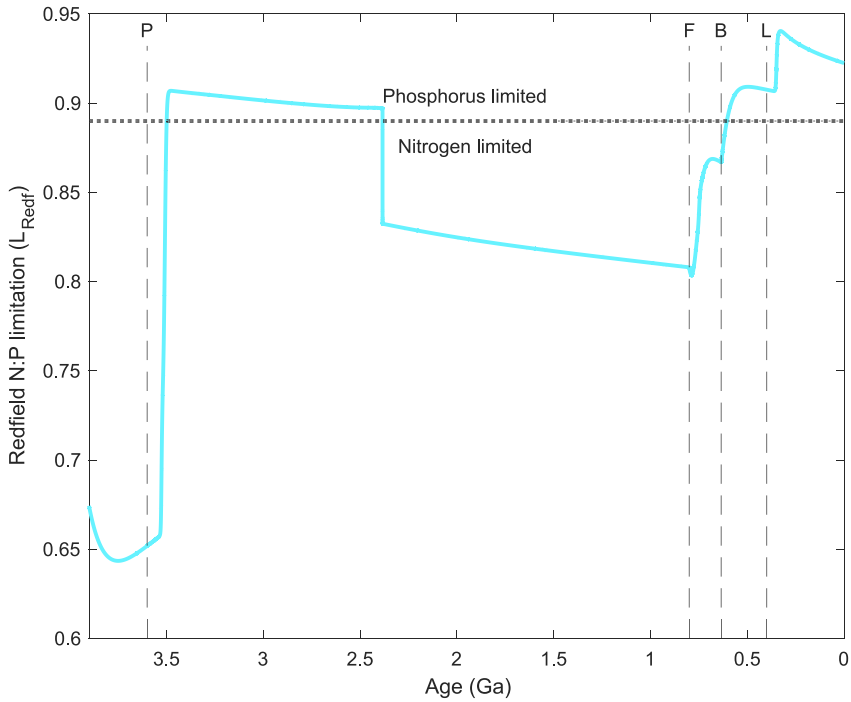

Figure 7. The evolution of nutrient limitations. Biological assimilation limitation by relative nitrogen to phosphorus availability. A smaller value indicates that available N:P is lower than typical Redfield ratio, 16:1, and nitrogen is the more limiting nutrient, promoting productivity via N-fixation over direct assimilation (Equations 31 and 26, respectively). A L_{Redf} value approaching 0.89 is denoted by the dotted horizontal line, indicating fixed N:P ratio is at Redfield ratio. Black dashed vertical lines denote forced evolutionary transitions: *P* for oxygenic photosynthesis, *F* for fungi, *B* for increased body sizes, and *L* for vascular land plants.

productivity and OC burial achieve pseudo-steady state through this stage (Figure 6f). Oxygenic fixation, ammonification, and denitrification fluxes increase slightly across the 1.6–0.8 Ga period, coincident with a slow decline in anoxic processes such as photo-ferrotrophy and methanogenesis (Figures 6b–6d). Productivity is approximately 40%–50% modern levels through the majority of this stage (Figure 6b).

3.1.1.4. Stage 4

The evolution of fungi at 0.7 Ga corresponds to a rapid influx of phosphorus with cascading effects for the biosphere. The post-GOE pseudo-steady state is disrupted by increased phosphorus influx to the ocean, boosting productivity beyond modern rates and resulting in an expansion of the OC pool and subsequent burial (Figures 6a and 6e). Photosynthesis and nitrogen fixation jump sharply; the latter easing nitrogen limitation (Figures 6a–6c and 7). Phosphorus returns to being the primary limiting nutrient on the system because of progressive oxygenation in the deep ocean and sediments inhibiting P scavenging and allowing nitrogen levels to equilibrate (see Section 3.3.1.4). Net primary productivity exceeds modern rates by the end of this stage (Figure 6b) and burial efficiency drops to its lowest point as remineralization by ammonification increases (Figures 6d and 6f).

3.1.1.5. Stage 5

The evolution of large-bodied organisms in the Ediacaran increases export and burial efficiency (Figures 6d and 6f), returning surface nutrient levels and productivity fluxes to near modern levels (6 a-c). Organic carbon burial continues its massive expansion (Figure 6e), increasing from near 5%–20% at 0.65 Ga at the end of this stage.

3.1.1.6. Stage 6

Land colonization by vascular plants triggers the full oxygenation of the deep ocean and evolves the biosphere to its modern state. Additional oxygen production by the new terrestrial biosphere at 0.4 Ga increases deep ocean oxygenation (discussed further in Section 3.2.1.6), resulting in nitrate dominating the fixed nitrogen reservoir

(Figure 6a) and declining anaerobic remineralization fluxes (Figure 6d). Lowered denitrification reduces fixed N loss, and thus causes a slight decline in fixation and a jump in nitrogen availability as a nutrient (Figures 6c and 7).

Carbon burial fraction declines across this period from a high of 25%–20% following this final evolutionary transition (Figure 6e). Vascular land plants enhance silicate and carbonate weathering fluxes, increasing ocean pH (discussed further in Sections 3.2.1.6 and 3.6.1.6); the result is increased carbonate precipitation over dissolution, which contributes to the decline in OC burial. This decline is also a function of the increasing oxygenation of the deep ocean, which expands ammonification to previously anoxic bottom waters and sediments and decreases burial efficiency (Figure 6f).

3.1.2. Biosphere: Tuning Requirements

Early primary production by photo-ferrotrophy is highly sensitive to the influx of reduced iron from the mantle; a higher influx from a more reducing or faster convecting mantle would likely result in higher pseudo-steady state primary production. Assuming slower sinking rates prior to the evolution of large organisms is important in bolstering early primary production; faster sinking in the anoxic ocean would increase burial efficiency but also sequester more nutrients onto the continents and make the system less productive overall. Similarly, it is important for the early biosphere's productivity that residence time for particulate matter in the sediments is longer than at present (as controlled by erosional influx, χ_{eros}, a function of relative continent size); longer residence times in the sediments allows for more remineralization and returns nutrients more efficiently to their dissolved reservoir. Constant modern sediment residence timescales in an anoxic deep ocean would yield significantly higher f_{org} but also would inhibit primary production by sequestering key nutrients. Phosphorus weathering and burial flux balance is also key to the biosphere; we comment on this further in Section 3.3.2.

3.1.3. Biosphere: Implications

Biosphere productivity has increased through geologic time as more efficient pathways emerge. Characteristic of this model's design is a fundamental electron-donor limitation on primary productivity prior to the evolution of oxygenic photosynthesis; as our only anoxygenic pathway for primary production is photo-ferrotrophy, our biosphere is initially limited by FeO availability and is approximately 4 orders of magnitude lower than modern day. Fixation and remineralization are subsequently lower than modern rates by the same magnitude (Figures 6a–6d). Other organisms utilizing H_2S, H_2, and CO as electron donors have not been considered here and may very well have aided in maintaining higher primary productivity, perhaps even comparable to the modern level, during this stage (Kharecha et al., 2005). Additionally, higher or additional influxes of FeO into the system would allow for a higher level of primary production at pseudo-steady state. This model suggests that the Proterozoic biosphere had considerable levels of primary productivity, perhaps within two orders of magnitude of the modern biosphere; this is well within some recent estimates of Archean and Proterozoic primary production ranging from 1×10^{-3} to 1×10^{-1} times modern levels (Crockford et al., 2023).

Nitrogen and phosphorus limitations alternate across the GOE. Nutrient limitations primarily determine the efficiency of the ocean biosphere, and both nitrogen and phosphorus have been the ultimate limiting nutrient at different times. There has been a long running debate regarding how phosphorus-limited the Archean biosphere was. Conventional wisdom assumed low dissolved phosphorus would arise as a result of limited continental weathering (Hao et al., 2020) or extensive scavenging by iron oxides (Bjerrum & Canfield, 2002; Jones et al., 2015; Rego et al., 2023); to the contrary, carbonate minerals in Archean stromatolites show enrichment in P relative to today (Crockford & Halevy, 2022; Ingalls et al., 2022), implying that the biosphere was limited by electron donors rather than phosphorus. Our nominal run suggests that phosphorus was less limiting than nitrogen during the Eoarchean and during the majority of the Proterozoic (see Figure 7); these periods are discussed in Sections 3.3.1.1 and 3.3.1.3. We do not see any indication that the onset of coupled nitrification-denitrification causes a decrease in the fixed nitrogen reservoir, and we do not see an extensive nitrogen limited phase causing the delay between photosynthesis evolution and the GOE as predicted by other models (Fennel et al., 2005).We do, however, see nitrogen limiting conditions preceding photosynthesis evolution and in the post-GOE stage. The stalled expansion of the fixed N reservoir is apparently caused by lowered fixation, which itself is limited by the availability of phosphorus (Section 2.4.1.3). Both nutrients are quite limiting in the period between 3.5 and 2.3 Ga, coincident with a rapid rise in OM burial efficiency (Figures 6e and 6f), suggesting that burial of OM and removal of nutrients from the system greatly contributes to the slow rise in oxygen; this is not wholly

inconsistent with the hypothesis that the GOE delay is a function of OC accumulation onto continental bodies (Peters & Husson, 2017). Both nutrient limitation and the gradual increase of oxygen sources over sinks could plausibly contribute to the delay.

3.2. Atmosphere-Ocean and Climate Evolution

The evolution of the modeled atmosphere and climate is shown in Figure 8 and the ocean is shown in Figure 9.

3.2.1. Atmosphere-Ocean: Chronology

3.2.1.1. Stage 1

Ocean chemistry is in equilibrium with the atmosphere, with limited influxes from the continents. Dinitrogen and CO_2 rapidly become the largest components of the pre-photosynthesis atmosphere, owing to mantle outgassing and the limited draws of nitrogen fixation and continental weathering, respectively, in this period. Most CH_4 is biologically sourced (only 1% of mantle carbon outgassed is CH_4), and as such its atmospheric level is limited by biosphere production via methanogenesis. Ammonia sources are similarly primarily biological, bolstered by a small fraction of mantle nitrogen outgassing, and this species has the additional draw of biosphere uptake. Nutrient species (RN and H_3PO_4) gradually increase with fixation and silicate-bound phosphorus weathering, respectively (Figures 9c and 9e compared with Figure 6c and Section 3.3.1.1); OC is in pseudo-steady state (Figure 9f), reflecting photo-ferrotrophy levels (Figure 6b) and influencing dissolved RN and H_3PO_4 at the end of this stage. Relatively low ocean pH and high demand in productivity in this period (Figures 7 and 9i) limits NH_3 speciation and gas exchange into the atmosphere; for these reasons, NH_3 partial pressure is low throughout this stage and there is negligible radiative forcing from this greenhouse gas (Figure 8b).

Carbonate chemistry is in considerable flux as air-sea gas exchange and the initialization of the inorganic carbon pump gradually draws carbon from the atmosphere into the ocean and continents; this also causes the gradual rise in ocean pH (Figures 9g–9j; discussed further in Section 3.6.1.1). Carbon dioxide equilibrates with the ocean to approximately 20 PAL at the start of this stage and maintains pseudo-steady state at this level, providing the majority of the radiative forcing for this period (Figures 8a and 8b).

3.2.1.2. Stage 2

The evolution of oxygenic photosynthesis is initially a minor disruption to atmospheric chemistry, introducing oxygen to the ocean and limiting the reservoirs of N and P. The evolution of photosynthesis initiates at the start of this stage; the gradual increase in oxygen following 3.4 Ga results from reductant sequestration via OC burial (Figure 6e). As the fraction of carbon buried with organics is not a defined parameter but an output in our model, the timing of the GOE is primarily controlled by the surface reducing capacity as parameterized by relative mantle reductant outgassing (χ_{mantle}); we comment further on this control in Section 3.2.2.

Oxygenic photosynthesis initiates a gradual rise in oxygen across the next billion years. Increased productivity boosts OC reservoirs, especially in the neritic and pelagic sediments (Figure 9f) driving a rise in f_{org} (Figure 6e). Figure 9a shows dissolved oxygen rising sharply in all ocean and sediment reservoirs immediately after photosynthesis evolution; this corresponds with an increase in nitrification and expansion of the dissolved nitrate reservoir (Figure 9d) and a decline in surface ocean methane (Figure 9b). Atmospheric methane is initially boosted by enhanced productivity inducing more methanogenesis but declines as more oxygen is produced until the GOE (Figures 6d and 8a). Higher nutrient demand results in a sharp drop in surface ocean RN and H_3PO_4 in Figures 9c and 9e; atmospheric NH_3 drops as demand on fixed N increases (Figures 6c and 8a). Prior to the GOE, the carbonate system is in pseudo-steady state (Figures 9g–9j), with near neutral pH.

3.2.1.3. Stage 3

Oxygen enters into the bistable range with methane around 2.3 Ga and rapidly transitions from around 10^{-6} PAL to almost 10^{-2} PAL; following the GOE, oxygen rises more slowly as productivity becomes increasingly nitrogen limited (Figure 7) and enters into a new pseudo-steady state with methane production. The ocean and sediments become increasingly oxygenated (although the deep ocean and pelagic sediments are still suboxic; Figure 9a). At the same time, methane in the surface ocean rebounds as methanogenesis experiences a slight, transient increase with higher productivity export to the suboxic deep ocean (Figures 6d and 9b); this boosts atmospheric CH_4 levels

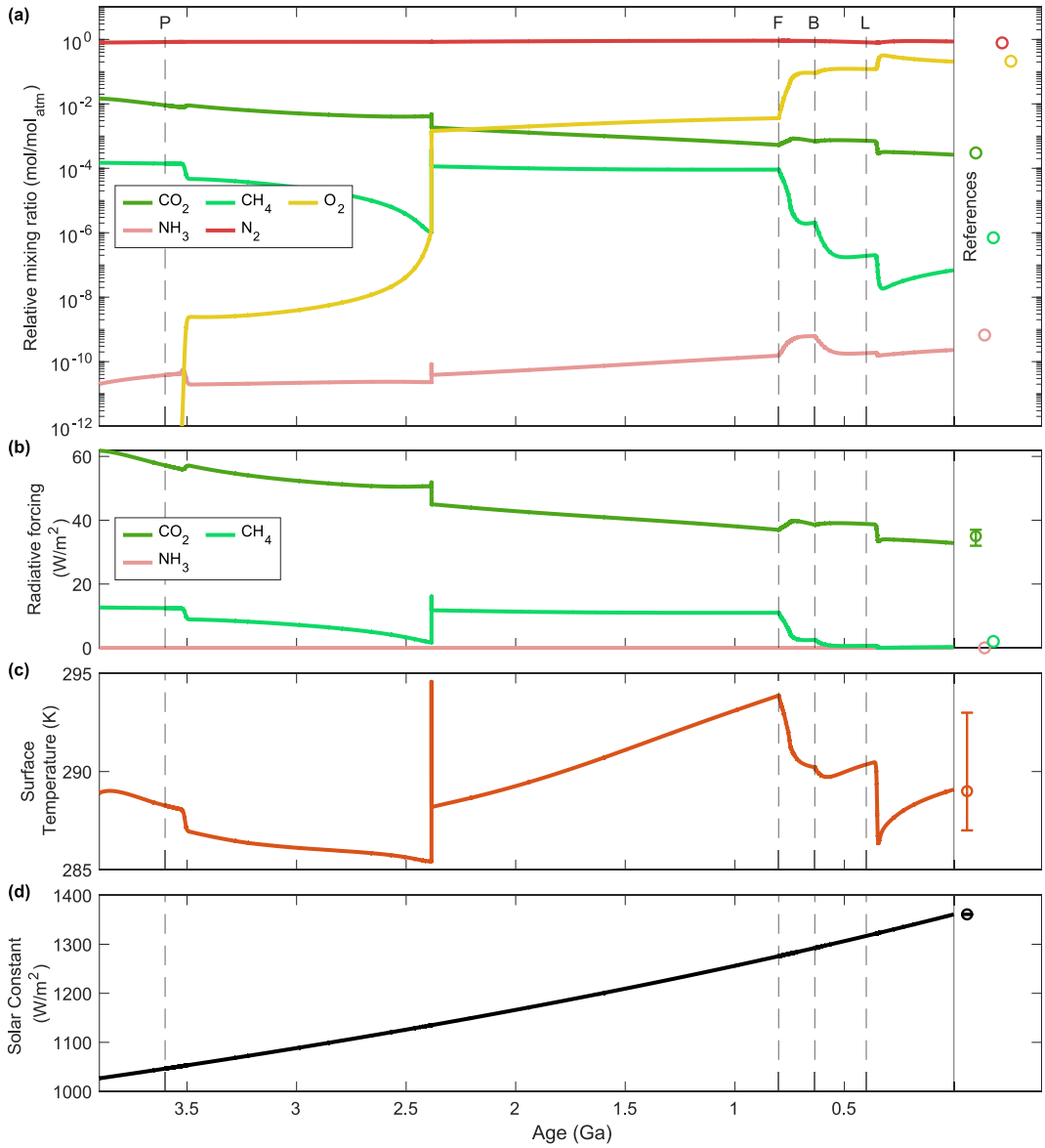

Figure 8. The evolution of the atmosphere and climate. (a) atmospheric composition; note mixing ratios are moles of the gas divided by total moles in a 1 bar atm, (b) radiative forcing by greenhouse gases (Wm^{-2}), (c) surface temperature (K), and (d) prescribed evolution of solar constant (Wm^{-2}). Modern estimates for reservoirs and fluxes are denoted with symbols at the far right of each plot, with range estimates as vertical bars (citations in Table A2); the solid vertical line denotes the end of model output. Black dashed vertical lines denote forced evolutionary transitions: *P* for oxygenic photosynthesis, *F* for fungi, *B* for increased body sizes, and *L* for vascular land plants.

to a pre-oxygenic photosynthesis high and raises atmospheric temperature (Figure 8c). Nitrate continues to expand while RN levels stagnate (Figures 9c and 9d). The Mesoproterozoic "boring billion" in our model is characterized by little change in atmosphere-ocean chemistry, continuing pseudo-steady state across all reservoirs.

The climate shifts from cooling to rapid warming across the GOE transition. Atmospheric CO_2 is relatively stable going into the GOE, bolstered by increased methane oxidation (see Section 3.5.1.3); the subsequent rise in CH_4 leads to a punctuated warming event that drives enhanced silicate weathering and stabilizes the climate at a higher temperature with increased CH_4 radiative forcing (Figures 8a–8c; see Section 3.6.1.3). The surface generally warms throughout this stage, with the exception of a brief cooling period coincident with the start of the GOE and CH_4 decline; gradual warming is generally a function of solar forcing parameter and should not be misconstrued

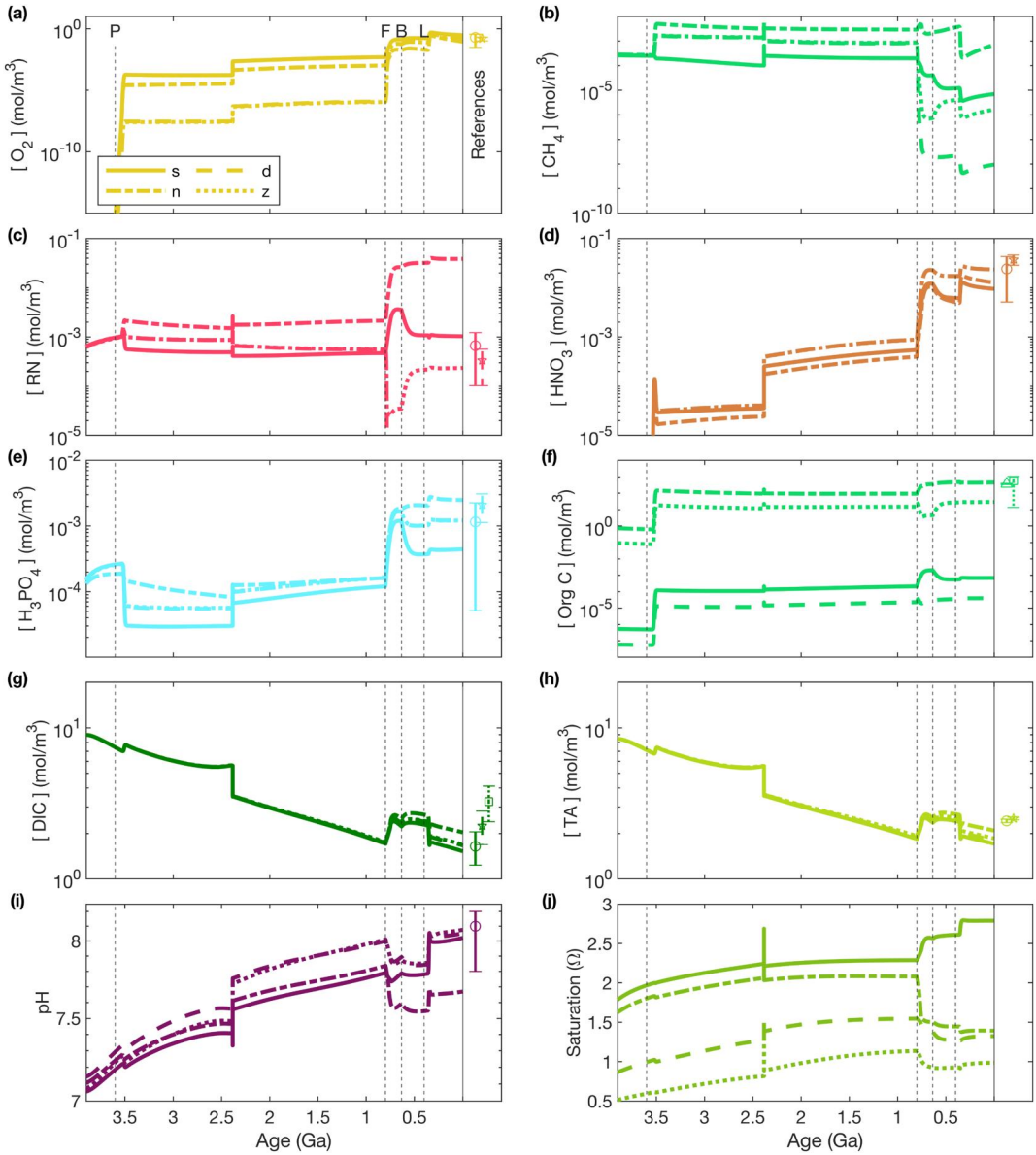

Figure 9. The evolution of ocean reservoirs. In the legend, *s*, *n*, *d*, and *z* denote surface ocean, neritic (shelf) sediments, deep ocean, and pelagic sediments, respectively. (a–f) Concentrations of reactive species (oxygen, methane, reduced nitrogen (RN), nitrate, phosphate, and organic carbon, respectively; note that RN is comprised of NH_3 and NH_4^+ in equilibrium). (g–j) Inorganic carbon system parameters (dissolved inorganic carbon, total alkalinity, pH, and carbonate saturation, respectively). Modern estimates for reservoirs and fluxes are denoted with symbols at the far right of each plot, with range estimates as vertical bars (citations in Table A2); the solid vertical line denotes the end of model output. Black dashed vertical lines denote forced evolutionary transitions: *P* for oxygenic photosynthesis, *F* for fungi, *B* for increased body sizes, and *L* for vascular land plants.

as negating the reality of climate cooling events that may have arisen during this period due to ice-albedo feedbacks that we do not resolve here.

Post-GOE warming accelerates the inorganic carbon cycle, triggering a sharp decline in DIC and alkalinity and disrupting carbonate saturation state across all ocean/sediment reservoirs as pH increases (Figures 9g–9j). The temperature increase enhances continental weathering, alkalinity influx, and contributes to enhanced carbonate burial evidenced by spiking carbonate saturation corresponding to a dip in f_{org} (Figures 6e and 9j; discussed further in Section 3.6.1.3). While the nutrient and oxygen levels in the ocean revert to a new pseudo-steady state in the aftermath of the GOE, the carbonate system continues its longterm trend of CO_2 sequestration. Larger

continents and higher temperatures slowly increase silicate and carbonate weathering's draw on atmospheric CO_2, transferring DIC and alkalinity to the ocean and continuing a rise in pH into the Neoproterzoic (Figures 8a and 9i).

3.2.1.4. Stage 4

The evolution of fungi upends pseudo-steady state by boosting productivity and causing a major acceleration of oxygen's growth, significant climatic cooling, and shifting the limiting nutrient paradigm again. This finding is broadly consistent with theories surrounding the connection between land colonization by lichens and fungi and increasing oxygenation in the Neoproterozoic (Heckman et al., 2001; Lenton & Watson, 2004). The influx of phosphorus spurs massive increases in primary production and a jump in atmosphere-ocean oxygen level that results in a nearly fully oxygenated ocean (Figures 6b, 8a, 9a, and 9b). Organic carbon levels in the surface ocean rise with productivity but decline in the pelagic sediments as increased dissolved oxygen there allows for extensive ammonification and crashing methane production, causing a decline in all atmosphere-ocean CH_4 reservoirs (Figures 6d, 8a, 9b, and 9f). Dissolved RN and atmospheric NH_3 increase with fixation (Figures 6c, 8a, and 9c); we comment on the ammonia excursion further in Section 3.4.1.3.

Carbonate saturation in the sediments and deep ocean declines sharply, resulting in widespread carbonate dissolution and leading to the massive expansion of f_{org} despite little change in total OC reservoirs (Figures 6e and 9j); as less carbon is buried as inorganic material, the fraction buried as organics rises. Declining pH and carbonate saturation and the corresponding bump in atmospheric CO_2 at 0.75 Ga (Figures 8a, 9i, and 9j) are discussed in further detail in Section 3.6.1.4. The small increase in CO_2 from this feedback partially compensates for the decline in CH_4 radiative forcing, such that the surface temperature drops only a few degrees (Figures 8b and 8c).

3.2.1.5. Stage 5

The evolution of large bodied organisms causes a decline in OC in the surface ocean as export efficiency increases and a shift in nutrient limitations (Figures 7, 9c, 9e, and 9f), discussed earlier in Section 3.1.1.5. Faster OC export and declining carbonate saturation lead to increasing f_{org} following this transition (Figures 6e, 9f, and 9j).

3.2.1.6. Stage 6

The Phanerozoic atmosphere-ocean system is a function of colonization of land by vascular plants, which completes the rise of oxygen to beyond 1 PAL and full oxygenation of the deep ocean during the Carboniferous as the terrestrial biosphere emerges (Figures 8a, 9a, and 9b). Nutrients and OC reach their modern levels during this period as the biosphere becomes aerobic and continental influxes reach modern rates (Figures 9c–9f); enhanced silicate/carbonate weathering and productivity causes a drop in CO_2 and a corresponding rise in pH (Figures 6b, 8a, and 9i and Section 3.6.1.6). After a sharp temperature decline at the 0.4 Ga transition, warming resumes following increasing solar flux (Figures 8c and 8d). Atmospheric methane ends up lower than modern levels even with additional production in the simple terrestrial biosphere; this indicates a missing component or perhaps over-simplification in either the biological methane cycle or photochemical interactions, particularly methane oxidation.

3.2.2. Atmosphere-Ocean: Tuning Requirements

This model interactively resolves the GOE, but timing and tempo of this transition can be significantly modified by two key parameters: mantle reductant output and continental emergence. This nominal tuning arises from trying to fit these parameters as best as possible to their modern references and to evolve them within conservative limits. Mantle reductant output is the primary control on surface reducing capacity, curtailing oxygen levels. Continental emergence is a major control on the long-term sequestration of OC (and nutrients buried with OM); geologic sequestering of OC equals net oxygen production, but this competes with the effects of nutrient burial, which limits the expansion of the biosphere. The relationship between mantle reductant output tuning, OC burial, and atmospheric oxygenation is shown in Figure 10; many different GOE scenarios can occur, depending on the relative outflux of mantle reductants at the onset of photosynthesis but oxygenation occurs in all scenarios once enough OC has been buried and weathering supply of nutrients is sufficiently high.

Lower reductant flux requires less long-term OC burial for net oxygen production to overwhelm surface reducing capacity. The system's reducing capacity is encapsulated by the k_{oxy} parameter (Figures 10g and 10h), which is

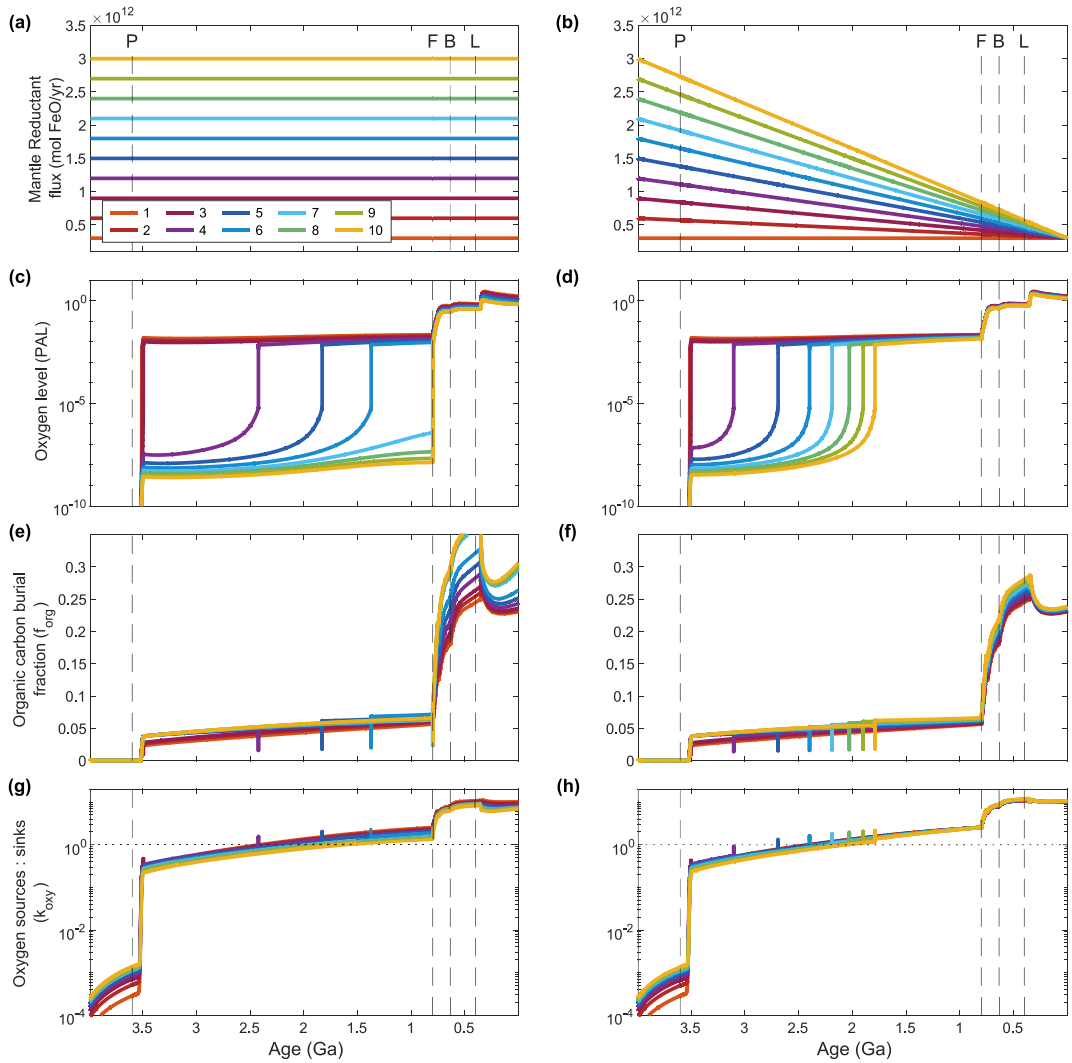

Figure 10. Timing the great oxidation event by changing only χ_{mantle} forcing. Left column (a, c, e) output from model runs with constant mantle reductant outflux, while right column (b, d, f) output from runs with linearly decreasing mantle reductant outflux. Line color denotes the value of χ_{mantle} (all other parameters in the model are kept the same). From top to bottom: (a and b) mantle reductant outfluxes (i.e., $\chi_{mantle}F_{mantle,FeO,0}$); (c and d) atmospheric oxygen levels (present atmospheric levels); (e and f) fraction of total carbon buried as organic matter (f_{org}); (g and h) oxygen source and sink balance (k_{oxy}; dotted horizontal line denotes unity). Lower mantle reductant influx is overwhelmed by lower net oxygen production (via the burial of organic carbon), resulting in earlier GOEs. Black dashed vertical lines denote forced evolutionary transitions: *P* for oxygenic photosynthesis, *F* for fungi, *B* for increased body sizes, and *L* for vascular land plants.

defined as the ratio of net oxygen production flux (via OC burial) to the flux of reducing species from the geosphere (Catling & Claire, 2005). When k_{oxy} exceeds unity, the atmosphere becomes oxidized. However, this is not a prerequisite for oxygenation and does not guarantee oxygenation in every case; a rapid switch from extremely to mildly reducing conditions follows the evolution of oxygenic photosynthesizers, with GOEs occurring for different mantle reductant fluxes as $k_{oxy} \geq 0.3$. Mantle reductant output is directly related to the minimum value of k_{oxy} required to initiate the GOE. In essence, higher mantle reductant output requires higher OC burial to reach the bistable tipping point, while cases with lower reductant output can reach this point with $k_{oxy} < 1$ (Figures 10g and 10h, curves for $\chi_{mantle} < 4$ and ≤ 5, respectively). In the case of constant mantle reductant output, it appears that k_{oxy} may have to exceed 1 in order to initiate a GOE (Figure 10g curve for $\chi_{mantle} = 10$). Since more reductant has accumulated at the surface in the constant flux scenarios, the system

requires even higher OC burial to oxidize; in the most extreme case, this only occurs when lichen and fungi evolve, spurring extensive primary production and dramatically increasing f_{org} (Figure 10e).

The GOE could have occurred at 2.3 Ga with a constant outflux of reductants, but only at a level 6–7x the modern rate (Figure 10c). Tuning χ_{mantle} depends mostly on the desired timing of the GOE, and acts to counteract the slow expansion of f_{org}. From the perspective of this model, constant $f_{org} = 0.2$ throughout geologic time, which is how some interpret the carbon isotope record (Hayes & Waldbauer, 2006; Marais et al., 1992; Schidlowski, 1988) is highly unlikely for many reasons, one being that such high burial would require significantly higher or more reducing mantle outgassing (or the emergence of the oxygenic biosphere much closer to the GOE) in order to result the tempo of surface oxygenation implied by the proxy record.

This atmosphere and climate history further depends on the treatment of continental growth; the initial atmospheric level of CO_2 and the overall trend of ocean pH and carbonate system behavior depends on atmosphere-ocean equilibrium, which is in large part determined by the magnitude of silicate weathering with punctuated transitions reflecting significant changes in the biosphere (particularly the GOE, evolution of fungi, and land plants). Larger initial continents would draw out CO_2 rapidly via weathering and make the early Archean climate very cold (see Section 3.6.2). Continental size further determines the initial ocean reservoir of phosphorus, which is exclusively sourced from the geosphere, and that in turn determines the pace of biosphere expansion (see Section 3.3.3). Our simplified treatment of mantle exchanges requires the initializing assumption of significant N and C retention in the mantle in order to properly tune the Eoarchean. Additionally, we assume a fixed fraction of the mantle is available to outgas to the surface, but vigorous plate tectonics in a hotter mantle could mean that a greater portion of the Archean upper mantle was outgassing (Noack et al., 2014), whereas outgassing would be inhibited under a stagnant lid regime (Guimond et al., 2021; Korenaga, 2006). A more realistic treatment of mantle thermal history and subduction controls would undoubtably allow for different initial conditions (Table A1).

Our nominal run atmospheric oxygen curve is shown in Figure 11 alongside constraints from different redox proxies in the literature; the timing and tempo of the rise of oxygen in this model fits extremely well within these constraints (Figure 11). The evolution of photosynthesis initiates a gradual rise in oxygen that enters into the bistable range with methane around 2.3 Ga with secondary transition as fungi and terrestrial plants evolve around 0.7 Ga and 0.4 Ga, respectively. The Phanerozoic transition initiates a Carboniferous aged oxygen overshoot which gradually returns to modern levels, a finding predicted by other models focusing on the Phanerozoic (Bergman et al., 2004; Berner, 2009; Lenton et al., 2018).

3.2.3. Atmosphere-Ocean: Implications

Atmosphere-ocean chemistry is strongly controlled by biological transitions and complete surface oxygenation requires a terrestrial biosphere. This modeled atmosphere-ocean reflects major biological transitions and continental emergence. The impetus for adding in oxygen production in a terrestrial biosphere that evolves in two steps with fungi and then with land plants (see Section 2.3.8) was an inability to achieve modern oxygen levels with modern ocean primary production and f_{org}; without this addition, oxygen in the atmosphere never exceeds 0.5 PAL, and the deep ocean and sediments remain anoxic. This tuning requirement is suggestive that the Phanerozoic started with suboxic deep oceans and that the modern ocean oxygen state was achieved relatively late, in the Devonian (Canfield et al., 2007; Krause et al., 2022) and reaffirms previous modeling results suggesting that modern oxygen levels were only achieved after the evolution of vascular land plants (Krause et al., 2018; Lenton et al., 2016; Ozaki & Reinhard, 2021).

The GOE and later expansion of the biosphere onto continents plausibly led to significant climate disruptions which may have resulted in mass extinctions. Our results suggest that, from biological feedbacks alone, it is likely that the GOE was followed by a relatively warm period for the climate. An initial rise in oxygen might have caused a rise in atmospheric methane and surface temperature, whereas later rises (corresponding with oxygenation of the deep ocean) likely caused climate cooling, particularly as vascular plants and terrestrial biospheres evolve. Prior to the GOE, there is a marked decline in atmospheric CH_4 and temperature, corresponding well to the timing of the Paleoproterozoic snowball event (Hoffman, 2013; Kirschvink et al., 2000; Warke et al., 2020). The GOE is accompanied by a rapid rise in atmospheric temperature and CH_4, a result of increased surface aerobic remineralization and productivity followed by extensive anaerobic remineralization in the deoxygenated deep ocean. This reverses into a rapid decline as the silicate weathering feedback kicks in; a

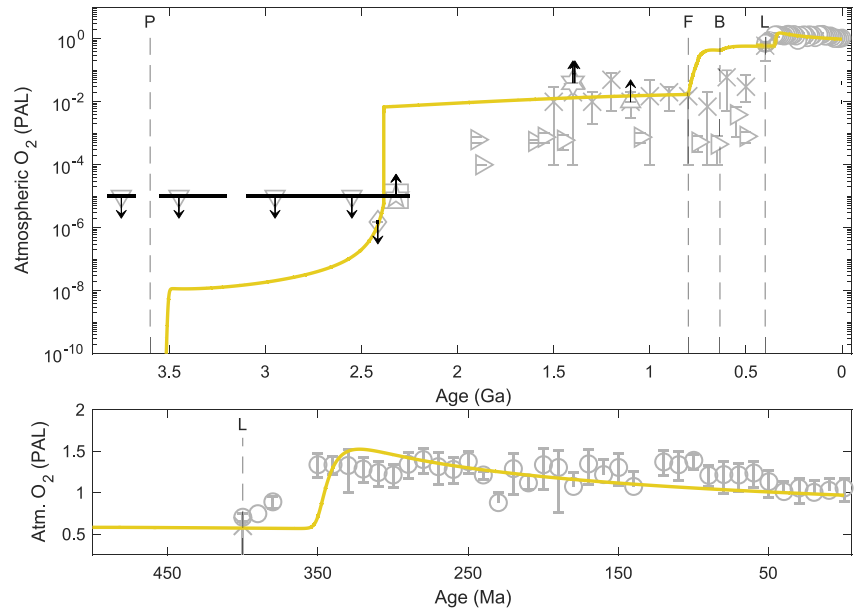

Figure 11. Oxygen curve and proxy compilation. Atmospheric oxygen through time in the model (yellow), constrained by literature estimates for atmospheric oxygen level (gray errorbars denote source's first standard deviation from mean). (a) Oxygen and estimates for the entire model run; (b) Phanerozoic period, which has a higher density of constraints. Arrows indicate maximums (↓) or minimums (↑) for oxygen based on existence mass independent fractionation of sulfur (MIF-S) signal, the duration of which is defined roughly by black bars. Symbols denote sources; ▵ = Canfield et al. (2018) and ✡ = Zhang et al. (2016), constraints from chromium isotopes; ✕ = Krause et al. (2022) estimates from $\delta^{13}C$ fractionation modeling; ▵ = J. E. Johnson et al. (2014) constraints from uraninite and pyrite; ▫ = Izon et al. (2022), ☆ = Luo et al. (2016), and ⋄ = Claire et al. (2014) (and references therein), constraints from mass independent fractionation of sulfur isotopes; ○ = Glasspool and Scott (2010) constraints from charcoal; ◁ = Sperling et al. (2015) constraints from iron speciation; ▷ = Bellefroid et al. (2018) constraints from cerium anomalies (reading Figure 4 data for 90 m chemocline). Black dashed vertical lines denote forced evolutionary transitions: *P* for oxygenic photosynthesis, *F* for fungi, *B* for increased body sizes, and *L* for vascular land plants.

climate oscillation of this magnitude would have had severe consequences for the biosphere, which was also only beginning to cope with abundant oxygen. It is possible that this warming-cooling reversal, coupled with tectonic forcings, could have triggered significant global glaciation (R. E. Kopp et al., 2005).

The two-step oxygenation of the deep ocean caused by evolution of fungi (0.7 Ga) and land plants (0.4 Ga) also corresponds with major climatic cooling events. The temperature maximum prior to fungal evolution is followed by a rapid temperature crash as CH_4 production plummets; this feedback may have contributed to the Neoproterozoic snowball event (Hoffman et al., 1998). Even faster cooling occurs in the wake of vascular plant evolution, this time a perturbation to CO_2 (see Section 3.6.1.6) correlates in time to the end-Devonian mass extinction (Kaiser et al., 2016). Our model does not resolve very short term climate perturbations, punctuated events such as LIP eruptions, or global tectonic arrangements that undoubtably add to the complexity of the geologic oxygen record, particularly for the Phanerozoic portion of the record where more fine-scale oxygen oscillations are resolved.

3.3. Phosphorus Cycle Evolution

Figure 12 highlights the evolving global phosphorus cycle. Figure 13 highlights the C:P ratio of buried OM, a proxy for total phosphorus scavenging.

3.3.1. Phosphorus Cycle: Chronology

3.3.1.1. Stage 1

The early phosphorus cycle is dominated by influxes from continental reservoirs and outfluxes by sorption onto iron oxides. Continental expansion in the Eoarchean by mantle influx results in a silicate-bound phosphorus (SP)

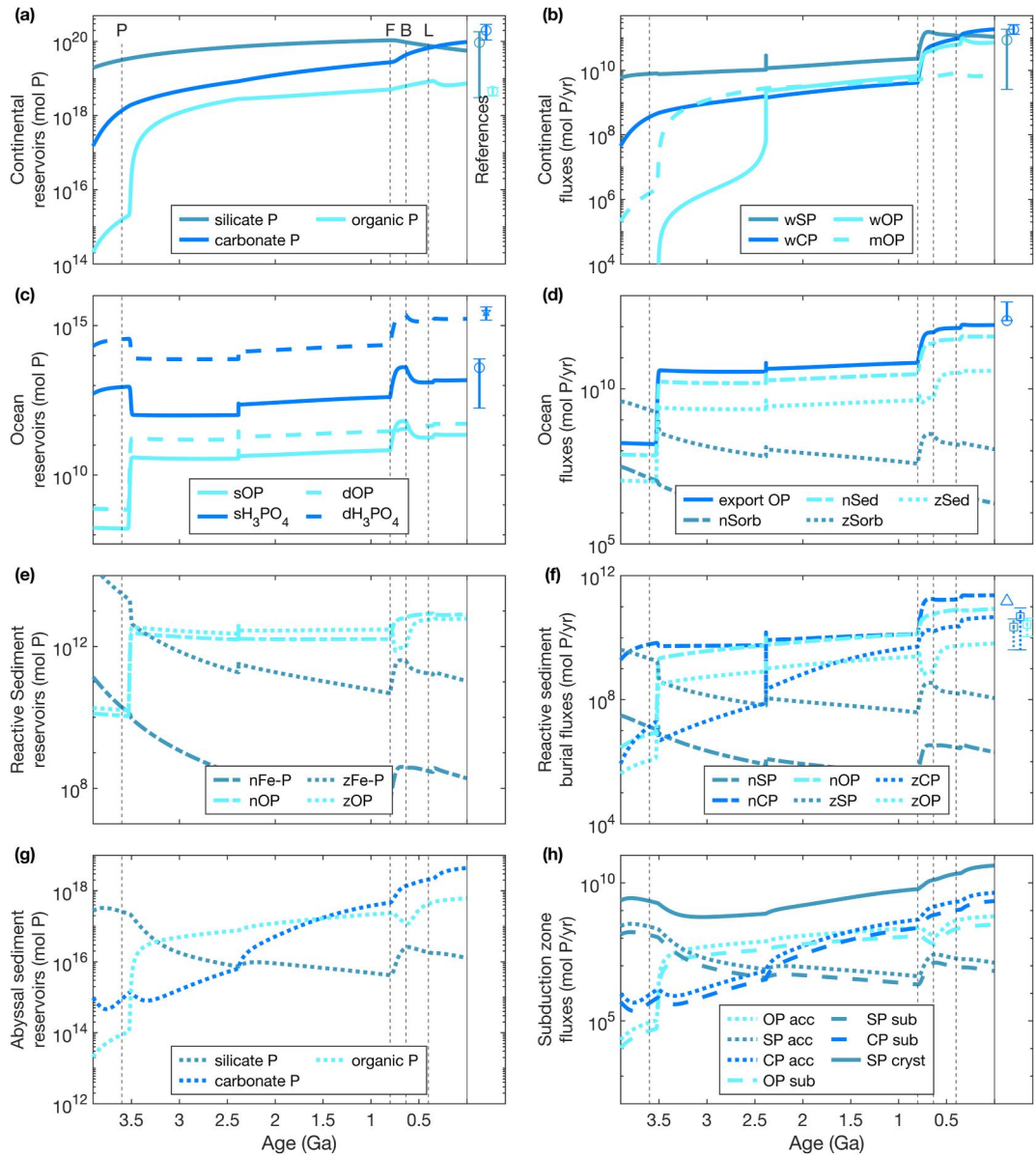

Figure 12. The evolution of phosphorus cycling. Left column (a, c, e, and g) phosphorus geologic reservoirs; in the legends, *u* denotes unreactive pelagic sediments, *o* denotes oceanic crust (slab), and *s*, *n*, *d*, and *z* denote surface ocean, neritic (shelf) sediments, deep ocean, and pelagic sediments, respectively. Right column (b, d, f, and h) phosphorus fluxes for each species out of the reservoirs in the corresponding left subplot (respectively: weathering (*w*) and metamorphism (*m*); export, sorption, and sedimentation; burial; accretion, subduction, and recrystallization). Modern estimates for reservoirs and fluxes are denoted with symbols at the far right of each plot, with range estimates as vertical bars (citations in Table A2); the solid vertical line denotes the end of model output. Black dashed vertical lines denote forced evolutionary transitions: *P* for oxygenic photosynthesis, *F* for fungi, *B* for increased body sizes, and *L* for vascular land plants.

reservoir comparable to modern and significant weathering (Figures 12a and 12b). This influx is only 10% of the total modern P weathering flux, given the absence of terrestrial fungi and plants. The major outfluxes for $[H_3PO_4]$ are sorption onto iron-oxides and burial with apatite in sediments (Figures 12d–12f). Oxide sorption declines until it broadly matches phosphorus influx, allowing dissolved phosphorus to rise to near-modern levels in the surface and deep ocean by the end of this stage (Figures 12c and 12d). Buried organic C:P declines steadily (Figure 13); initially high rates of phosphate scavenging are in response to high phosphorus demand for extensive nitrogen fixation, which limits the biosphere (Figure 7), but scavenging declines steadily as weathering transports more

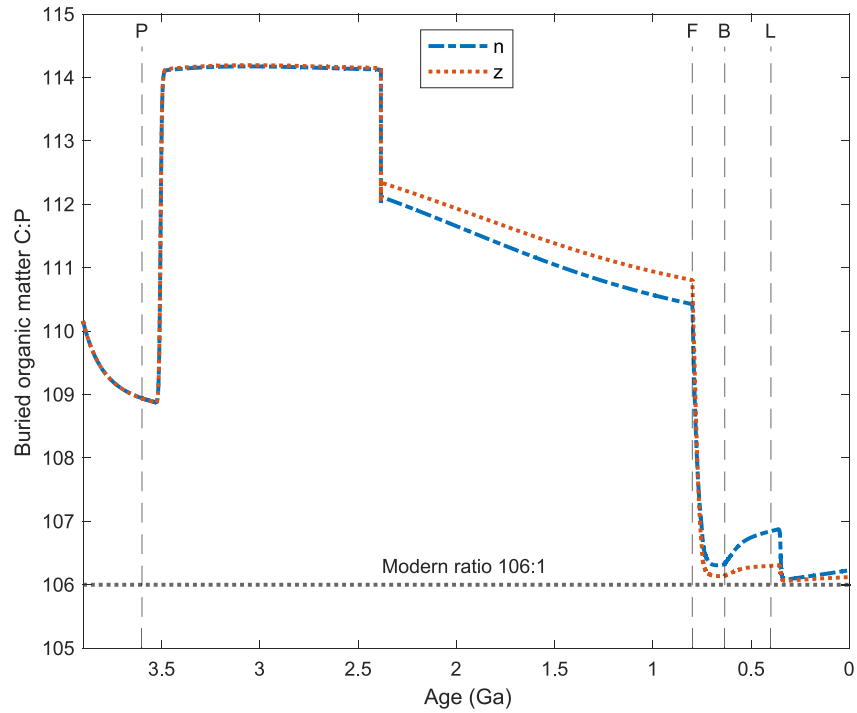

Figure 13. The evolution of buried organic matter (OM) C:P. The ratio of carbon to phosphate in buried OM. Line styles and colors correspond to the different sediment boxes: *n* is neritic (continental shelf) and *z* is pelagic sediments. Increased C:P in buried OM is a function of phosphate scavenging by decomposers in anoxic sediments, and is a function of biosphere P limitation and environmental oxygen level (see Section 2.5.6). Black dashed vertical lines denote forced evolutionary transitions: *P* for oxygenic photosynthesis, *F* for fungi, *B* for increased body sizes, and *L* for vascular land plants. Dotted black horizontal line denotes modern day OM C:P ratio (106:1).

phosphorus to the ocean and P limitation eases. By the end of the stage, total OP export production remains several orders of magnitude lower than modern despite P availability (Figure 12b) as the pre-oxygenic photosynthesis biosphere achieves pseudo-steady state limited by FeO (Section 3.1.1.1).

3.3.1.2. Stage 2

The emergence of oxygenic photosynthesis leads to increased phosphorus demand and biological influence over the phosphorus cycle. Biosphere expansion reduces ocean P reservoirs to a pseudo-steady state minimum at the end of this stage, bolstered by extensive scavenging (Figure 13). Increasing burial spurs rapid growth of the continental OP reservoir (Figure 12a) as phosphorus sequestration shifts from oxide sorption to burial in organics and carbonates (Figures 12d–12f). Sorption fluxes decline for the rest of the model run, mirroring declining iron oxide production by photo-ferrotrophy and increasing ocean pH (Section 3.2.1.2); this flux is limited to lower pH conditions (Section 2.5.7), and the trend in Fe-P reservoirs and sorption fluxes shown in Figures 12d–12f broadly follows ocean pH (Figure 9i). The combination of higher production efficiency, high burial efficiency in anoxic sediments, and low oxidative weathering of sequestered OP (Figures 12b–12f) pushes the system into a new pseudo-steady state with significantly lower dissolved P, severely limiting the oxygenic biosphere until the GOE (Figure 7).

3.3.1.3. Stage 3

The phosphorus cycle is stabilized in the wake of the GOE, possibly because of feedbacks with the nitrogen system. Dissolved levels rebound slightly as oxidative weathering initiates (Figures 12b and 12c), easing both P limitation and scavenging (Figures 7 and 13). Carbonate-bound P burial increases gradually throughout this period following progressive sequestration of atmospheric CO_2 by precipitation (Section 3.2.1.3). The Mesoproterozoic therefore finds a new pseudo-steady state with relatively balanced phosphorus influxes and outfluxes, in response to a biosphere now limited by N (Section 3.1.1.3).

3.3.1.4. Stage 4

The P system is pushed out of pseudo-steady state following the evolution of fungi; this initiates a massive influx of inorganic P to the ocean, which in turn accelerates the biosphere (Figures 12b–12d). Organic phosphorus in sediments again rises, and burial with apatite dominates outfluxes because of feedbacks in the inorganic carbon system (Figures 12e and 12f; discussed in more detail in Section 3.6.1.4). A transient rise in iron-oxide sorption is likely related to the drop in pH coincident with this transition (Section 3.2.1.4). Scavenging drops sharply as oxygen, and thus ammonification, rises in the pelagic sediments (Figures 9a and 13), allowing nitrogen levels to equilibrate and pushing the system into a slightly P-limited regime (Figure 7).

3.3.1.5. Stage 5

The development of large organisms in the Ediacaran decreases dissolved phosphorus to its modern level as remineralization in the water column becomes less efficient (Figure 12c). Faster sinking enhances export production (Figure 12d), causing a slight rise in scavenging as more OM is transported to suboxic sediments (Figure 13). Geological phosphorus reservoirs are increasingly dominated by carbonate-bound P (Figure 12a), a function of increasing carbonate burial and the continuing decline of iron oxide sorption (Figures 12d–12f; Section 3.6.1.5).

3.3.1.6. Stage 6

The final transition phase into the modern phosphorus cycle follows the evolution of the terrestrial biosphere. Inorganic phosphorus weathering increases to its modern level (Figure 12b), pushing the oceanic phosphorus cycle into a new pseudo-steady state, excepting the continuous decline in iron-sorbed phosphorus reservoirs and fluxes. Ratios of C:P in buried organics return to Redfield ratio as the deep ocean oxygenates (Figure 13). The modern geological P cycle is dominated by the balance in carbonate-bound P fluxes (Figures 12a, 12b, and 12f–12h).

3.3.2. Phosphorus Cycle: Tuning Requirements

The balance between phosphorus weathering and burial partially determines whether the GOE occurs. The fraction of P buried with apatite (f_{apatite}) and the effect of fungi on P weathering timescales (χ_{fungi}) are two very important parameters controlling the balance of ocean P availability and thus the entire biological system. A very strong carbonate burial flux ($f_{\text{apatite}} > 0.1$) keeps the biosphere so nutrient limited after the evolution of oxygenic photosynthesis that oxygen production never overwhelms reductant input. If the effect of fungi on phosphorus weathering is weak prior to 3.5 Ga $\left(\chi_{\text{fungi}} < \frac{1}{10}\right)$ then dissolved phosphorus exceeds 10x modern level and the GOE occurs very quickly after photosynthesis evolves; evidence for low Precambrian dissolved phosphorus precludes this scenario (Kipp & Stüeken, 2017).

3.3.3. Phosphorus Cycle: Implications

The climate has been sporadically destabilized by changes in phosphorus availability. During the period between evolution of oxygenic photosynthesis and fungi (3.5–0.7 Ga) there are huge shifts in phosphorus limitation and scavenging (Figures 7 and 13). Surface temperature crashes broadly correlate with the rapid influxes of phosphorus to the ocean that define these shifts (Figures 8c and 12c) by allowing large increases in biosphere productivity (Figure 6b). This has implications on OM burial efficiency through time as well; scavenging allows for phosphorus to be returned more efficiently to the ocean system in times of severe phosphorus limitation, but even so our modeled biosphere experiences periods of productivity very limited by P (Figures 7 and 13). Nitrogen fixation's functional dependence on phosphorus further limits productivity in these conditions. As with high apatite burial, high OM burial in the Archean and Proterozoic oceans would severely restrict P (and hence fixed N) availability and would likely prevent a GOE from occurring, particularly because returning those sequestered nutrients to the ocean requires oxidative weathering, which only initiates after oxygen rises. Because of this, high OM burial efficiency in an anoxic ocean seems incompatible with the timing of the GOE.

3.4. Nitrogen Cycle Evolution

The evolution of the global nitrogen cycle is shown in Figure 14. The division of total nitrogen (and carbon) in the model between the mantle, crust/sediment, and atmosphere-ocean systems through time is shown in Figure 15.

3.4.1. Nitrogen Cycle: Chronology

3.4.1.1. Stage 1

The early nitrogen cycle includes significant sequestration into the continent and mantle. The inorganic and ON cycles are intrinsically linked through nitrogen fixation, the singular pathway by which N_2 can be transferred to the continents and mantle. The nitrogen cycle "ramps up" as nitrogen fixation increases with phosphorus levels (see Section 3.1.1.1). The rapid growth of the continental NH_4^+ reservoir (Figures 14c and 15a) is a testament to massive amounts of fixation and subsequent hydrothermal alteration (Figure 14h). As photo-ferrotrophy assumes pseudo-steady state at the end of this stage (Figure 6b), atmospheric NH_3 and dissolved RN reservoirs follow suit (Figures 14a and 14e); low ocean pH means RN is mainly NH_4^+, and therefore not exchanging with the atmosphere (Figures 14b and 14c); air-sea gas exchange is negative (into the ocean) and not visible throughout this stage, even with extremely high ocean RN levels. Readily available NH_4^+ is hydrothermally altered and accumulates in the oceanic crust, which is then mostly recrystallized onto the continent at subduction zones in a rapid expansion of the continental N reservoir (Figures 14c, 14h, 14i, and 15a). Meanwhile, subduction returns N to the mantle at a significant rate just lower than its mantle outgassing flux (Figure 14j).

3.4.1.2. Stage 2

The evolution of oxygenic photosynthesis and nitrogen fixation increases geologic N at the expense of dissolved reservoirs. Higher productivity following the evolution of oxygenic photosynthesis efficiently sequesters fixed nitrogen into the sediments and continents as OM (Figures 14c, 14f, 14g, and 14i). Hydrothermal sequestration into the oceanic crust declines as dissolved N reservoirs are increasingly taken up by the biosphere (Figures 14e, 14g, and 14h). Nitrate emerges in the ocean as oxygen becomes available for nitrifiers (Figure 14e).

3.4.1.3. Stage 3

The GOE results in a rapid increase in atmospheric ammonia oxidation and oxidative weathering (Figures 14b and 14d). Nitrogen in the ocean is balanced between reduced and oxygenated species (Figure 14e). A massive spike in N_2 exchange to the atmosphere at the GOE corresponds with a significant increase in denitrification (Figures 6d and 14b); this initiates a new period of ocean fixed N levels balanced by denitrification, which heralds the post-GOE period of moderately N limited pseudo-steady state (Figure 7).

3.4.1.4. Stage 4

The evolution of fungi and increasing oxygenation transitions the fixed N reservoir to primarily nitrate. The second jump in environmental oxygen results in further nitrification of the oceanic fixed N reservoir, which gets to a modern level during this stage (Figure 14e). Increasing productivity shifts the major sequestration pathway from hydrothermal alteration of NH_4^+ to the burial of organics (Figures 14h and 14i); this trend is slightly disrupted following the evolution of fungi at 0.7 Ga as remineralization fluxes increase and remove OM from the pelagic sediments more efficiently (Figures 14g and 14h; see Section 3.1.1.3).

3.4.1.5. Stage 5

The evolution of larger organisms reinstates the trend of increasing organic N burial by the end of this stage. Nitrogen influxes to the mantle switch from being dominated by inorganic, silicate-bound N to organic-bound N (Figure 14j). Atmospheric ammonia rises to its highest level following this transition (Figure 14a), corresponding with a turn to positive air-sea gas exchange flux that categorizes the rest of the model run (Figure 14b), partially covered by ammonia oxidation line; even so, this greenhouse gas remains of minor climatic import (Figure 8b). The end of biospheric N limitation coincides with a boost in fixation (Figures 6c and 7), thus ammonia is preferentially released to the atmosphere.

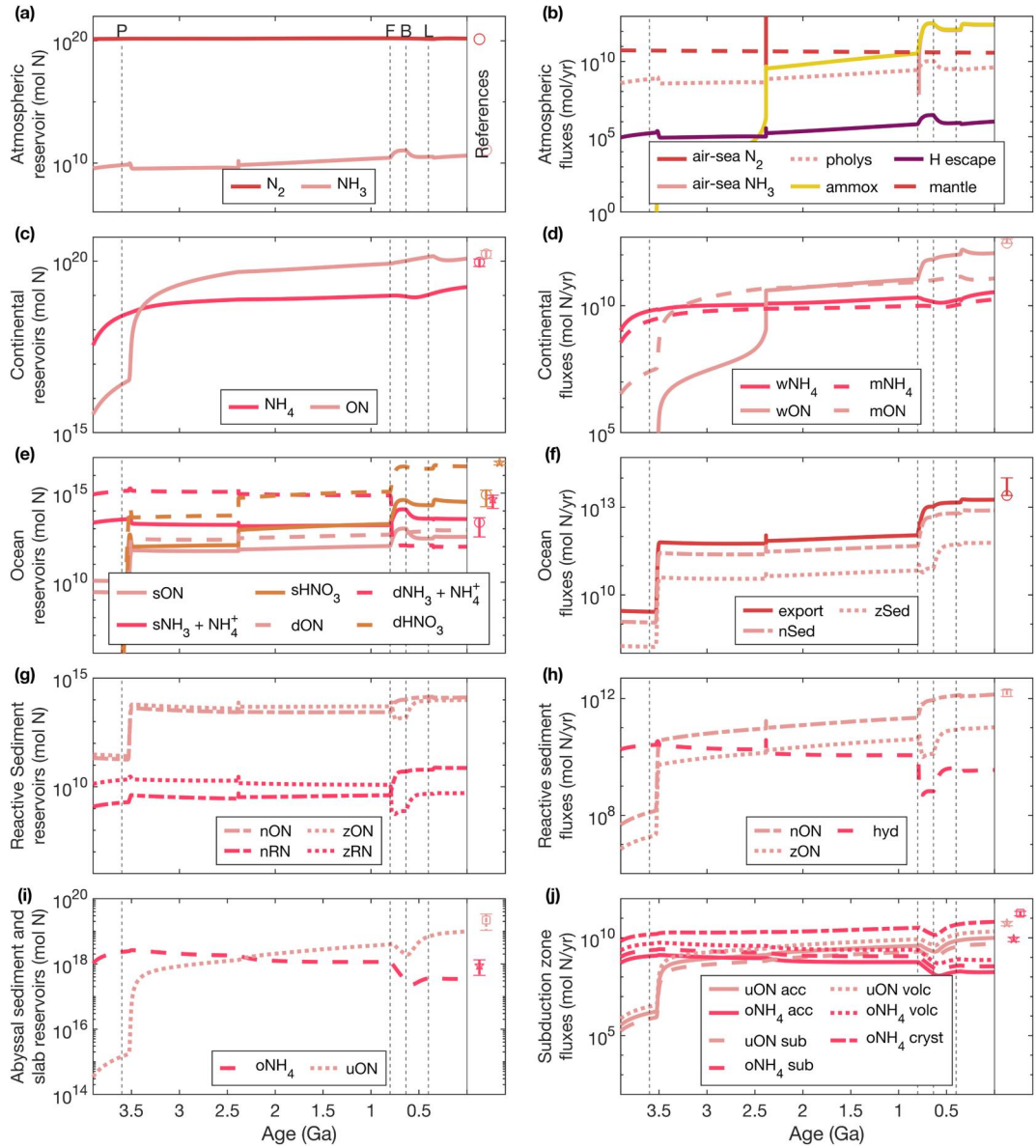

Figure 14. The evolution of nitrogen cycling. Left column (a, c, e, g, and i) nitrogen reservoirs; in the legends, *u* denotes unreactive pelagic sediments, *o* denotes oceanic crust (slab), and *s*, *n*, *d*, and *z* denote surface ocean, neritic (shelf) sediments, deep ocean, and pelagic sediments, respectively. Right column (b, d, f, h, and j) nitrogen fluxes for each species out of the reservoirs in the corresponding left subplot (respectively: air-sea gas exchanges, NH_3 photolysis, hydrogen escape, NH_3 photo-oxidation, and mantle outgassing; weathering (*w*) and metamorphism (*m*); export and sedimentation; burial and hydrothermal alteration; accretion, subduction, volcanism, and recrystallization). Silicate nitrogen is incorporated by hydrothermal alteration into the slab only, while organic nitrogen (NH_3) is buried in sediments from *n* and **z** reactive boxes and is not found in the slab. Modern estimates for reservoirs and fluxes are denoted with symbols at the far right of each plot, with range estimates as vertical bars (citations in Table A2); the solid vertical line denotes the end of model output. Black dashed vertical lines denote forced evolutionary transitions: *P* for oxygenic photosynthesis, *F* for fungi, *B* for increased body sizes, and *L* for vascular land plants.

3.4.1.6. Stage 6

The modern N cycle appears to be in pseudo-steady state. The evolution of the terrestrial biosphere in the Phanerozoic finalizes the nitrification of the fixed N reservoir as the deep ocean and sediments become fully

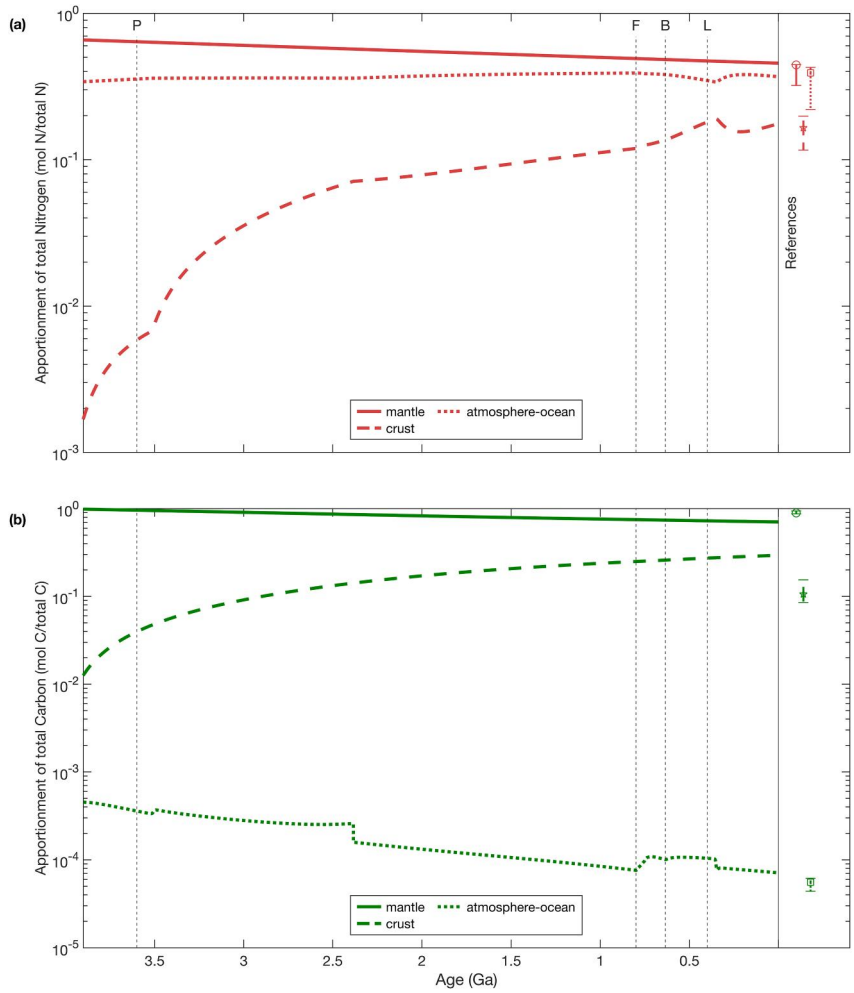

Figure 15. Nitrogen and carbon reservoir apportionment. The portion of total (a) nitrogen and (b) carbon in the model, split between upper mantle, crustal (continent, slab, and abyssal sediments), and atmosphere-ocean reservoirs of all species.

oxygenated (Figures 9a and 9e). Organic N weathering increases transiently across this transition with the oxygen overshoot (Figures 8a and 14d).

3.4.2. Nitrogen Cycle: Tuning Requirements

Because of the dependency of nitrogen fixation on phosphorus availability, the fixed nitrogen cycle is sensitive to phosphorus levels and therefore to the tuning of f_{apatite} (Section 3.3.2). Perhaps the most significant controls on the nitrogen system are the treatment of hydrothermal alteration and the fraction of subduction zone melt that is recrystallized ($f_{\text{cryst,NH4}}$). As our only pathway for inorganic nitrogen sequestration is hydrothermal alteration, the continental silicate-bound N reservoir is quite sensitive to estimates for hydrothermal flow and the seafloor weathering sensitivity modifier (Section 2.6.7). Assuming variable hydrothermal fluid flow would affect the amount of dissolved NH_4^+ passing through the ocean crust, while variable seafloor spreading would affect time spent at the hydrothermal ridge (not treated here); both could therefore change how much dissolved NH_4^+ could be sequestered in the ocean and continental crust through Earth history. We have assumed here that 75% of ocean crust NH_4^+ is recrystallized onto the continent. Higher recrystallization fraction, higher melt fraction, or even faster seafloor spreading (i.e., faster subduction) early in Earth's history would lead to faster accumulation of crustal N and could improve the fit of the model output to modern continental reservoir estimates (Figure 14c). Because of our simplifications to mantle subduction, and because we do not reproduce a mantle thermal history,

the apportionment of nitrogen in the mantle or atmosphere through time is not precisely resolved (Figure 15a); future versions of EONS should expand the current subduction treatment to include dependencies on temperature gradient, pH, and redox to better capture nitrogen subduction and outgassing.

3.4.3. Nitrogen Cycle: Implications

The rise of geologic nitrogen reservoirs is entirely controlled by the biosphere through fixation, highlighted by the correlation between the growth of the silicate-bound N reservoir in continent and dissolved RN in the ocean (Figures 14c and 14e). Biological activity allows for the return of otherwise volatile nitrogen to the mantle, broadly stabilizing the size of the N_2 atmosphere through time (Figure 14a). Solubility and the biosphere's never-ending hunger for fixed nitrogen, absent a significantly higher reduced mantle outflux, effectively inhibit the growth of ammonia in the atmosphere and make a significant radiative contribution from this greenhouse gas extremely unlikely.

Biology is limited by nitrogen availability prior to oxygenic photosynthesis and following the GOE; the most important factor limiting N availability is sequestration (burial) outpacing fixation, and not coupled nitrification-denitrification decreasing fixed N availability. The post-GOE period of N limitation does correspond to increased denitrification and N_2 outgassing to the atmosphere, but also a slow and unabated expansion of the dissolved nitrate and RN reservoirs (Figure 14e). Our nominal run implies that surface nitrogen reservoirs have broadly grown over time, including fixed nitrogen in the ocean (Figure 15a).

3.5. OC Cycle Evolution

The evolution of global OC cycle is shown in Figure 16.

3.5.1. OC Cycle: Chronology

3.5.1.1. Stage 1

Biological activity rapidly expands OC surface reservoirs. Though initialized at modern partial pressures, atmospheric CH_4 rapidly grows to approximately 100 times the modern level via ocean biosphere production outpacing hydrogen escape (Figures 16a and 16b). Photo-ferrotrophy adds a continuous influx of OC to the continent, which ends this stage nearly 3 orders of magnitude smaller than its modern size (Figure 16c).

3.5.1.2. Stage 2

The evolution of oxygenic photosynthesis drives a massive rise in OC production and significantly tempers atmospheric CH_4. The immediate aftermath of oxygenic photosynthesizer evolution is a nearly 100-fold increase in OC production, export, and burial (Figures 16e and 16h) that translates to a rapid growth in geologic reservoirs (Figures 16c and 16i, respectively). Anaerobic remineralization dominates in sediments (Figure 16h), but methane production cannot match rapidly increasing atmospheric oxidation, and CH_4 falls to near-modern levels by the end of this stage (Figures 16a and 16b).

3.5.1.3. Stage 3

The atmospheric methane decline ends with the initiation of the GOE, triggering oxidative weathering and partial oxygenation of the pelagic sediments (Figures 16d and 16h). Methane rebounds after this transition as oxygen levels come to a new steady state with surface reductants, leading to a temperature peak (Figures 8a and 8c). Geologic reservoirs of OC continue growth (Figures 16c, 16e, 16g, and 16i).

3.5.1.4. Stage 4

The OC cycle is disrupted again after the evolution of fungi, leading to a significant and lasting crash in atmospheric methane. The moderate oxygenation pseudo-steady state ends at fungal evolution circa 0.7 Ga; this transition sees the development of near-modern productivity and export that leads to a transient decline in pelagic sediment OC as oxygenation in that reservoir proliferates aerobic remineralization (Figures 16f–16h). The corresponding decline in anaerobic remineralization in the sediments (Figure 16h) is a death knell for atmospheric methane, which is further exacerbated by methane oxidation that increasingly outpaces air-sea gas exchange (Figures 16a and 16b).

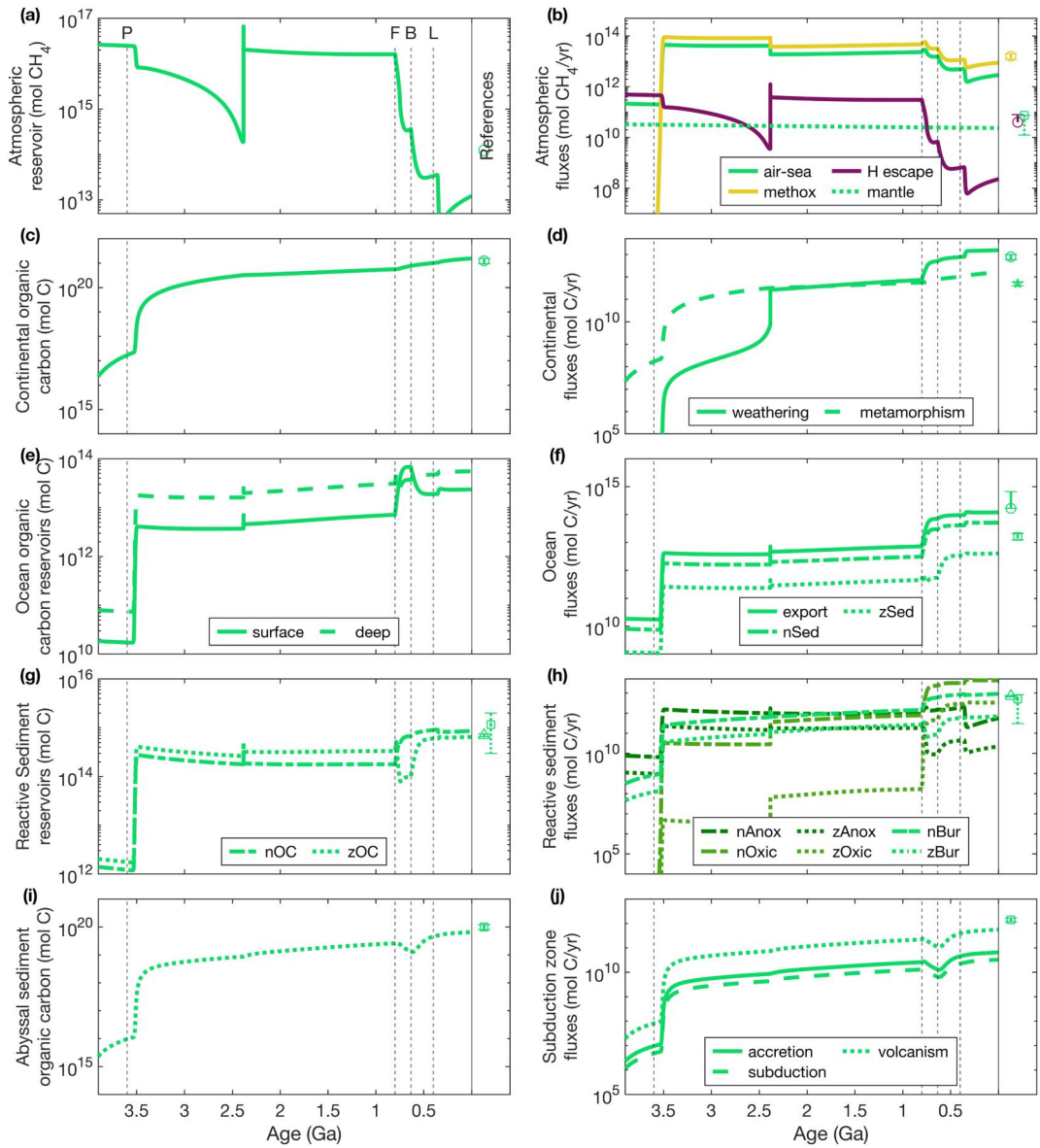

Figure 16. The evolution of organic carbon (OC) cycling. Left column (a, c, e, g, and i) OC reservoirs; in the legends, *u* denotes unreactive pelagic sediments, *o* denotes oceanic crust (slab), and *s*, *n*, *d*, and *z* denote surface ocean, neritic (shelf) sediments, deep ocean, and pelagic sediments, respectively. Right column (b, d, f, h, and j) OC fluxes for each species out of the reservoirs in the corresponding left subplot (respectively: air-sea gas exchange, hydrogen escape, methane oxidation, and mantle outgassing; weathering and metamorphism; export and sedimentation; remineralization (anoxic and oxic) and burial; accretion, subduction, and volcanism). Modern estimates for reservoirs and fluxes are denoted with symbols at the far right of each plot, with range estimates as vertical bars (citations in Table A2); the solid vertical line denotes the end of model output. Black dashed vertical lines denote forced evolutionary transitions: *P* for oxygenic photosynthesis, *F* for fungi, *B* for increased body sizes, and *L* for vascular land plants.

3.5.1.5. Stage 5

The evolution of large bodied organisms in the Ediacaran leads to a secondary crash in atmospheric methane as production declines (Figure 16a); sedimentary anaerobic remineralization, which slightly rebounds here (Figure 16h) is dominated now by denitrification rather than methanogenesis (Figure 6d).

3.5.1.6. Stage 6

The evolution of the terrestrial biosphere solidifies atmospheric CH_4 decline and the full oxygenation of the pelagic sediments. The beginning of the Phanerozoic sees a slight increase in atmospheric methane (Figure 16a) that is quickly quashed by the evolution of land plants and the full development of the terrestrial biosphere. Complete oxygenation of the deep ocean and sediments (Figure 9a) at this point leads to a small rise in aerobic remineralization at the expense of anaerobic remineralization (Figure 16h), further decreasing oceanic methane production (Figure 9b). The rest of the OC cycle reverts to a new pseudo-steady state for the remainder of the eon.

3.5.2. OC Cycle: Tuning Requirements

Continental emergence strongly controls the OC cycle. Reactive sediment burial timescale is evolved through our erosion parameter (χ_{eros}), which in turn affects the relative efficiency of sedimentary remineralization. More extensive remineralization, occurring when burial timescales are longer because of less continental erosion, means less OC is buried and thus net oxygen production is lower. The nominal run is tuned such that the growth of continents via mantle influxes results in modern day surface reservoirs for C, N, P, and SiO_3 at 0 Ga and reactive sediment residence times, using an inverse relationship with relative silicate reservoir size, evolve from approximately 100x modern in the Eoarchean (with 5% continental emergence) to modern day references.

3.5.3. OC Cycle: Implications

Continental OC accumulation occurs in three major steps, and pre and post photosynthesis pulses in growth closely mirror oxygen's rise in the atmosphere (Figure 8a). Husson and Peters (2017) proffered that the punctuated accumulation of OC onto continental bodies was a major cause of the GOE timing and two-step rise, a theory validated by our nominal run which shows three major phases (Figure 16d): (a) slow productivity in the Archean results in slow early accumulation (and low burial efficiency; Figure 6f), (b) growth is thereafter accelerated by a more prolific oxygenic biosphere and stable high burial efficiency (Figure 6f), eventually stabilizing throughout the Mesoproterozoic as oxidative weathering increases following the GOE. (c) A second jump in productivity following fungi evolution and enhanced P influx to the ocean results in the largest absolute growth of continental OC.

Our maximum Archean atmospheric mixing ratio of CH_4 is near 0.01%, much lower than is projected from modeling of xenon escape with hydrogen (Zahnle et al., 2019); this discrepancy could be a result of our limited anoxic biosphere. Were more production pathways included in this model, a slightly more productive biosphere could plausibly be capable of sustaining high pCH_4.

3.6. Inorganic Carbon Cycle Evolution

The evolution of the inorganic carbon cycle is shown in Figure 17.

3.6.1. Inorganic Carbon Cycle: Chronology

3.6.1.1. Stage 1

The Eoarchean atmosphere-ocean inorganic carbon system is moderated by rapid growth of the continental carbonate reservoir. Atmosphere CO_2 level peaks in the first few million years of the Archean as mantle outgassing and eventually air-sea gas exchange equilibrate with DIC (Figures 17a, 17b, and 17e). Minor subaerial silicate weathering and subsequent $CaCO_3$ precipitation in the surface ocean begins sequestering CO_2 from the atmosphere into the sediments and continent (Figures 15b and 17c–17i); extensive inorganic carbon burial in neritic sediments significantly outpaces OC burial (Figures 16h and 17h) and helps maintain low f_{org} throughout this stage (Figure 6e). Seafloor weathering is nearly equal to continental silicate weathering for the first few million years and transfers significant carbon into the oceanic crust (Figures 17h and 17i); this flux declines later as pH rises. Sedimentary and ocean crust $CaCO_3$ is significantly recycled by volcanism, which helps maintain a high partial pressure of CO_2 through the end of this stage (Figure 17j). By that time, so much atmosphere-ocean carbon has been sequestered as $CaCO_3$ that the continental reservoir is within an order of magnitude of its modern size.

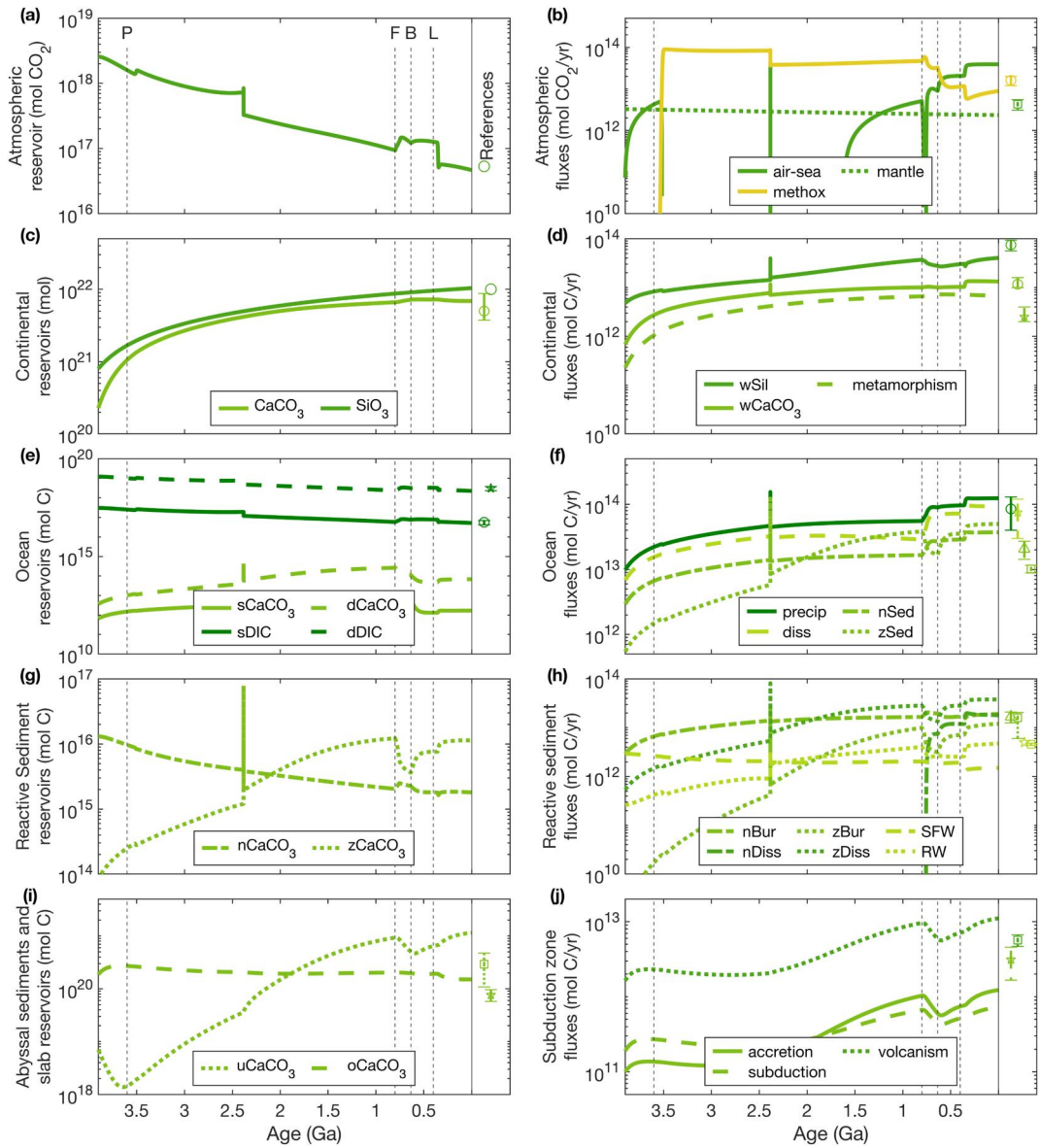

Figure 17. The evolution of inorganic carbon cycling. Left column (a, c, e, g, and i) inorganic carbon (and continental silicate) reservoirs; in the legends, *u* denotes unreactive pelagic sediments, *o* denotes oceanic crust (slab), and *s*, *n*, *d*, and *z* denote surface ocean, neritic (shelf) sediments, deep ocean, and pelagic sediments, respectively. Right column (b, d, f, h, and j) inorganic carbon fluxes for each species out of the reservoirs in the corresponding left subplot (respectively: air-sea gas exchange, mantle outgassing, and methane oxidation; silicate weathering, carbonate weathering and metamorphism; precipitation, dissolution, and sedimentation (export from surface ocean generally equals precipitation); dissolution, seafloor weathering, reverse weathering, and burial; accretion, subduction, and volcanism). Modern estimates for reservoirs and fluxes are denoted with symbols at the far right of each plot, with range estimates as vertical bars (citations in Table A2); the solid vertical line denotes the end of model output. Black dashed vertical lines denote forced evolutionary transitions: *P* for oxygenic photosynthesis, *F* for fungi, *B* for increased body sizes, and *L* for vascular land plants.

3.6.1.2. Stage 2

The inorganic carbon system is relatively stable following the evolution of oxygenic photosynthesis. Photosynthesis and increasing productivity initiates a massive draw of atmospheric CO_2 evidenced by negative air-sea gas exchange through the first part of this stage (Figure 17b). Just before the GOE, atmospheric CO_2 begins to rise in a mirror of methane's decline, a result of increasing production by oxidation (Figures 8a, 17a, and 17b).

Continental weathering continues to rise with growing the silicate reservoir and somewhat stabilizes surface temperature (Figures 8c, 17c, and 17d).

3.6.1.3. Stage 3

The GOE causes a punctuated disruption in the inorganic carbon system. Declining CO_2 is partially compensated by outgassing of ocean DIC (Figures 17a–17c); rising temperature from CH_4 decreases CO_2 solubility and reverses air-sea gas exchange (Figures 8a and 8c). This coincides with a sharp rise in ocean pH and carbonate saturation state, enhancing $CaCO_3$ precipitation (Figures 9i, 9j, and 17f); this boon to the carbonate pump is a likely cause for the transient dip in f_{org} (Figure 6e). The ocean system returns to a pseudo-steady state after this transition, but the atmospheric CO_2 reservoir continues to decline as surface temperature and continental silicate reservoir steadily increase (Figures 8c, 17c, and 17d).

3.6.1.4. Stage 4

The crash in atmospheric methane following fungal evolution causes a massive restructuring of the inorganic carbon cycle. Proterozoic CO_2 trends downward until fungi evolve; this transition initiates a rise in atmospheric O_2 from enhanced productivity, transiently increasing atmospheric oxidation reactions producing CO_2 at the expense of CH_4, which correspondingly declines (Figures 8a, 17a, and 17b). Methane oxidation then crashes as the deep ocean becomes increasingly oxidized and methanogenesis slows (Sections 3.1.1.4 and 3.2.1.4), which is mirrored by a steep rise in DIC and ocean CO_2 outgassing (Figures 17b and 17e) as deep ocean oxygenation accelerates methanotrophy (Figures 9a and 9b). Consequently, pH falls steeply in the deep ocean and sediments, widening the gap between surface and deep ocean saturation states (Figures 9i and 9j). Higher $CaCO_3$ precipitation and export from the surface and lower deep saturation contribute to enhanced dissolution particularly on the shelf (Figures 17f and 17h). This decline in pH is exacerbated by decreasing silicate weathering (Figure 17d), which also bolsters the expansion of atmospheric CO_2; weathering falls in response to temperature, yet another consequence of methane's crash (Figures 8a and 8c). Subduction zone fluxes peak at the start of this transition, and decline with $CaCO_3$ availability in the pelagic and unreactive sediments (Figures 17g and 17j).

3.6.1.5. Stage 5

Enhanced export slows the inorganic carbon cycle perturbation caused by the evolution of fungi. Increasing body sizes cause particulates to sink faster out of the surface and deep ocean, which in turn decreases dissolution in the water column (Figure 17f). Higher $CaCO_3$ export flux boosts sedimentary reservoirs and fluxes out of the subduction zone (Figures 17g, 17i, and 17j). Atmospheric CO_2 returns to its broad pattern of gradual decline as it is sequestered into the continent (Figures 15b, 17a, and 17c).

3.6.1.6. Stage 6

The colonization of continents by vascular plants causes a significant atmospheric CO_2 crash. Continental carbonate and silicate weathering increase in immediate response to plant evolution, immediately drawing down CO_2 (Figures 17a and 17d); while silicate weathering slows as CO_2 falls, carbonate weathering increases with continental carbonates, which is boosted by the rapid influx of alkalinity spurring precipitation and deposition (Figures 17c, 17f, 17h, and 17i). Reverse weathering, which has tracked with sedimentary pH throughout the entire run, increases slightly in response to the alkalinity influx to maintain stable pH (Figures 9i and 17h). In the aftermath of the CO_2 crash, the inorganic carbon system reverts to a new pseudo-steady state with significantly lower atmospheric CO_2; this reservoir continues its slow decline as solar constant increases surface temperature for the duration of the Phanerozoic (Section 3.2.1.6).

3.6.2. Inorganic Carbon Cycle: Tuning Requirements

The inorganic carbon system in this model is sensitive to parameters controlling feedbacks between pH and reverse weathering. Because we do not resolve the global silicate cycle, the choice of fixed $[Si]_0$ in Equation 109 is extremely important. Using the upper estimate for modern porewater dissolved silica yield a very strong feedback between reverse weathering and alkalinity that, while not broadly destabilizing to the inorganic carbon system, forces it into a lower pH steady state and subtly changes the history of atmospheric

CO_2 sequestration. A major change in ocean silica concentration accompanied the evolution of biogenic silica precipitation in the Phanerozoic (Isson & Planavsky, 2018), which is not included as a forcing in this version of EONS; resolving shifting ocean silica levels through time would likely somewhat enhance reverse weathering's influence over the Precambrian climate, particularly in keeping the Proterozoic warm (Krissansen-Totton & Catling, 2020). Precipitation and dissolution timescales are also controlling parameters for this system; we have tuned the model such that total precipitation and dissolution fluxes in the modern ocean correspond to literature estimates. Crustal carbon rises at the expense of mantle and atmosphere-ocean reservoirs, which decline steadily through time (Figure 15b). As such, the amount of carbon outgassing from the mantle strongly determines the stability of the Earth system, particularly in the Archean; a very large upper mantle carbon reservoir, or significantly faster mantle overturn, results in extremely high atmospheric CO_2. Under such conditions and with limited continental emergence, the system enters an extremely acidic state that rapidly becomes unstable.

3.6.3. Inorganic Carbon Cycle: Implications

The climate has been broadly stabilized through geologic time by the long-term sequestration of atmospheric CO_2 into carbonate minerals. Carbon dioxide level and surface temperature essentially reflect one another, with the exception of a positive trend in temperature versus a negative trend in CO_2 (Figures 8c and 17a), both of which are attributable in part to increasing solar constant and the growth of continental silicates (Figures 8d and 17d). Temperature fluctuations, many of which are initiated by increases in biologically sourced atmospheric methane, are perfectly reflected in silicate, carbonate, and seafloor weathering curves (Figures 8c, 17d, and 17h). Our modeled ocean pH agrees well with other models of gradual and monotonic pH increase (Krissansen-Totton et al., 2018; Tajika & Matsui, 1992). We omit the critical ice-albedo feedback, which would add a significant destabilizing force to this story.

A stabilized ancient climate requires extensive carbonate burial, which precludes constant f_{org}. High atmospheric CO_2 in the Eoarchean is required to keep temperatures above freezing (Figures 8a and 8c; Goldblatt & Zahnle, 2011; Walker, 1982), necessitating extensive carbonate burial through the Precambrian as continents grow and solar flux increases (Figures 8d and 17d–17h). Higher f_{org} results from either high OC burial or low inorganic carbon burial; unless the biosphere was significantly more productive in the Archean-Proterozoic periods, in contradiction of conventional wisdom (Canfield et al., 2006; Crockford et al., 2018; Kharecha et al., 2005; Ozaki et al., 2018; Sauterey et al., 2020), modern $f_{org} = 0.2$ at this time would require much lower carbonate burial. Our model suggests that this is highly unlikely and that OC burial increased slowly during these eons, and as a result led to the permanent oxygenation of the Earth's surface (Figures 6e and 10).

4. Discussion and Conclusions

The Earth system is a massively interconnected web of biogeochemical feedbacks. Developing a comprehensive model of this system necessitates consideration of the coupled biogeochemical cycles and climate. This model demonstrates that understanding this planet as it evolved through time implicates systems operating on disparate timescales ranging seconds to billions of years. It further solidifies life's pervasive influence on our planet's evolution.

4.1. A Framework for Model Uncertainty

EONS is a large and complex *conceptual* model of Earth system evolution. It is our best representation of the evolution of Earth, simplified to be conceptually tractable and parametrized to be numerically solvable. We are confident that this produces a very useful tool to aid our understanding of Earth system evolution, through formalizing, quantifying, and testing our assumptions in a self-consistent framework. Yet we are also acutely aware that our model is not gospel: it embodies our assumptions and biases, pragmatic choices, and our fallible understanding of Earth.

Uncertainty in EONS (and any model in this class) can be classed into three types:

1. **Choices and assumptions**: The key science and art of building a conceptual model of Earth are the choices of which reservoirs and processes to include or exclude. These numerous decisions represent our scientific

judgment, tested through iteration and frequently falsified, revised and improved through the development of the model. This set of choices is non-unique, and different choices might well have given results which were either quantitatively or qualitatively different. We see this as the primary source of uncertainty.

An example of a significant choice is that we excluded the sulfur cycle. Knowing that this system strongly affects carbon and oxygen cycles, our choice to exclude had two strands; first the pragmatic necessity of limiting the content in the first version of EONS, and second an assumption that most of the first order features of oxygen and carbon evolution can be broadly explained without sulfur. There are times and places in Earth history when this second assumption will fail, and this version of EONS will give a low fidelity representation of those. A future development of EONS could rectify this; we estimate the cost would be a year or more of model development, with the resulting model possessing another dimension of complexity accompanied by secondary and tertiary uncertainties.

2. **Functional form of parameterizations**: EONS is highly parametrized. In the model biogeochemistry, few of the equations arise from rigorous derivation as would be possible in simpler systems, but rather are approximations of the shape of response to key variables. The form of parametrized responses can have important qualitative impacts on the results, especially where non-linearities are included. To mitigate this, we have used functional forms which are consistent, simple, and smooth wherever possible. Nevertheless, better or different representations of various processes would yield different results. We see this as the major source of secondary uncertainty.
3. **Parameter choice**: Numerous parameters set rates and thresholds in the model, and in many cases these have to be guessed from available experiments or observations, and those guesses iterated upon through examining model output. The nominal run presented uses a set of parameters which works well together, but is undoubtedly non-unique, and we see this as a tertiary source of uncertainty. Mathematical tools exist to automate experimentation with different parameter sets, and these have been used in models of Earth system evolution. However, in our model at least, this would address only the tertiary sources of uncertainty, and therefore would not realistically constrain the overall uncertainty.

Despite all of this uncertainty, we are confident in the utility of our model, and argue that a plausible nominal run of the model is good evidence for most of our assumptions being robust. Numerous of our original assumptions were falsified through our model development, with unrealistic model results making those errors plain. Each revision of a poor assumption (or fixing a bug) generally led to a cascade of simplification and improvement of the results, and EONS as presented is the asymptotic solution of this. Of course, we anticipate that improvements will be made over time, and that EONS as a living model will evolve from this initial release.

4.2. The Origin of Earth's Oxygen

While geologic forcings contribute to its precise timing, surface oxygenation is inevitable in the wake of the evolution of oxygenic photosynthesis. This model successfully produces a reasonable chemical evolution for the Earth's major surface systems. That this finding does not require a robust treatment of the terrestrial biosphere speaks to the overwhelming supremacy of the oceanic carbon pump in controlling the Earth's climate and surface chemistry. Our model agrees with other recent models of the GOE, suggesting that this transition was stepwise (Alcott et al., 2019) and long lived, occurring gradually through the late Archean and Proterozoic, and completing in the early portion of the Phanerozoic with oxygen level reaching its maximum in the Carboniferous (Bergman et al., 2004; Lyons et al., 2014). Our results suggest that while mantle reductant outflux influences the timing of the GOE, a major decline in geologic reductants is not necessary for surface oxidation (Section 3.2.2). Furthermore, our results point to the delay in surface oxygenation after the evolution of oxygenic photosynthesis being exacerbated by gradual buildup of OM sequestering nutrients (Section 3.2.3); while OC burial is a major control allowing oxygen to rise, it is inextricably coupled with sequestration of nutrients, the affect of which is limited biosphere expansion. Explaining oxygen's rise as purely a result of increased OM burial appears insufficient to overcome this feedback. The fraction of carbon buried as organics must have evolved over time or the mantle must have been much more reducing (or outfluxes more than 10x higher) in order for this delay to occur (Section 3.2.3); we believe the former is more realistic.

4.3. Expansion of OC Burial

The growth of f_{org} is a function of export and burial efficiency, both of which have increased as the biosphere expanded, weathering increased and nutrient limitations waned. Carbon isotope evidence and steady state models have suggested that f_{org} is broadly stable through time (Hayes & Waldbauer, 2006; Marais et al., 1992; Schidlowski, 1988), though interpretations of the Precambrian record are diverse. Rothman et al. (2003) modeled carbon isotope evolution in the Neoproterozoic through Phanerozoic and found these records inconsistent with steady state carbon cycling; these authors suggest that OC remineralization became much more efficient at the Cambrian boundary, reducing the size the of ocean OC reservoir and shifting the carbon system to a new steady state that has persisted ever since. A reconstruction of a possible Archean biosphere using more alternative anoxygenic production pathways suggest that the Archean biosphere may have had much lower burial efficiencies (Kharecha et al., 2005). Bjerrum and Canfield (2004) developed a carbon isotope mass balance model for the Precambrian and estimated OC comprised 0%–10% of total carbon buried, not significantly different from our model results. A recent study combining results from carbon isotope modeling and productivity estimates for the Archean suggest that constant $f_{org} = 0.2$ would require burial efficiencies to be impossibly high until 3.5 Ga (Crockford et al., 2023). But it is possible that the carbon record itself is not helpful in constraining f_{org}, given significant uncertainty regarding the magnitude of inorganic carbon cycle fluxes in the Precambrian (Krissansen-Totton et al., 2015), and the high potential for diagenetic alteration (Ahm et al., 2018; Derry, 2010) or authigenic carbonate formation (Schrag et al., 2013) which can alter the carbon isotope record. It has also been suggested that changes in oxidative weathering may alter the isotope record (Daines et al., 2017; Derry, 2014), potentially obfuscating a rise in f_{org} (Krissansen-Totton et al., 2021; Planavsky et al., 2022). Our findings support f_{org} evolving between several pseudo-steady states through Earth's history. Whether or not f_{org} reflects or produces a more oxidized surface is still unresolved; as it is not a fixed parameter in this model, a direct causal relationship to the GOE is impossible to determine. EONS includes all of the systems necessary to track carbon isotopes through time to further bolster this argument, although the addition of such components is beyond the scope of this current work; we hope to more directly address the carbon isotope record in the near future.

Producing the GOE under severely nutrient limited conditions requires lower OM burial efficiency. Decreased continental phosphorus influx, which further limits nitrogen fixation, is a major inhibiting factor for the Precambrian biosphere that must be overcome in order to sustain a biosphere which can eventually cause the GOE (Section 3.1.3). The simplest pathway for nutrient resupply is remineralization under low burial efficiency. We have already discussed why high f_{org} in the Precambrian is unlikely based on the inorganic carbon system (Section 3.6.3). Our model suggests that the delay in oxygenation after the rise of biospheric oxygen production is in part a result of limitation imposed by deficient N and P supply. Higher pre-GOE burial efficiency ($f_{org} > 0.05$) would invariably change the tempo of oxygenation; further exacerbation of nutrient supply could plausibly prevent oxygenation, or the faster accumulation of OC could initiate a GOE even earlier. Fitting this model within geological oxygen constraints (Section 3.2.2) suggests that a billion-year GOE delay requires lower efficiency. Were it the case that oxygenic photosynthesis evolved later than we assume here, higher burial efficiency would be more plausible.

4.4. Biospheric Reworking of Atmosphere, Geosphere, and Climate

Modern oxygen levels are achieved only when the deep ocean becomes fully oxygenated; in this model, that occurs when the terrestrial biosphere fully develops. This finding is consistent with other recent oxygen modeling which found that the evolution of land plants was key in stabilizing atmospheric oxygen (Krause et al., 2022). Model output also indicates rapid oxygenation and climate disruption coincident with biological expansion onto continents in the Neoproterozoic (Sections 3.1.1.6 and 3.2.1.6), supporting a theory that enhanced phosphorus weathering by lichen and fungi contributed to the Neoproterozoic oxygenation event (NOE; Heckman et al., 2001; Lenton & Watson, 2004). Evidence indicates that the deep ocean became mostly oxygenated around the Ediacaran-Cambrian boundary, but that anoxia was still present (Canfield et al., 2007). Our model produces ocean oxygen levels that are broadly consistent with these theories (Section 3.2.1.4). The fact that our atmosphere-ocean does not achieve modern oxygen level without the addition of the terrestrial

biosphere suggests that there were still significant portions of the deep ocean experiencing suboxia into Devonian (Section 3.2.1.5).

The evolutionary trajectory of key geologic cycles is strongly influenced by transitions occurring in the biosphere. This can be most clearly demonstrated by observing the OC continental reservoir growth curve, which is a nearly perfect reflection of the atmospheric O_2 curve, up to the point of the GOE when oxidative weathering begins (Sections 3.2.1.3 and 3.5.1.3). The rise of geologic nitrogen reservoirs and the size of the continental N reservoir broadly correspond to the relative availability of fixed N in the ocean at any given time, and sequestration of biologically fixed N into the ocean crust and subsequent subduction into the mantle maintains surface atmospheric pressure within 20% of the modern level (Section 3.4). Geologic phosphorus shifts from dominantly silicate to carbonate bound species, particularly in the Phanerozoic (Section 3.3.1.5), as biology transitions from producing iron oxides and as increasing OM remineralization efficiency returns H_3PO_4 to sedimentary porewaters where it can be buried as apatite. Key perturbations in the inorganic carbon cycle result from atmospheric methane excursions and crashes exerting control over surface temperatures, activating the silicate weathering feedback (Sections 3.5.1.3 and 3.6.1.3). Every geologic cycle in some way controls the tempo of biological evolution and becomes a product of biological influence.

The climate warms in response to the GOE rather than cools. Our model shows that methanogenesis promotes a rise in atmospheric CH_4 in the aftermath of oxygen's rise which produces rapid climatic warming (Sections 3.1.1.3, 3.2.1.3, and 3.5.1.3). This appears to contradict earlier theories that the permanent oxygenation of the surface would collapse the methane greenhouse and cause dramatic climate cooling (Pavlov et al., 2000). Rather, while the GOE here coincides with rapid warming, it is preceded by a significant decline in CH_4 and cooling. Therefore it is possible that the same processes gave rise to both the GOE and the Paleoproterozoic snowball Earth. We will investigate this in a future version of EONS with a more developed climate system, including ice-albedo feedbacks.

4.5. Earth Outside of Steady State

Climate stabilization by the inorganic carbon cycle has its limitations. While Earth's long-term climate is relatively moderated by the silicate weathering feedback, the overall rising trend in surface temperature broadly reflects external forcings outside of steady state. The inorganic carbon system never achieves even pseudo-steady state between atmosphere-ocean and geologic reservoirs (Section 3.6); while continental reservoirs rapidly grow to near-modern sizes, there is never a point in the model run when carbon reservoir size in any setting (atmosphere, ocean, crustal, or mantle) ceases to change, indicating that sources and sinks of surface carbon are never capable of true equilibration even if they broadly balance on shorter timescales. The continuous rise in solar constant forces a long-term decline in atmosphere-ocean inorganic carbon by influencing the rates of mineral dissolution and continental weathering (Walker et al., 1981). This system is susceptible to extreme perturbations caused by the biosphere, particularly when terrestrial plants emerge and directly influence the silicate weathering feedback; this causes a significant and rapid decline in surface temperature from an all-time high (Section 3.6.1.6), strongly implicating terrestrial plants as the cause of the Devonian mass extinction.

The holistic Earth system is not at steady state. The presence of an active biosphere, coupled with progressive loss of hydrogen to space, means that our planet is becoming increasingly oxidized through time. From this perspective, it is unlikely that the Earth will return to a reducing atmosphere as long as sufficient atmospheric carbon remains available to fuel photosynthesis (Ozaki & Reinhard, 2021). Our model shows that close coupling between biological and geological systematics, which puts expansive geologic cycles in a continuous feedback with short-term biological cycles, prevents planetary steady state. Punctuated pseudo-equilibria arise between major biological transitions as primary production levels equilibrate with geologic influxes, but such distant timescales for system response prevent true stability. Earth's fundamental mutability arises from these inseverable systems; the whole of our planet is infinitely more complex than the sum of its parts.

Appendix A: Model Parameter Conditions

This appendix details key information for the EONS model parameterization: Initial reservoir conditions are provided in Table A1 all model parameters and constants are summarized in Table A3, references for all modern reservoirs and fluxes used in Section 3 nominal run plots are summarized in Table A2, and we include a summary table of all model fluxes with unique chemical stoichiometries in Table A4 (Table A5).

Table A1
Initial Reservoirs Summary

Reservoir	Species	Initial size (mol)	Note	Ref
Atmosphere (a)	CO_2	5×10^{18}	150 PAL	MG1
	CH_4	1.2×10^{14}	1 PAL	
	N_2	1.38×10^{20}	1 PAL	
	NH_3	1.2×10^{11}	10 ppm	SM72
	H_2O	1×10^{18}		
Surface ocean (s)	DIC	2.6×10^{18}	7.5×10^{-2} mol/kg	Tuned
	TA	2.4×10^{18}	7×10^{-2} mol/kg	Tuned
	CH_4	1×10^{6}		
	N_2	3×10^{17}		
	RN	1×10^{14}		
	H_3PO_4	6.1×10^{12}	1.75×10^{-7} mol/kg	B02; F05
	FeO	3.5×10^{15}	1×10^{-4} mol/kg	S20
	H_2O	1×10^{19}		
Neritic sediments (n)	DIC	1.5×10^{14}	7.5×10^{-2} mol/kg	Tuned
	TA	1.4×10^{14}	7×10^{-2} mol/kg	Tuned
	CH_4	1×10^{6}		
	N_2	3×10^{17}		
	RN	1×10^{9}		
	H_3PO_4	3.4×10^{8}	1.75×10^{-7} mol/kg	B02; F05
	H_2O	1×10^{18}		
Deep ocean (d)	DIC	1×10^{20}	7.5×10^{-2} mol/kg	Tuned
	TA	9.8×10^{19}	7×10^{-2} mol/kg	Tuned
	CH_4	1×10^{6}		
	N_2	3×10^{18}		
	RN	1×10^{15}		
	H_3PO_4	2.4×10^{14}	1.75×10^{-7} mol/kg	B02; F05
	FeO	1.4×10^{17}	1×10^{-4} mol/kg	S20
	H_2O	1×10^{20}		
Pelagic sediments (z)	DIC	1.7×10^{15}	7.5×10^{-2} mol/kg	Tuned
	TA	1.6×10^{15}	7×10^{-2} mol/kg	Tuned
	CH_4	1×10^{6}		
	N_2	3×10^{9}		
	RN	1×10^{9}		
	H_3PO_4	4×10^{8}	1.75×10^{-7} mol/kg	B02; F05
	H_2O	1×10^{18}		
Continental crust (c)	SP	1.5×10^{19}	5% PCR	R03; RG03
	Fe_2SiO_4	6.8×10^{20}	5% PCR	W95
	SiO_3	5×10^{20}	5% PCR	RG03
Mantle (m)	C	3.3×10^{22}	100 ppm	TGv2
	N	5.5×10^{20}	2–5 PAN	JG15

Table A1
Continued

Reservoir	Species	Initial size (mol)	Note	Ref
	P	4.6×10^{20}		Tuned
	Fe	2×10^{22}		Tuned
	SiO_3	3×10^{22}		Tuned

Note. All initialized reservoir sizes; we note present atmospheric levels (PAL; PAN denotes present atmospheres of nitrogen) and sources for certain values in the **Notes** column. Citation keys are: **G21** (Goldblatt et al., 2021); **SC72** (Sagan & Chyba, 1997); **B02** (Bjerrum & Canfield, 2002); **F05** (Fennel et al., 2005); **S20** (Swanner et al., 2020); **R03** (Ruttenberg, 2003); **RG03** (Rudnick & Gao, 2003); **W95** (Wedepohl, 1995); **TGv2** (Carlson, 2005); **JG15** (B. Johnson & Goldblatt, 2015); Tuned denotes initial conditions set to equilibrate high initial atmospheric CO_2 (for DIC, TA) or to achieve modern surface reservoirs at the end of the run, given a constant mantle outflux (for mantle reservoirs). "PAL" stands for present atmospheric level; "PCR" stands for present continental reservoir size; "PAN" stands for present atmospheric nitrogen level.

Table A2
Modern References

Subplot	Item	Symbol	Reference
Figure 6			
a	Fixed N	∘	Koltermann et al. (2011) and Talley (2007)
	HNO_3	∘	Koltermann et al. (2011) and Talley (2007)
	NH_3+NH_4^+	∘	Gruber (2008)
	H_3PO_4	∘	Koltermann et al. (2011) and Talley (2007)
b	Oxygenic photosynthesis	∘	Canuel and Hardison (2018)
	Photoferrotrophy	∘	Thompson et al. (2019)
c	Oxygenic fixation	∘	Palta and Hartnett (2018)
d	Ammonification	∘	Canuel and Hardison (2018)
	Denitrification	∘	Gruber (2008)
e	Organic carbon burial fraction	∘	Berner (2004)
f	Burial efficiency	∘	Crockford et al. (2023)
Figure 8			
a	CO_2	∘	Falkowski (2012)
	CH_4	∘	Ciais et al. (2014)
	N_2	∘	Wallmann and Aloisi (2012)
	NH_3	∘	Byrne and Goldblatt (2014)
	O_2	∘	Bergman et al. (2004)
b	CO_2	∘	Byrne and Goldblatt (2014)
	CH_4	∘	Byrne and Goldblatt (2014)
	NH_3	∘	Byrne and Goldblatt (2014)
c	Surface temperature	∘	Lodders et al. (1998)
d	Solar constant	∘	G. Kopp and Lean (2011)
Figure 9			
a	$[O_2]_s$	∘	Koltermann et al. (2011) and Talley (2007)
	$[O_2]_d$	☆	Koltermann et al. (2011) and Talley (2007)
c	$[RN]_s$	∘	Gruber (2008)
	$[RN]_d$	☆	Gruber (2008)
d	$[HNO_3]_s$	∘	Koltermann et al. (2011) and Talley (2007)
	$[HNO_3]_d$	☆	Koltermann et al. (2011) and Talley (2007)
e	$[H_3PO_4]_s$	∘	Koltermann et al. (2011) and Talley (2007)
	$[H_3PO_4]_d$	☆	Koltermann et al. (2011) and Talley (2007)

Table A2
Continued

Subplot	Item	Symbol	Reference
f	$[OrgC]_n$	△	Mackenzie et al. (2004)
	$[OrgC]_z$	□	Mackenzie et al. (2004)
g	$[DIC]_s$	○	Falkowski (2012)
	$[DIC]_d$	☆	Falkowski (2012)
h	$[TA]_s$	○	Millero (1996)
	$[TA]_d$	☆	Millero (1996)
i	pH_s	○	Zeebe and Wolf-Gladrow (2001)
Figure 12			
a	Silicate P	○	Jahnke (2000)
	Carbonate P	○	Jahnke (2000)
	Organic P	○	Falkowski (2012)
b	wSP	○	Jahnke (2000)
	wCP	○	Jahnke (2000)
c	$[HNO_3]_s$	○	Koltermann et al. (2011) and Talley (2007)
	$[HNO_3]_d$	☆	Koltermann et al. (2011) and Talley (2007)
d	Export OP	○	Watson and Orr (2003)
f	zSP	□	Ruttenberg (2003)
	nCP	△	Ruttenberg (2003)
	zCP	□	Ruttenberg (2003)
	zOP	□	Mackenzie et al. (2004)
Figure 14			
a	N_2	○	Wallmann and Aloisi (2012)
	NH_3	○	Byrne and Goldblatt (2014)
c	NH_4	○	Wallmann and Aloisi (2012)
	ON	○	Falkowski (2012)
d	wON	○	Voss et al. (2013)
e	$sHNO_3$	○	Koltermann et al. (2011) and Talley (2007)
	$dHNO_3$	☆	Koltermann et al. (2011) and Talley (2007)
	sNH_3-NH_4^+	○	Gruber (2008)
	dNH_3-NH_4^+	☆	Gruber (2008)
f	export ON	○	Watson and Orr (2003)
h	nON	○	Mackenzie et al. (2004)
i	oNH_4	☆	Goldblatt et al. (2009)
	uON	□	Goldblatt et al. (2009)
j	volc oNH_4	□	Wallmann and Aloisi (2012)
	sub oNH_4	☆	Goldblatt et al. (2009)
	volc uON	□	Wong et al. (2019)
	sub uON	☆	Goldblatt et al. (2009)
Figure 15			
a	Mantle N	○	Goldblatt et al. (2009)
	Crust N	☆	Goldblatt et al. (2009) and B. Johnson and Goldblatt (2015)
	Atmosphere-ocean N	□	Byrne and Goldblatt (2014) and Gruber (2008)
b	Mantle C	○	Kelemen and Manning (2015)
	Crust C	☆	Falkowski (2012) and Wallmann and Aloisi (2012)
	Atmosphere-ocean C	□	Ciais et al. (2014) and Falkowski (2012)

Table A2
Continued

Subplot	Item	Symbol	Reference
Figure 16			
a	CH_4	○	Ciais et al. (2014)
b	Methox	○	Ciais et al. (2014)
	Mantle	□	Bergman et al. (2004)
	H escape	○	Catling et al. (2001)
c	Continental OC	○	Wallmann and Aloisi (2012)
d	Weathering	○	Bergman et al. (2004)
	Metamorphism	☆	Wallmann and Aloisi (2012)
f	Export	○	Watson and Orr (2003)
	zSed	□	Watson and Orr (2003)
g	nOC	△	Mackenzie et al. (2004)
	zOC	□	Mackenzie et al. (2004)
h	nBur	△	Mackenzie et al. (2004)
	zBur	□	Mackenzie et al. (2004)
	nOxic	△	Mackenzie et al. (2004)
	zOxic	□	Mackenzie et al. (2004)
i	Abyssal sediment OC	□	Clift (2017)
j	Volcanism	□	Wong et al. (2019)
Figure 17			
a	CO_2	○	Falkowski (2012)
b	Methox	○	Ciais et al. (2014)
	Mantle	□	Wallmann and Aloisi (2012)
c	$CaCO_3$	○	Falkowski (2012)
	SiO_3	○	Rudnick and Gao (2003)
d	wSil	○	Canuel and Hardison (2018)
	$wCaCO_3$	○	Wallmann and Aloisi (2012)
	Metamorphism	☆	Wallmann and Aloisi (2012)
e	sDIC	○	Falkowski (2012)
	dDIC	☆	Falkowski (2012)
f	precip	○	Wallmann and Aloisi (2012)
	diss	☆	Wallmann and Aloisi (2012)
	nSed	△	Libes (2011)
	zSed	□	Mackenzie et al. (2004)
h	nBur	△	Libes (2011)
	zBur	□	Mackenzie et al. (2004)
	SFW	☆	Wallmann et al. (2008)
	RW	□	Li and Elderfield (2013)
i	$uCaCO_3$	□	Wong et al. (2019)
	$oCaCO_3$	☆	Mackenzie et al. (2004)
j	Volcanism	□	Wong et al. (2019)
	Subduction	☆	Wong et al. (2019)

Note. All references correspond to nominal run output plots in Section 3, denoting the plot symbols for each point. Subplots without denoted references are excluded.

Table A3
Model Constants and Parameters

Parameter and definition	Value	Units	Ref
Atmosphere Constants			
Solar radiation constants			
S_M	1,361	W/m^2	BG14
S_A	1,020	W/m^2	This model
Average hydrogen diffusion constant			
k_{Hesc}	1.33×10^{16}	mol H/yr	C06
Thermal optical depth parameterization constants ($a_T T + b_T G F_t$)			
a_T	0.0075		This model
b_T	0.0175		This model
N_2 pressure-broadening exponent			
q	0.1257		This model
van't Hoff Temperature dependant Henry's law constants $(-\Delta_{sol}H)/R$			
ν_{O2}	1,700	K	S15
ν_{CO2}	2,400	K	S15
ν_{CH4}	1,900	K	S15
ν_{N2}	1,300	K	S15
ν_{NH3}	4,200	K	S15
Henry's Law constants at 298.15 K			
κ_{0,O_2}	1.2×10^{-5}	mol/m^{3}Pa	S15
κ_{0,CO_2}	3.3×10^{-4}	mol/m^{3}Pa	S15
κ_{0,CH_4}	1.4×10^{-5}	mol/m^{3}Pa	S15
κ_{0,N_2}	6.4×10^{-6}	mol/m^{3}Pa	S15
κ_{0,NH_3}	5.9×10^{-1}	mol/m^{3}Pa	S15
Gas diffusivity			
D_{O_2}	1.78×10^{-5}	cm/s	CRC
D_{CO_2}	1.45×10^{-5}	cm/s	CRC
D_{CH_4}	1.55×10^{-5}	cm/s	CRC
D_{N_2}	2.0×10^{-5}	cm/s	CRC
D_{NH_3}	1.5×10^{-5}	cm/s	CRC
Modern atmospheric reservoirs			
$R_{O2,a,0}$	3.7×10^{19}	mol	JG18
$R_{CO2,a,0}$	5.3×10^{16}	mol	JG18
$R_{N2,a,0}$	1.4×10^{20}	mol	JG18
$R_{CH4,a,0}$	1.2×10^{14}	mol	JG18
$R_{NH3,a,0}$	1.7×10^{12}	mol	JG18
Earth properties			
Mean albedo			
α	0.3		
Surface area of the Earth, ocean, continents, and continental sediments			
A_E	5.1×10^{14}	m^2	JG18
A_{oc}	3.4×10^{14}	m^2	JG18
A_{cont}	1.7×10^{14}	m^2	JG18
A_{shelf}	3.4×10^{12}	m^2	This model

Table A3
Continued

Parameter and definition	Value	Units	Ref
Ocean, continental crust, oceanic crust, and upper mantle mass			
M_{oc}	1.4×10^{21}	kg	
M_{ccrust}	1.52×10^{22}	kg	LF98
M_{ocrust}	8.45×10^{21}	kg	LF98
M_{um}	1×10^{24}	kg	LF98
Continental topographic relief growth rate			
η_{topo}	$\frac{3}{2}$		This model
Specific heat capacity and density of ocean water			
c_p	4,200	J/kgK	
ρ_{oc}	1,027	kg/m^3	
Depth of ocean boxes and stagnant boundary layer			
d_s	100	m	JG18
d_d	4,000	m	JG18
d_{sl}	3.96×10^{-5}	m	LS74
Modern ocean dissolved silica			
$[Si]_0$	5×10^{-3}	mol/m^3	IP18, This model
Modern ocean dissolved phosphorus			
$[H_3PO_4]_0$	1.5×10^{-3}	mol/L	WOCE
Continental silicate reservoir			
$R_{sil,c,0}$	1×10^{22}	mol	This model
Fractions			
f_{Ashelf}	0.08		YF01
f_{Pshelf}	0.3		YF01
f_{sub}	0.05		This model
f_{melt}	0.85		This model
f_{acc}	0.1		This model
$f_{apatite}$	0.01		This model
f_{scav}	0.1		This model
f_{melt}	0.85		This model
$f_{acc,u}$	0.1		This model
$f_{acc,o}$	0.05		This model
$f_{sub,u}$	0.05		This model
$f_{sub,o}$	0.1		This model
$f_{volc,NH4}$	0.2125		This model
$f_{volc,ON}$	0.2125		This model
$f_{volc,\ CaCO3}$	0.85		This model
$f_{volc,OC}$	0.85		This model
$f_{cryst,NH4}$	0.6375		This model
$f_{cryst,ON}$	0.6375		This model
$f_{cryst,SP}$	0.85		This model
$f_{cryst,OP}$	0.85		This model
$f_{cryst,CP}$	0.85		This model
$f_{cryst,Fe(OH3)}$	0.85		This model

Table A3
Continued

Parameter and definition	Value	Units	Ref
Population growth curve slopes			
ϵ_{photo}	2.76×10^{-7}	yr^{-1}	This model
ϵ_{fungi}	4.61×10^{-8}	yr^{-1}	This model
ϵ_{plant}	5.53×10^{-7}	yr^{-1}	This model
Biological Reaction constants $k_{j,x}$			
Half-saturation uptake of O_2 in ammonification			
$k_{ammon,O2}$	8×10^{-3}	mol/m^3	CRC
Nitrification acidity inhibition factor			
$k_{nit,H}$	6.3×10^{-5}	mol/m^3	DK00
Nitrification half-saturation uptake values			
$k_{nit,O2}$	2×10^{-2}	mol/m^3	F05
Denitrification half-saturation uptake values			
$k_{denit,HNO3}$	4.4×10^{-3}	mol/m^3	DK00
$k_{denit,O2}$	2.05×10^{-4}	mol/m^3	T14
Nutrient assimilation half-saturation uptake values			
$k_{assim,\ fixN}$	1.6×10^{-3}	mol/m^3	JG18
$k_{assim,H3PO4}$	10^{-4}	mol/m^3	JG18
$k_{assim,DIC}$	4.4×10^{-3}	mol/m^3	B01
Redfield sensitivity half-saturation constant			
$k_{assim,NP}$	2		This model
Half reaction rate for N_2 fixation			
$k_{fix,N2}$	3.73×10^{-2}	mol/m^3	JG18
Methanotrophy half-saturation uptake values			
$k_{mtrophy,O2}$	5.7×10^{-3}	mol/m^3	R97
Oxygen limitation on anoxicity			
$k_{anox,O2}$	6.2×10^{-3}	mol/m^3	C08
pH limitation on iron-phosphate sorption			
$k_{sorb,pH}$	7		K07
Biological Uptake ratios $r_{\frac{j}{j^*}}$			
Nutrient assimilation			
$r_{\frac{C}{P}}$	106:1		
$r_{\frac{C}{N}}$	106:16		
$r_{\frac{N}{P}}$	16:1		
Newly Fixed N Assimilation			
$r_{\frac{N2}{newN}}$	1:2		
$r_{\frac{CO2}{newN}}$	106:16		
$r_{\frac{H3PO4}{newN}}$	1:16		
$r_{\frac{O2}{newN}}$	118:16		
$r_{\frac{H2O}{newN}}$	130:16		
$r_{\frac{N2}{FeO}}$	8:472		
$r_{\frac{CO2}{FeO}}$	106:472		
$r_{\frac{H3PO4}{FeO}}$	1:472		
$r_{\frac{H2O}{FeO}}$	838:472		

Table A3
Continued

Parameter and definition	Value	Units	Ref
Geochemical constants			
Activation energies for weathering dissolution			
E_{gran}	20.5	kcal/mol	BC94
E_{basa}	15	kcal/mol	BC94
E_{carb}	32	kJ/mol	H85
Rate power for $CaCO_3$ reactions			
η_{calc}	1.25		This model
η_{diss}	1.05		This model
Rate power for weathering reactions			
η_w	0.3		SZ01
Normalization modifiers for weathering sensitivity			
a_w	10		This model
b_w	9		This model
Speciation constant for orthophosphate			
k_{ads}	0.07	μM^{-1}	B02
Rate constant of reverse weathering			
k_{rw}	5.75×10^{12}	mol C/yr	IP18
Rate constant of seafloor weathering			
k_{sfw}	1.75×10^{12}	mol C/yr	GC11, M14
Rate constant of hydrothermal flow			
k_{hyd}	5.05×10^{13}	m^3/yr	JG17
Sediment diffusion constants			
λ_{N2}	6.28×10^{-2}	m^2/yr	B96
λ_{NO3}	1.58×10^{-2}	m^2/yr	B92
λ_{NH4}	2.21×10^{-2}	m^2/yr	B92
λ_{PO4}	9.5×10^{-3}	m^2/yr	B92
λ_{O2}	3.15×10^{-2}	m^2/yr	KB80
λ_{CO2}	4.57×10^{-2}	m^2/yr	CRC
λ_{HCO3}	1.61×10^{-2}	m^2/yr	T95
λ_{CH4}	2.74×10^{-2}	m^2/yr	IJ93
Timescales			
NH_3 photo-oxidation and photolysis			
$\tau_{ammox,0}$	5	day	BG14
τ_{pholys}	10	yr	K82
Fe(II) Photo-oxidation			
τ_{photox}	1	yr	This model
Productivity			
τ_{assim}	180	day	F05
τ_{fix}	1,825	day	F05
τ_{death}	15	day	AR5

Table A3
Continued

Parameter and definition	Value	Units	Ref
Ocean mixing, sinking, and sediment residence			
τ_{oc}	1,000	yr	KO08
$\tau_{sink,s}$	50	day	KO08
$\tau_{sink,d}$	5,000	day	FK09
$\tau_{sink,n}$	100	yr	This model
$\tau_{sink,z}$	1,000	yr	This model
Aerobic remineralization			
$\tau_{oxrm,s}$	1.65	day	KO08, This model
$\tau_{oxrm,d}$	165	day	KO08, This model
$\tau_{oxrm,n}$	30	yr	KO08, This model
$\tau_{oxrm,z}$	300	yr	KO08, This model
Anaerobic remineralization and methanotrophy			
$\tau_{axrm,s}$	165	day	This model
$\tau_{axrm,d}$	825	day	This model
$\tau_{axrm,n}$	10	yr	This model
$\tau_{axrm,z}$	150	yr	This model
$\tau_{mtrophy}$	0.1	yr	This model
Nitrification			
τ_{nit}	2.4×10^{-2}	yr	DK00, This model
Carbonate Precipitation and Dissolution			
τ_{precip}	25	yr	This model
$\tau_{diss,s}$	0.25	yr	This model
$\tau_{diss,d}$	0.25	yr	This model
$\tau_{diss,n}$	10	yr	This model
$\tau_{diss,z}$	100	yr	This model
Iron oxide P sorption and reduction			
τ_{sorb}	0.1	yr	J10
Weathering			
τ_{wsil}	5×10^{8}	yr	Z12
τ_{woxi}	1×10^{8}	yr	B04
τ_{wcarb}	5×10^{8}	yr	Z12, WA12
Outgassing and subduction			
τ_{meta}	10^{9}	yr	WA12
τ_{subd}	10^{8}	yr	This model

Note. Reference abbreviations are **JG18** (B. W. Johnson & Goldblatt, 2018), **S15** (Sander, 2015), **CRC** (Haynes, 2014), **Ar5** (Ciais et al., 2014), **Z12** (Zeebe, 2012), **SZ01** (Sleep & Zahnle, 2001), **B02** (Bjerrum & Canfield, 2002), **B04** (Bergman et al., 2004), **YF01** (Yool & Fasham, 2001), **BG14** (Byrne & Goldblatt, 2014), B01 (Burkhardt et al., 2001), **F05** (Fennel et al., 2005), **K07** (Konhauser, Amskold, et al., 2007), **WA12** (Wallmann & Aloisi, 2012), **IP18** (Isson & Planavsky, 2018), **T14** (Tiano et al., 2014), **FK09** (Fischer & Karakaş, 2009), **BC94** (Brady & Carroll, 1994), **H85** (Herman & White, 1985), **C06** (Claire et al., 2006), **C08** (Crowe et al., 2008), **KO08** (Kriest & Oschlies, 2008), **R97** (Ren et al., 1997), **B92** (Butcher et al., 1992), **B96** (Boudreau, 1996), **T95** (Treumann et al., 1995), **LJ93** (Iversen & Jørgensen, 1993), **KB80** (Krom & Berner, 1980), **GC11** (Gillis & Coogan, 2011), **M14** (Mills et al., 2014), **LF98** (Lodders et al., 1998), **LS74** (Liss, 1974), **DK00** (Dinçer & Kargı, 2000), **WOCE** (Talley, 2007), and **J10** (Jaisi et al., 2010). References accompanied by "This model" denote parameters derived from literature sources but modified in the tuning process.

Geochemistry, Geophysics, Geosystems

10.1029/2023GC011252

Table A4
Model Flux Summary

Flux name	Equation number	Stoichiometry	Parameterization	Reservoirs								
				a	*s*	*n*	*d*	*z*	*u*	*o*	*c*	*m*
Photochemical Fluxes												
NH_3 Photolysis	Equation 52	$8NH_3 + 3CO_2 \xrightarrow{12h\nu} 4N_2 + 3CH_4 + 6H_2O$	$F_{\text{pholys}} = \frac{R_{\text{NH3,a}}}{\tau_{\text{pholys}}}$	✓								
NH_3 Photo-oxidation	Equation 49	$2NH_3 + \frac{3}{2}O_2 \xrightarrow{6h\nu} N_2 + 3H_2O$	$F_{\text{ammox}} = \frac{R_{\text{NH3,a}}}{\tau_{\text{ammox}}(O_2)}$	✓								
CH_4 Photo-oxidation	Equation 54	$CH_4 + 2O_2 \xrightarrow{4h\nu} CO_2 + 2H_2O$	$F_{\text{methox}} = K_{\text{eff}}([CH_4][O_2])^{\frac{1}{2}}$	✓								
NH_3 Hydrogen escape	Equation 58	$2NH_3 \xrightarrow{6h\nu} N_2 + 6H^+\uparrow$	$F_{\text{Hesc},NH3} = k_{\text{Hesc}}[NH_3]\frac{1}{3}$	✓								
CH_4 Hydrogen escape	Equation 58	$CH_4 + H_2O \xrightarrow{4h\nu} \frac{1}{2}CO_2 + \frac{1}{2}CH_4 + 4H^+\uparrow$	$F_{\text{Hesc,CH4}} = k_{\text{Hesc}}[CH_4]\frac{1}{4}$	✓								
Biochemical Fluxes												
$CaCO_3$ Precipitation	Equation 61	$Ca^{2+} + 2HCO_3^- \xrightarrow{\Omega \geq 1} CaCO_3 + CO_2 + H_2O$	$F_{\text{precip},i} = \frac{(\Omega_i - 1)^{\eta_{\text{calc}}}[CO_3^{2-}]_i M_{\text{oc},i}}{\tau_{\text{precip}}}$		✓	✓	✓	✓				
$CaCO_3$ Dissolution	Equation 62	$CaCO_3 + CO_2 + H_2O \xrightarrow{\Omega < 1} Ca^{2+} + 2HCO_3^-$	$F_{\text{diss},i} = \frac{(1-\Omega_i)^{\eta_{\text{diss}}} R_{\text{CaCO3},i}}{\tau_{\text{diss}}}$		✓	✓	✓	✓				
Nitrification	Equation 37	$NH_4^+ + 2O_2 \rightarrow HNO_3 + H^+ + H_2O$	$F_{\text{nit},i} = \frac{[NH_4^+]M_{\text{oc},i}}{\tau_{\text{nit}}} L_{\text{nit,O}_2,i}(1 - L_{\text{nit,H},i})$		✓	✓	✓	✓				
Abiotic Iron photo-oxidation	Equation 65	$4FeO + O_2 + 11H_2O \xrightarrow{4h\nu}$	$F_{\text{Fephotox}} = \frac{R_{\text{FeO,s}}}{\tau_{\text{photox}}} L_{\text{O}_2,\text{anox},s}$		✓							
Productivity by photosynthesis via NH_3 assimilation	Equation 26	$106CO_2 + 16NH_3 + H_3PO_4 + 106H_2O \xrightarrow{h\nu} (CH_2O)_{106}(NH_3)_{16}(H_3PO_4) + 106O_2$	$F_{\text{assim,NH3}} = \frac{R_{H_3PO_4,s}}{\tau_{\text{assim}}} L_{\text{assim,DIC}} L_{\text{Redf}} r_P^C \chi_{\text{photo}}(t) f_{\text{RN}}$		✓							
Productivity by photosynthesis via HNO_3 Assimilation	Equation 26	$106CO_2 + 16HNO_3 + H_3PO_4 + 122H_2O \xrightarrow{h\nu} (CH_2O)_{106}(NH_3)_{16}(H_3PO_4) + 138O_2$	$F_{\text{assim,HNO3}} = \frac{R_{H_3PO_4,s}}{\tau_{\text{assim}}} L_{\text{assim,DIC}} L_{\text{Redf}} r_P^C \chi_{\text{photo}}(t)(1 - f_{\text{RN}})$		✓							
Productivity by Oxygenic N_2 Fixation	Equation 31	$106CO_2 + 8N_2 + H_3PO_4 + 130H_2O \xrightarrow{h\nu} (CH_2O)_{106}(NH_3)_{16}(H_3PO_4) + 118O_2$	$F_{\text{fix,newN}} = \frac{R_{H_3PO_4,s}}{\tau_{\text{fix}}} L_{\text{assim,DIC}} L_{\text{fix,N2}}(1 - L_{\text{Redf}}) \chi_{\text{photo}}(t) r_P^N$		✓							
Productivity by Anoxygenic N_2 Fixation	Equation 34	$472FeO + 106CO_2 + 8N_2 + H_3PO_4 + 1322 \xrightarrow{h\nu} 472Fe(OH)_3 + (CH_2O)_{106}(NH_3)_{16}(H_3PO_4) + 484H_2O$	$F_{\text{fixation,FeO}} = \frac{R_{\text{FeO,s}}}{\tau_{\text{fix}}} L_{\text{assim,DIC}} L_{\text{assim,H}_3\text{PO}_4} L_{\text{fix,N2}}(1 - L_{\text{Redf}})(1 - \chi_{\text{photo}}(t))$		✓							
Productivity by Photoferrotrophy	Equation 28	$4FeO + CO_2 + \frac{16}{106}NH_3 + \frac{1}{106}H_3PO_4 + 11H_2O \xrightarrow{h\nu} 4Fe(OH)_3 + \frac{1}{106}(CH_2O)_{106}(NH_3)_{16}(H_3PO_4) + 5H_2O$	$F_{\text{ferrotrophy}} = \frac{R_{\text{FeO,s}}}{\tau_{\text{assim}}} L_{\text{assim,DIC}} L_{\text{assim,fixN}} L_{\text{assim,H}_3\text{PO}_4}(1 - L_{\text{anox,O}_2,s})$		✓							
Remineralization by Ammonification	Equation 40	$(CH_2O)_{106}(NH_3)_{16}(H_3PO_4) + 106O_2 \rightarrow 106CO_2 + 16NH_3 + H_3PO_4 + 106H_2O$	$F_{\text{ammon},i} = \frac{R_{\text{OC},i}}{\tau_{\text{ourm},i}} L_{\text{ammon,O}_2,i}$		✓	✓	✓	✓				
Remineralization by Denitrification	Equation 43	$(CH_2O)_{106}(NH_3)_{16}(H_3PO_4) + \frac{424}{5}HNO_3 \rightarrow 106CO_2 + \frac{212}{5}N_2 + 16NH_3 + H_3PO_4 + \frac{742}{5}H_2O$	$F_{\text{denit},i} = \frac{R_{\text{OC},i}}{\tau_{\text{axm},i}}(1 - L_{\text{ammon,O}_2,i}) L_{\text{denit,HNO3},i}$		✓	✓	✓	✓				
Remineralization by Methanogenesis	Equation 44	$(CH_2O)_{106}(NH_3)_{16}(H_3PO_4) \rightarrow 53CO_2 + 53CH_4 + 16NH_3 + H_3PO_4$	$F_{\text{methgen},i} = \frac{R_{\text{OC},i}}{\tau_{\text{axm},i}}(1 - L_{\text{ammon,O}_2,i})(1 - L_{\text{denit,HNO3},i})$		✓	✓	✓	✓				
Methanotrophy	Equation 46	$CH_4 + 2O_2 \rightarrow CO_2 + 2H_2O$	$F_{\text{mtrophy},i} = \frac{R_{\text{CH4},i}}{\tau_{\text{mtrophy}}} L_{\text{mtrophy,O}_2,i}$		✓	✓	✓	✓				
Phosphate scavenging	Equation 67	$(CH_2O)_{106}(NH_3)_{16}(H_3PO_4) \rightarrow (CH_2O)_{106}(NH_3)_{16} + H_3PO_4(aq)$	$F_{\text{scav,i}} = \frac{R_{\text{OP},i}}{\tau_{\text{sink},i}}(1 - L_{H_3PO_4,\text{assim}})(1 - L_{\text{O}_2,\text{anox},i}) f_{\text{scav}}$			✓		✓				
Phosphate iron-sorption	Equation 69	$Fe(OH)_3 + H_3PO_4 \rightarrow FePO_4 + 3H_2O$	$F_{\text{sorb},i} = \frac{R_{\text{FeOH3},i}}{\tau_{\text{scab}}}[H_3PO_4]_i K_{\text{ads}}(1 - L_{\text{pH,sorb},i})$		✓	✓	✓	✓				
Geologic Fluxes												
Apatite burial	Equation 74	$H_3PO_4(aq) \rightarrow H_3PO_4(u)$	$F_{\text{burial,PO4},i} = F_{\text{burial,CaCO3},i} \frac{[H_3PO_4]_i}{[H_3PO_4]_0} f_{\text{apatite}}$			✓		✓	✓			
Iron-oxide P burial	Equation 70	$FePO_4 + 3H_2O \rightarrow Fe(OH)3 + H_3PO_4$	$F_{\text{burial,FePO4},i} = \frac{R_{\text{FePO4},i}}{\tau_{\text{sink,i,0}} \chi_{\text{eros}}(t)}$			✓		✓	✓			
NH_4 subduction	Equation 76	$(NH_4)_2SiO_3(o) \rightarrow 2NH_4(m) + SiO_2 + H_2O$	$F_{\text{subduct,NH4}} = \frac{R_{\text{NH4,o}}}{\tau_{\text{sub}}} f_{\text{sub,o}}$							✓		✓
$CaCO_3$ subduction	Equation 77	$CaCO_3(o) \rightarrow CaO + CO_2(m)$	$F_{\text{subduct,CaCO3}} = \frac{f_{\text{subu}} R_{\text{CaCO3,u}} + f_{\text{sub,o}} R_{\text{CaCO3,o}}}{\tau_{\text{sub}}}$						✓	✓		✓
Carbonate Volcanism	Equation 82	$CaCO_3 + SiO_2 \xrightarrow{heat} CO_2\uparrow + CaSiO_3$	$F_{\text{volc,CaCO3}} = \frac{R_{\text{CaCO3,u}} + R_{\text{CaCO3,o}}}{\tau_{\text{sub}}} f_{\text{volc,CaCO3}}$	✓					✓			
Organic Volcanism	Equation 81	$(CH_2O)_{106}(NH_3)_{16}(H_3PO_4) \xrightarrow{heat} 53CO_2\uparrow + 53CH_4\uparrow + 16NH_3\uparrow + H_3PO_4$	$F_{\text{volc,OC}} = \frac{R_{\text{OC,u}}}{\tau_{\text{sub}}} f_{\text{volc,OC}}$	✓					✓			
NH_4 Volcanism	Equation 83	$(NH_4)_2SiO_3 \xrightarrow{heat} 2NH_3\uparrow + SiO_2 + H_2O$	$F_{\text{volc,NH4}} = \frac{R_{\text{NH4,o}}}{\tau_{\text{sub}}} f_{\text{volc,NH4}}$	✓						✓		

Geochemistry, Geophysics, Geosystems

10.1029/2023GC011252

Table A4
Continued

Flux name	Equation number	Stoichiometry	Parameterization	Reservoirs							
				a	*s*	*n*	*d*	*z*	*u*	*o*	*c*	*m*
NH_4 recrystallization	Equation 85	$(NH_4)_2SiO_3(o) \rightarrow (NH_4)_2SiO_3(c)$	$F_{cryst,NH4} = \frac{R_{NH4,c}}{\tau_{sub}} f_{cryst,NH4}$							✓	✓	
Carbonate Metamorphism	Equation 86	$CaCO_3 \overset{heat}{\rightarrow} CO_2\uparrow + CaO$	$F_{meta,CaCO3} = \frac{R_{CaCO3,c}}{\tau_{meta}}$	✓							✓	
Organic Metamorphism	Equation 86	$(CH_2O)_{106}(NH_3)_{16}(H_3PO_4) \overset{heat}{\rightarrow} 53\,CO_2\uparrow + 53\,CH_4\uparrow + 16\,NH_3\uparrow H_3PO_4$	$F_{meta,OC} = \frac{R_{OC,c}}{\tau_{meta}}$	✓							✓	
NH_4 Metamorphism	Equation 86	$(NH_4)_2SiO_3 \overset{heat}{\rightarrow} 2\,NH_2\uparrow + 2\,H_2O + SiO_2$	$F_{meta,NH4} = \frac{R_{NH4,c}}{\tau_{meta}}$	✓							✓	
Carbonate weathering	Equation 96	$CaCO_3 + H_2O + CO_2 \rightarrow Ca^{2+} + 2HCO_3^-$	$F_{wthr,CaCO3} = \frac{R_{CaCO3,c}}{\tau_{wcarb}} S_{carb}(t,T,CO_2)$	✓	✓						✓	
Apatite weathering	Equation 97	$H_3PO_4(c) \rightarrow H_3PO_4(aq)$	$F_{wthr,CP} = \frac{R_{CP,c}}{\tau_{wcarb}/\chi_{fungi}(t)} S_{carb}(t,T,CO_2)$	✓	✓						✓	
Silicate weathering	Equation 102	$CaSiO_3(c) + H_2O + 2\,CO_2(a) \rightarrow Ca^{2+} + 2\,HCO_3^-(aq) + SiO_2$	$F_{wthr,sil} = 2\frac{R_{SiO3,c}}{\tau_{wsil}} S_{sil}(t,T,CO_2)$	✓	✓						✓	
Silicate-bound P weathering	Equation 104	$H_3PO_4(c) \rightarrow H_3PO_4(aq)$	$F_{wthr,SP} = \frac{R_{SP,c}}{\tau_{wsil}/\chi_{fungi}(t)} S_{sil}(t,T,CO_2)$	✓	✓						✓	
Ammonium weathering	Equation 103	$(NH_4)_2SiO_3 + 2CO_2(a) + H_2O \rightarrow 2\,NH_4^+(aq) + SiO_2 + 2\,HCO_3^-(aq)$	$F_{wthr,NH4} = \frac{R_{NH4,c}}{\tau_{wsil}} S_{sil}(t,T,CO_2)$	✓	✓						✓	
Iron oxidative weathering	Equation 105	$Fe_2SiO_4 + CO_2(a) + H_2O + \frac{1}{2}O_2(a) \rightarrow Fe_2O_3(c) + H_2CO_3(aq) + SiO_2$	$F_{wthr,Feox} = \frac{R_{Fe2SiO4,c}}{\tau_{wsil}} \sqrt{fO_2} S_{sil}(t,T,CO_2)$	✓							✓	
Oxidative weathering	Equation 107	$(CH_2O)_{106}(NH_3)_{16}(H_3PO_4) + 106\,O_2 \rightarrow 106\,CO_2 + 16\,NH_3 + H_3PO_4 + 106\,H_2O$	$F_{wthr,OC} = \frac{R_{OC,c}}{\tau_{wox}} \sqrt{fO_2}$	✓	✓						✓	
Reverse weathering	Equation 109	$Ca^{2+} + 2\,HCO_3^- + SiO_2 \rightarrow CaSiO_3 + 2\,CO_2 + H_2O$	$F_{revwthr,i} = 2k_{rw,i}(pH_i)[Si]_i(pH_i)V_i$			✓		✓				
Seafloor weathering	Equation 112	$CO_2(aq) + CaSiO_3 \rightarrow CaCO_3 + SiO_2$	$F_{sfw} = k_{sfw} S_{sfw}([CO_2]_z)$					✓		✓		
Hydrothermal alteration	Equation 114	$2\,NH_4^+(aq) + SiO_2 + 2\,HCO_3^- \rightarrow (NH_4)_2SiO_3 + 2\,CO_2(aq) + H_2O$	$F_{hyd} = [NH_4^+]_z \rho_{oc} k_{hyd} S_{sfw}([CO_2]_z)$					✓		✓		
NH_3 mantle outgassing	Equation 116	$NH_3(m) \rightarrow NH_3(a)$	$F_{mantle,NH3} = f_{red} F_{mantle,N}$	✓								✓
CH_4 mantle outgassing	Equation 116	$CH_4(m) \rightarrow CH_4(a)$	$F_{mantle,CH4} = f_{red} F_{mantle,C}$	✓								✓
N_2 mantle outgassing	Equation 117	$N_2(m) \rightarrow N_2(a)$	$F_{mantle,N2} = (1 - f_{red}) F_{mantle,N}$	✓								✓
CO_2 mantle outgassing	Equation 117	$CO_2(m) \rightarrow CO_2(a)$	$F_{mantle,CO2} = (1 - f_{red}) F_{mantle,C}$	✓								✓
FeO mantle outgassing	Equation 13	$FeO(m) \rightarrow FeO(d)$	$F_{mantle,FeO} = F_{mantle,Fe,0}\left(\chi_{mantle} + \frac{(1-\chi_{mantle})t}{4.5\times10^9}\right)$				✓					✓

Note. All model fluxes with unique stoichiometries.

Table A5
All Model Speciation Stoichiometries

Flux name	Equation number	Stoichiometry	Parameterization	Reservoirs								
				A	*s*	*n*	*d*	*z*	*u*	*o*	*c*	*m*
CO_2 speciation	Equation 8	$2H^+ + CO_3^{2-} \rightarrow CO_2 + H_2O$	$[CO_2]_i = \frac{[DIC]_i}{\left(1+\frac{K_{1,i}}{[H^+]_i}+\frac{K_{1,i}K_{2,i}}{[H^+]_i^2}\right)}$		✓	✓	✓	✓				
CO_3^{2-} speciation	Equation 9	$HCO_3^- \rightarrow H^+ + CO_3^{2-}$	$[CO_3^{2-}]_i = \frac{[DIC]_i}{\left(1+\frac{[H^+]_i}{K_{2,i}}+\frac{[H^+]_i^2}{K_{1,i}K_{2,i}}\right)}$		✓	✓	✓	✓				
HCO_3^- speciation	Equation 10	$CO_2 + H_2O \rightarrow H^+ + HCO_3^-$	$[HCO_3^-]_i = \frac{[DIC]_i}{\left(1+\frac{[H^+]_i}{K_{1,i}}+\frac{K_{2,i}}{[H^+]_i}\right)}$		✓	✓	✓	✓				
NH_3 speciation	Equation 11	$NH_4^+ \rightarrow NH_3 + H^+$	$[NH_3]_i = \frac{[RN]_i}{\left(1+\frac{[H^+]_i}{K_{N,i}}\right)}$		✓	✓	✓	✓				
NH_4^+ speciation	Equation 12	$NH_3 + H^+ \rightarrow NH_4^+$	$[NH_4^+]_i = \frac{[NH_3]_i[H^+]_i}{K_{N,i}}$		✓	✓	✓	✓				

Appendix B: Formulae for Aqueous Speciation

This appendix details calculations for equilibrium speciation between ammonia-ammonium (Appendix B1), for DIC species and carbonate saturation state (Appendix B2), and provides the thermodynamic equilibrium constants for all speciation reactions (Table B1).

Table B1
Thermodynamic Equilibrium Speciation Constants for the EONS Model

Parameter	Definition	Value	Units
Ammonia equilibrium reaction: $NH_4^+ \rightleftharpoons NH_3 + H^+$			
$pK_{N,s}$	Surface ocean rate constant	−9.2562	
$pK_{N,n}$	Neritic sediments rate constant	−9.2562	
$pK_{N,d}$	Deep ocean rate constant	−10.0243	
$pK_{N,z}$	Deep sediments rate constant	−10.0834	
$K_{N,s}$	Surface ocean dissociation constant	5.5434×10^{-10}	mol/kg
$K_{N,n}$	Neritic sediments dissociation constant	5.5434×10^{-10}	mol/kg
$K_{N,d}$	Deep ocean dissociation constant	9.4553×10^{-11}	mol/kg
$K_{N,z}$	Deep sediments dissociation constant	8.2537×10^{-11}	mol/kg
Protonation reaction: $HCO_3^- \rightleftharpoons CO_3^{2-} + H^+$			
$pK_{1,s}$	Surface ocean rate constant	−5.8563	
$pK_{1,n}$	Neritic sediments rate constant	−5.8563	
$pK_{1,d}$	Deep ocean rate constant	−6.0675	
$pK_{1,z}$	Deep sediments rate constant	−6.0837	
$K_{1,s}$	Surface ocean equilibrium dissociation constant	1.4048×10^{-6}	mol/kg
$K_{1,n}$	Neritic sediments equilibrium dissociation constant	1.4048×10^{-6}	mol/kg
$K_{1,d}$	Deep ocean equilibrium dissociation constant	1.3134×10^{-6}	mol/kg
$K_{1,z}$	Deep sediments ocean equilibrium dissociation constant	1.2718×10^{-6}	mol/kg
Hydration reaction: $CO_2 + H_2O \rightleftharpoons H_2CO_3$			
$pK_{2,s}$	Surface ocean rate constant	−8.9249	
$pK_{2,n}$	Neritic sediments rate constant	−8.9249	
$pK_{2,d}$	Deep ocean rate constant	−9.3116	
$pK_{2,z}$	Deep sediment rate constant	−9.3409	
$K_{2,s}$	Surface ocean equilibrium dissociation constant	1.1967×10^{-9}	mol/kg

Table B1
Continued

Parameter	Definition	Value	Units
$K_{2,n}$	Neritic sediments equilibrium dissociation constant	1.1967×10^{-9}	mol/kg
$K_{2,d}$	Deep ocean equilibrium dissociation constant	6.4591×10^{-10}	mol/kg
$K_{2,z}$	Deep sediments equilibrium dissociation constant	6.0476×10^{-10}	mol/kg
Boric acid reaction: $B(OH)_4 \rightleftharpoons B(OH)_3 + OH^-$			
$pK_{B,s}$	Surface ocean rate constant	−8.5975	
$pK_{B,n}$	Neritic sediments rate constant	−8.5975	
$pK_{B,d}$	Deep ocean rate constant	−8.8625	
$pK_{B,z}$	Deep sediment rate constant	−8.8829	
$K_{B,s}$	Surface ocean equilibrium dissociation constant	2.5545×10^{-9}	mol/kg
$K_{B,n}$	Neritic sediments equilibrium dissociation constant	2.5545×10^{-9}	mol/kg
$K_{B,d}$	Deep ocean equilibrium dissociation constant	2.2530×10^{-9}	mol/kg
$K_{B,z}$	Deep sediments equilibrium dissociation constant	2.1635×10^{-9}	mol/kg
Ion water product reaction: $H_2O \rightleftharpoons H^+ + OH^-$			
$pK_{W,s}$	Surface ocean rate constant	−13.2173	
$pK_{W,n}$	Neritic sediments rate constant	−13.2173	
$pK_{W,d}$	Deep ocean rate constant	−14.1249	
$pK_{W,z}$	Deep sediments rate constant	−14.1960	
$K_{W,s}$	Surface ocean equilibrium dissociation constant	6.1075×10^{-14}	mol/kg
$K_{W,n}$	Neritic sediments equilibrium dissociation constant	6.107×10^{-14}	mol/kg
$K_{W,d}$	Deep ocean equilibrium dissociation constant	1.0392×10^{-14}	mol/kg
$K_{W,z}$	Deep sediments equilibrium dissociation constant	8.8603×10^{-15}	mol/kg

B1. NH_3 and NH_4^+ Speciation

Ammonia and ammonium exist in the ocean and reactive sedimentary reservoirs in equilibrium. The ammonium dissociation constant (K_N) depends on local salinity (S_i, in permil) and temperature (T_i, in Kelvin), and is based on an equation from Millero (1995).

$$K_{N,i} = \exp\left(\frac{-6285.33}{T_i} + 0.0001635T_i - 0.25444 + \left(0.46532 - \frac{123.7184}{T_i}\right)S_i^{0.5} + \left(-0.01992 + \frac{3.17556}{T_i}\right)S_i\right) \quad \text{(B1)}$$

B2. Carbon Speciation

Carbon species (CO_2, HCO_3^-, and CO_3^{2-}) exist in equilibrium within the DIC reservoir within the surface (s) and deep (d) ocean and in the porewaters of reactive sediments (n and z). Concentrations of hydrogen and hydroxyl ions ($[H^+]$ and $[OH^-]$) are calculated assuming equilibrium hydration and protonation reactions and a sixth-order polynomial equation solved for the single set of positive roots; the acid dissociation constants for protonation, hydration, boric acid, and ion water product (K_1, K_2, K_B,K_W) for these following equations depend on local salinity (S_i, in permil) and temperature (T_i, in Kelvin; Zeebe & Wolf-Gladrow, 2001). Pressure effects on the thermodynamic constants outlined below are treated the same as outlined in Zeebe and Wolf-Gladrow (2001) Appendix A.

$$K_{1,i} = \exp\left(2.83655 - \frac{2307.1266}{T_i} - 1.5529413\ln(T_i) - \left(0.207608410 + \frac{4.0484}{T_i}S_i^{0.5}\right) + 0.0846834S_i - 0.00654208S_i^{1.5} + \ln(1 - 0.001005S_i)\right) \quad \text{(B2)}$$

$$K_{2,i} = \exp\left(-9.226508 - \frac{3351.6106}{T_i} - 0.2005743\ln(T_i) - \left(0.106901773 + \frac{23.9722}{T_i}S_i^{0.5}\right) + 0.1130822S_i - 0.00846934S_i^{1.5} + \ln(1 - 0.001005S_i)\right) \quad \text{(B3)}$$

$$K_{B,i} = \exp\left(-8966.9 - 2890.53S_i^{0.5} - 77.942S_i + 1.728S_i^{1.5} - \frac{0.0996S_i^2}{T_i} + 148.0248 + 137.1942S_i^{0.5} + 1.62142S_i - \left(24.4344 + 25.085S_i^{0.5} + 0.2474S_i\right)\ln(T_i) + 0.053105S_i^{0.5}T_i\right) \quad \text{(B4)}$$

$$K_{W,i} = \exp\left(148.96502 - \frac{13847.26}{T_i} - 23.6521\ln(T_i) + \frac{118.67}{T_i} - 5.977 + 1.0495\ln(T_i)S_i^{0.5} - 0.01615S_i\right) \quad \text{(B5)}$$

The following sixth-order polynomial equation has been modified from the fifth-order polynomial in appendix A of Zeebe and Wolf-Gladrow (2001), to add in the effects of ammonia-ammonium speciation on TA. This equation is solved for hydrogen concentration for reservoir i:

$$[\mathrm{DIC}]_i\left(\frac{K_{1,i}}{[\mathrm{H}^+]_i} + 2\frac{K_{1,i}K_{2,i}}{[\mathrm{H}^+]_i^2}\right) = \left([\mathrm{TA}]_i - \frac{K_{B,i}[B_T]_i}{K_{B,i} + [\mathrm{H}^+]_i} - \frac{K_{W,i}}{[\mathrm{H}^+]_i} + [\mathrm{H}^+]_i - \frac{[RN]_iK_{N,i}}{K_{N,i} + [\mathrm{H}^+]_i}\right)\left(1 + \frac{K_{1,i}}{[\mathrm{H}^+]_i} + \frac{K_{1,i}K_{2,i}}{[\mathrm{H}^+]_i^2}\right) \quad \text{(B6)}$$

where $[B_T]_i$ is the total dissolved boron concentration in the ocean, taken to be a constant approximately equal to $4.16 \times 10^{-4}\frac{S_i}{35}$ (Zeebe & Wolf-Gladrow, 2001).

Calcium carbonate saturation state, Ω, is a product of (CO_3^{2-}) and a fixed [Ca^{2+}] divided by the aragonite solubility constant (K_a) which is dependant on local temperature (T_i), salinity (S_i), and pressure (P_i; Millero, 1995).

$$K_{a,i} = 10^{\left(-171.945 - 0.077993T_i + \frac{2903.293}{T_i} + 71.595\log(T_i) + \left(-0.068393 + 0.0017276T_i + \frac{88.135}{T_i}\right)S_i^{0.5} - 0.10018S_i + 0.0059415S_i^{1.5}\right)} \quad \text{(B7)}$$

Data Availability Statement

The EONS model is licensed under MIT and available for download on GitHub https://github.com/juliahorne/EONS.git (Horne & Goldblatt, 2024).

Acknowledgments
We thank Roberta Hamme and Jon Husson for helpful comments on our manuscript, and Kazumi Ozaki and Joshua Krissansen-Totton for insightful reviews which improved this paper. Financial support was provided by the Natural Sciences and Engineering Research Council of Canada (NSERC) through Discovery Grant RGPIN-2018-05929 and the Canadian Space Agency through FAST Grant 18FAVICB21. High Performance computing resources were provided through NSERC Research Tools and Equipment Grant RTI-2020-00277.

References

Ahm, A.-S. C., Bjerrum, C. J., Blättler, C. L., Swart, P. K., & Higgins, J. A. (2018). Quantifying early marine diagenesis in shallow-water carbonate sediments. *Geochimica et Cosmochimica Acta*, *236*, 140–159. https://doi.org/10.1016/j.gca.2018.02.042

Albarede, F., Thibon, F., Blichert-Toft, J., & Tsikos, H. (2020). Chemical archeoceanography. *Chemical Geology*, *548*, 119625. https://doi.org/10.1016/j.chemgeo.2020.119625

Alcott, L. J., Mills, B. J., & Poulton, S. W. (2019). Stepwise Earth oxygenation is an inherent property of global biogeochemical cycling. *Science*, *366*(6471), 1333–1337. https://doi.org/10.1126/science.aax6459

Anderson, L. A., & Sarmiento, J. L. (1994). Redfield ratios of remineralization determined by nutrient data analysis. *Global Biogeochemical Cycles*, *8*(1), 65–80. https://doi.org/10.1029/93gb03318

Bellefroid, E. J., Hood, A. V. S., Hoffman, P. F., Thomas, M. D., Reinhard, C. T., & Planavsky, N. J. (2018). Constraints on Paleoproterozoic atmospheric oxygen levels. *Proceedings of the National Academy of Sciences*, *115*(32), 8104–8109. https://doi.org/10.1073/pnas.1806216115

Bergman, N. M., Lenton, T. M., & Watson, A. J. (2004). COPSE: A new model of biogeochemical cycling over Phanerozoic time. *American Journal of Science*, *304*(5), 397–437. https://doi.org/10.2475/ajs.304.5.397

Berman-Frank, I., Chen, Y., Gao, Y., Fennel, K., Follows, M. J., Milligan, A. J., & Falkowski, P. G. (2008). *Feedbacks between the nitrogen, carbon and oxygen cycles*. *Nitrogen in the marine environment* (2nd ed., pp. 1537–1563). Elsevier.

Berner, R. A. (1991). A model for atmospheric CO_2 over phanerozoic time. *American Journal of Science*, *291*(4), 339–376. https://doi.org/10.2475/ajs.291.4.339

Berner, R. A. (2004). *The Phanerozoic carbon cycle: CO_2 and O_2*. Oxford University Press.

Berner, R. A. (2009). Phanerozoic atmospheric oxygen: New results using the GEOCARBSULF model. *American Journal of Science*, *309*(7), 603–606. https://doi.org/10.2475/07.2009.03

Bjerrum, C. J., & Canfield, D. E. (2002). Ocean productivity before about 1.9 Gyr ago limited by phosphorus adsorption onto iron oxides. *Nature*, *417*(6885), 159–162. https://doi.org/10.1038/417159a

Bjerrum, C. J., & Canfield, D. E. (2004). New insights into the burial history of organic carbon on the early Earth. *Geochemistry, Geophysics, Geosystems*, *5*(8), Q08001. https://doi.org/10.1029/2004gc000713

Blichert-Toft, J., & Albarede, F. (1994). Short-lived chemical heterogeneities in the Archean mantle with implications for mantle convection. *Science*, *263*(5153), 1593–1596. https://doi.org/10.1126/science.263.5153.1593

Boudreau, B. P. (1996). The diffusive tortuosity of fine-grained unlithified sediments. *Geochimica et Cosmochimica Acta*, *60*(16), 3139–3142. https://doi.org/10.1016/0016-7037(96)00158-5

Brady, P. V., & Carroll, S. A. (1994). Direct effects of CO_2 and temperature on silicate weathering: Possible implications for climate control. *Geochimica et Cosmochimica Acta*, *58*(7), 1853–1856. https://doi.org/10.1016/0016-7037(94)90543-6

Braterman, P. S., Cairns-Smith, A. G., & Sloper, R. W. (1983). Photo-oxidation of hydrated Fe^{2+}—Significance for banded iron formations. *Nature*, *303*(5913), 163–164. https://doi.org/10.1038/303163a0

Burkhardt, S., Amoroso, G., Riebesell, U., & Sültemeyer, D. (2001). CO_2 and HCO_3 uptake in marine diatoms acclimated to different CO_2 concentrations. *Limnology and Oceanography*, *46*(6), 1378–1391. https://doi.org/10.4319/lo.2001.46.6.1378

Butcher, S. S., Charlson, R. J., Orians, G. H., & Wolfe, G. V. (1992). *Global biogeochemical cycles* (Vol. 50). Academic Press.

Byrne, B., & Goldblatt, C. (2014). Radiative forcing at high concentrations of well-mixed greenhouse gases. *Geophysical Research Letters*, *41*(1), 152–160. https://doi.org/10.1002/2013gl058456

Canfield, D. E., Poulton, S. W., & Narbonne, G. M. (2007). Late-Neoproterozoic deep-ocean oxygenation and the rise of animal life. *Science*, *315*(5808), 92–95. https://doi.org/10.1126/science.1135013

Canfield, D. E., Rosing, M. T., & Bjerrum, C. (2006). Early anaerobic metabolisms. *Philosophical Transactions of the Royal Society B: Biological Sciences*, *361*(1474), 1819–1836. https://doi.org/10.1098/rstb.2006.1906

Canfield, D. E., Zhang, S., Frank, A. B., Wang, X., Wang, H., Su, J., et al. (2018). Highly fractionated chromium isotopes in Mesoproterozoic-aged shales and atmospheric oxygen. *Nature Communications*, *9*(1), 2871. https://doi.org/10.1038/s41467-018-05263-9

Canil, D. (1997). Vanadium partitioning and the oxidation state of Archaean komatiite magmas. *Nature*, *389*(6653), 842–845. https://doi.org/10.1038/39860

Canuel, E. A., & Hardison, A. K. (2018). Carbon cycle. In W. M. White (Ed.), *Encyclopedia of geochemistry: A comprehensive reference source on the chemistry of the Earth* (pp. 191–194).

Carlson, R. W. (2005). *The mantle and core: Treatise on geochemistry* (Vol. 2). Elsevier.

Catling, D. C., & Claire, M. W. (2005). How Earth's atmosphere evolved to an oxic state: A status report. *Earth and Planetary Science Letters*, *237*(1–2), 1–20. https://doi.org/10.1016/j.epsl.2005.06.013

Catling, D. C., & Zahnle, K. J. (2020). The Archean atmosphere. *Science Advances*, *6*(9), eaax1420. https://doi.org/10.1126/sciadv.aax1420

Catling, D. C., Zahnle, K. J., & McKay, C. P. (2001). Biogenic methane, hydrogen escape, and the irreversible oxidation of early Earth. *Science*, *293*(5531), 839–843. https://doi.org/10.1126/science.1061976

Ciais, P., Sabine, C., Bala, G., Bopp, L., Brovkin, V., Canadell, J., et al. (2014). Carbon and other biogeochemical cycles. In *Climate change 2013: The physical science basis. Contribution of Working Group I to the Fifth Assessment Report of the Intergovernmental Panel on Climate Change* (pp. 465–570). Cambridge University Press.

Claire, M. W., Catling, D. C., & Zahnle, K. J. (2006). Biogeochemical modelling of the rise in atmospheric oxygen. *Geobiology*, *4*(4), 239–269. https://doi.org/10.1111/j.1472-4669.2006.00084.x

Claire, M. W., Kasting, J. F., Domagal-Goldman, S. D., Stüeken, E. E., Buick, R., & Meadows, V. S. (2014). Modeling the signature of sulfur mass-independent fractionation produced in the Archean atmosphere. *Geochimica et Cosmochimica Acta*, *141*, 365–380. https://doi.org/10.1016/j.gca.2014.06.032

Clift, P. D. (2017). A revised budget for Cenozoic sedimentary carbon subduction. *Reviews of Geophysics*, *55*(1), 97–125. https://doi.org/10.1002/2016rg000531

Coogan, L. A., & Gillis, K. M. (2013). Evidence that low-temperature oceanic hydrothermal systems play an important role in the silicate-carbonate weathering cycle and long-term climate regulation. *Geochemistry, Geophysics, Geosystems*, *14*(6), 1771–1786. https://doi.org/10.1002/ggge.20113

Coogan, L. A., & Gillis, K. M. (2018). Low-temperature alteration of the seafloor: Impacts on ocean chemistry. *Annual Review of Earth and Planetary Sciences*, *46*(1), 21–45. https://doi.org/10.1146/annurev-earth-082517-010027

Crockford, P., & Halevy, I. (2022). Questioning the paradigm of a phosphate-limited Archean biosphere. *Geophysical Research Letters*, *49*(17), e2022GL099818. https://doi.org/10.1029/2022gl099818

Crockford, P. W., Hayles, J. A., Bao, H., Planavsky, N. J., Bekker, A., Fralick, P. W., et al. (2018). Triple oxygen isotope evidence for limited mid-Proterozoic primary productivity. *Nature*, *559*(7715), 613–616. https://doi.org/10.1038/s41586-018-0349-y

Crockford, P. W., On, Y. M. B., Ward, L. M., Milo, R., & Halevy, I. (2023). The geologic history of primary productivity. *Current Biology*, *33*(21), 4741–4750. https://doi.org/10.1016/j.cub.2023.09.040

Crowe, S. A., Døssing, L. N., Beukes, N. J., Bau, M., Kruger, S. J., Frei, R., & Canfield, D. E. (2013). Atmospheric oxygenation three billion years ago. *Nature*, *501*(7468), 535–538. https://doi.org/10.1038/nature12426

Crowe, S. A., Jones, C., Katsev, S., Magen, C., O'Neill, A. H., Sturm, A., et al. (2008). Photoferrotrophs thrive in an Archean ocean analogue. *Proceedings of the National Academy of Sciences*, *105*(41), 15938–15943. https://doi.org/10.1073/pnas.0805313105

Daines, S. J., Mills, B. J., & Lenton, T. M. (2017). Atmospheric oxygen regulation at low Proterozoic levels by incomplete oxidative weathering of sedimentary organic carbon. *Nature Communications*, *8*(1), 14379. https://doi.org/10.1038/ncomms14379

Derry, L. A. (2010). A burial diagenesis origin for the Ediacaran Shuram–Wonoka carbon isotope anomaly. *Earth and Planetary Science Letters*, *294*(1), 152–162. https://doi.org/10.1016/j.epsl.2010.03.022

Derry, L. A. (2014). Organic carbon cycling and the lithosphere.

Dhuime, B., Hawkesworth, C. J., Delavault, H., & Cawood, P. A. (2018). Rates of generation and destruction of the continental crust: Implications for continental growth. *Philosophical Transactions of the Royal Society A: Mathematical, Physical and Engineering Sciences*, *376*(2132), 20170403. https://doi.org/10.1098/rsta.2017.0403

Dickson, A. G. (1981). An exact definition of total alkalinity and a procedure for the estimation of alkalinity and total inorganic carbon from titration data. *Deep-Sea Research, Part A: Oceanographic Research Papers*, *28*(6), 609–623. https://doi.org/10.1016/0198-0149(81)90121-7

Dinçer, A. R., & Kargı, F. (2000). Kinetics of sequential nitrification and denitrification processes. *Enzyme and Microbial Technology*, *27*(1–2), 37–42. https://doi.org/10.1016/s0141-0229(00)00145-9

Emerson, S., & Hedges, J. (2008). *Chemical oceanography and the marine carbon cycle*. Cambridge University Press.

Falkowski, P. G. (2012). The global carbon cycle: Biological processes. *Fundamentals of Geobiology* (pp. 5–19).

Fennel, K., Follows, M., & Falkowski, P. G. (2005). The co-evolution of the nitrogen, carbon and oxygen cycles in the Proterozoic ocean. *American Journal of Science*, *305*(6–8), 526–545. https://doi.org/10.2475/ajs.305.6-8.526

Feulner, G. (2012). The faint young Sun problem. *Reviews of Geophysics*, *50*(2), RG2006. https://doi.org/10.1029/2011rg000375

Fischer, G., & Karakaş, G. (2009). Sinking rates and ballast composition of particles in the Atlantic Ocean: Implications for the organic carbon fluxes to the deep ocean. *Biogeosciences*, *6*(1), 85–102. https://doi.org/10.5194/bg-6-85-2009

Froelich, P., Klinkhammer, G. P., Bender, M. L., Luedtke, N. A., Heath, G. R., Cullen, D., et al. (1979). Early oxidation of organic matter in pelagic sediments of the eastern equatorial Atlantic: Suboxic diagenesis. *Geochimica et Cosmochimica Acta*, *43*(7), 1075–1090. https://doi.org/10.1016/0016-7037(79)90095-4

Garduno Ruiz, D. I., Goldblatt, C., & Ahm, A.-S. (2023). Climate shapes the oxygenation of Earth's atmosphere across the Great Oxidation Event. *Earth and Planetary Science Letters*, *607*, 118071. https://doi.org/10.1016/j.epsl.2023.118071

Gillis, K. M., & Coogan, L. A. (2011). Secular variation in carbon uptake into the ocean crust. *Earth and Planetary Science Letters*, *302*(3–4), 385–392. https://doi.org/10.1016/j.epsl.2010.12.030

Glasspool, I. J., & Scott, A. C. (2010). Phanerozoic concentrations of atmospheric oxygen reconstructed from sedimentary charcoal. *Nature Geoscience*, *3*(9), 627–630. https://doi.org/10.1038/ngeo923

Goldblatt, C., Claire, M. W., Lenton, T. M., Matthews, A. J., Watson, A. J., & Zahnle, K. J. (2009). Nitrogen-enhanced greenhouse warming on early Earth. *Nature Geoscience*, *2*(12), 891–896. https://doi.org/10.1038/ngeo692

Goldblatt, C., Lenton, T. M., & Watson, A. J. (2006). Bistability of atmospheric oxygen and the Great Oxidation. *Nature*, *443*(7112), 683–686. https://doi.org/10.1038/nature05169

Goldblatt, C., McDonald, V. L., & McCusker, K. E. (2021). Earth's long-term climate stabilized by clouds. *Nature Geoscience*, *14*(3), 143–150. https://doi.org/10.1038/s41561-021-00691-7

Goldblatt, C., & Zahnle, K. J. (2011). Faint young Sun paradox remains. *Nature*, *474*(7349), E1. https://doi.org/10.1038/nature09961

Goody, R. M., & Yung, Y. L. (1995). *Atmospheric radiation: Theoretical basis*. Oxford University Press.

Gough, D. O. (1981). Solar interior structure and luminosity variations. In *Physics of Solar Variations: Proceedings of the 14th ESLAB Symposium Held in Scheveningen, The Netherlands, 16–19 September, 1980* (pp. 21–34). Springer.

Gregory, B. S., Claire, M. W., & Rugheimer, S. (2021). Photochemical modelling of atmospheric oxygen levels confirms two stable states. *Earth and Planetary Science Letters*, *561*, 116818. https://doi.org/10.1016/j.epsl.2021.116818

Gruber, N. (2008). The marine nitrogen cycle: Overview and challenges. *Nitrogen in the marine environment*, *2*, 1–50.

Guimond, C. M., Noack, L., Ortenzi, G., & Sohl, F. (2021). Low volcanic outgassing rates for a stagnant lid Archean earth with graphite-saturated magmas. *Physics of the Earth and Planetary Interiors*, *320*, 106788. https://doi.org/10.1016/j.pepi.2021.106788

Hao, J., Knoll, A. H., Huang, F., Schieber, J., Hazen, R. M., & Daniel, I. (2020). Cycling phosphorus on the Archean Earth: Part II. Phosphorus limitation on primary production in Archean ecosystems. *Geochimica et Cosmochimica Acta*, *280*, 360–377. https://doi.org/10.1016/j.gca.2020.04.005

Hawkesworth, C., Cawood, P. A., & Dhuime, B. (2019). Rates of generation and growth of the continental crust. *Geoscience Frontiers*, *10*(1), 165–173. https://doi.org/10.1016/j.gsf.2018.02.004

Hayes, J. M., & Waldbauer, J. R. (2006). The carbon cycle and associated redox processes through time. *Philosophical Transactions of the Royal Society B: Biological Sciences*, *361*(1470), 931–950. https://doi.org/10.1098/rstb.2006.1840

Haynes, W. M. (2014). *CRC handbook of chemistry and physics*. CRC Press.

Heckman, D. S., Geiser, D. M., Eidell, B. R., Stauffer, R. L., Kardos, N. L., & Hedges, S. B. (2001). Molecular evidence for the early colonization of land by fungi and plants. *Science*, *293*(5532), 1129–1133. https://doi.org/10.1126/science.1061457

Herman, J. S., & White, W. B. (1985). Dissolution kinetics of dolomite: Effects of lithology and fluid flow velocity. *Geochimica et Cosmochimica Acta*, *49*(10), 2017–2026. https://doi.org/10.1016/0016-7037(85)90060-2

Hiatt, W. C., & Grady, C. P. (2008). An updated process model for carbon oxidation, nitrification, and denitrification. *Water Environment Research*, *80*(11), 2145–2156. https://doi.org/10.2175/106143008x304776

Hoffland, E., Kuyper, T. W., Wallander, H., Plassard, C., Gorbushina, A. A., Haselwandter, K., et al. (2004). The role of fungi in weathering. *Frontiers in Ecology and the Environment*, *2*(5), 258–264. https://doi.org/10.2307/3868266

Hoffman, P. F. (2013). The Great Oxidation and a Siderian snowball Earth: MIF-S based correlation of Paleoproterozoic glacial epochs. *Chemical Geology*, *362*, 143–156. https://doi.org/10.1016/j.chemgeo.2013.04.018

Hoffman, P. F., Kaufman, A. J., Halverson, G. P., & Schrag, D. P. (1998). A Neoproterozoic snowball Earth. *Science*, *281*(5381), 1342–1346. https://doi.org/10.1126/science.281.5381.1342

Holland, H. D. (2002). Volcanic gases, black smokers, and the Great Oxidation Event. *Geochimica et Cosmochimica Acta*, *66*(21), 3811–3826. https://doi.org/10.1016/s0016-7037(02)00950-x

Holloway, J. M., & Dahlgren, R. A. (2002). Nitrogen in rock: Occurrences and biogeochemical implications. *Global Biogeochemical Cycles*, *16*(4), 65-1–65-17. https://doi.org/10.1029/2002gb001862

Horne, J., & Goldblatt, C. (2024). juliahorne/EONS: EONS model initial release (version 1.0.0) [Software]. Zenodo. https://doi.org/10.5281/zenodo.10515733

Hunten, D. M. (1973). The escape of light gases from planetary atmospheres. *Journal of the Atmospheric Sciences*, *30*(8), 1481–1494. https://doi.org/10.1175/1520-0469(1973)030<1481:teolgf>2.0.co;2

Husson, J. M., & Peters, S. E. (2017). Atmospheric oxygenation driven by unsteady growth of the continental sedimentary reservoir. *Earth and Planetary Science Letters*, *460*, 68–75. https://doi.org/10.1016/j.epsl.2016.12.012

Ibarra, D. E., Rugenstein, J. K. C., Bachan, A., Baresch, A., Lau, K. V., Thomas, D. L., et al. (2019). Modeling the consequences of land plant evolution on silicate weathering. *American Journal of Science*, *319*(1), 1–43. https://doi.org/10.2475/01.2019.01

Ingalls, M., Grotzinger, J. P., Present, T., Rasmussen, B., & Fischer, W. W. (2022). Carbonate-associated phosphate (CAP) indicates elevated phosphate availability in Neoarchean shallow marine environments. *Geophysical Research Letters*, *49*(6), e2022GL098100. https://doi.org/10.1029/2022GL098100

Isson, T. T., & Planavsky, N. J. (2018). Reverse weathering as a long-term stabilizer of marine pH and planetary climate. *Nature*, *560*(7719), 471–475. https://doi.org/10.1038/s41586-018-0408-4

Iversen, N., & Jørgensen, B. B. (1993). Diffusion coefficients of sulfate and methane in marine sediments: Influence of porosity. *Geochimica et Cosmochimica Acta*, *57*(3), 571–578. https://doi.org/10.1016/0016-7037(93)90368-7

Izon, G., Luo, G., Uveges, B. T., Beukes, N., Kitajima, K., Ono, S., et al. (2022). Bulk and grain-scale minor sulfur isotope data reveal complexities in the dynamics of Earth's oxygenation. *Proceedings of the National Academy of Sciences*, *119*(13), e2025606119. https://doi.org/10.1073/pnas.2025606119

Jahnke, R. A. (2000). *The phosphorus cycle*. *Earth system science: From biogeochemical cycles to global change* (pp. 360–376). Elsevier Academic Press.

Jaisi, D. P., Blake, R. E., & Kukkadapu, R. K. (2010). Fractionation of oxygen isotopes in phosphate during its interactions with iron oxides. *Geochimica et Cosmochimica Acta*, *74*(4), 1309–1319. https://doi.org/10.1016/j.gca.2009.11.010

Johnson, B., & Goldblatt, C. (2015). The nitrogen budget of Earth. *Earth-Science Reviews*, *148*, 150–173. https://doi.org/10.1016/j.earscirev.2015.05.006

Johnson, B. W., & Goldblatt, C. (2018). EarthN: A new Earth system nitrogen model. *Geochemistry, Geophysics, Geosystems*, *19*(8), 2516–2542. https://doi.org/10.1029/2017gc007392

Johnson, J. E., Gerpheide, A., Lamb, M. P., & Fischer, W. W. (2014). O_2 constraints from Paleoproterozoic detrital pyrite and uraninite. *Bulletin*, *126*(5–6), 813–830. https://doi.org/10.1130/b30949.1

Jones, C., Nomosatryo, S., Crowe, S. A., Bjerrum, C. J., & Canfield, D. E. (2015). Iron oxides, divalent cations, silica, and the early earth phosphorus crisis. *Geology*, *43*(2), 135–138. https://doi.org/10.1130/g36044.1

Jørgensen, B. B. (1977). Bacterial sulfate reduction within reduced microniches of oxidized marine sediments. *Marine Biology*, *41*(1), 7–17. https://doi.org/10.1007/bf00390576

Kaiser, S. I., Aretz, M., & Becker, R. T. (2016). The global Hangenberg Crisis (Devonian–Carboniferous transition): Review of a first-order mass extinction. *Geological Society, London, Special Publications*, *423*(1), 387–437. https://doi.org/10.1144/sp423.9

Kelemen, P. B., & Manning, C. E. (2015). Reevaluating carbon fluxes in subduction zones, what goes down, mostly comes up. *Proceedings of the National Academy of Sciences*, *112*(30), E3997–E4006. https://doi.org/10.1073/pnas.1507889112

Kendall, B., Anbar, A. D., Kappler, A., & Konhauser, K. O. (2012). The global iron cycle. *Fundamentals of Geobiology* (Vol. *1*, pp. 65–92).

Kharecha, P., Kasting, J., & Siefert, J. (2005). A coupled atmosphere–ecosystem model of the early Archean Earth. *Geobiology*, *3*(2), 53–76. https://doi.org/10.1111/j.1472-4669.2005.00049.x

Kipp, M. A., & Stüeken, E. E. (2017). Biomass recycling and Earth's early phosphorus cycle. *Science Advances*, *3*(11), eaao4795. https://doi.org/10.1126/sciadv.aao4795

Kirschvink, J. L., Gaidos, E. J., Bertani, L. E., Beukes, N. J., Gutzmer, J., Maepa, L. N., & Steinberger, R. E. (2000). Paleoproterozoic snowball Earth: Extreme climatic and geochemical global change and its biological consequences. *Proceedings of the National Academy of Sciences*, *97*(4), 1400–1405. https://doi.org/10.1073/pnas.97.4.1400

Knudsen, A. C., & Gunter, M. E. (2002). Sedimentary phosphorites—An example: Phosphoria formation, southeastern Idaho, USA. *Reviews in Mineralogy and Geochemistry*, *48*(1), 363–389. https://doi.org/10.2138/rmg.2002.48.9

Koltermann, K. P., Gouretski, V., & Jancke, K. (2011). Hydrographic Atlas of the World Ocean Circulation Experiment (WOCE): Volume 3: Atlantic Ocean.

Konhauser, K. O., Amskold, L., Lalonde, S. V., Posth, N. R., Kappler, A., & Anbar, A. (2007). Decoupling photochemical Fe (II) oxidation from shallow-water BIF deposition. *Earth and Planetary Science Letters*, *258*(1–2), 87–100. https://doi.org/10.1016/j.epsl.2007.03.026

Konhauser, K. O., Lalonde, S. V., Amskold, L., & Holland, H. D. (2007). Was there really an Archean phosphate crisis? *Science*, *315*(5816), 1234. https://doi.org/10.1126/science.1136328

Kopp, G., & Lean, J. L. (2011). A new, lower value of total solar irradiance: Evidence and climate significance. *Geophysical Research Letters*, *38*(1), L01706. https://doi.org/10.1029/2010GL045777

Kopp, R. E., Kirschvink, J. L., Hilburn, I. A., & Nash, C. Z. (2005). The Paleoproterozoic snowball Earth: A climate disaster triggered by the evolution of oxygenic photosynthesis. *Proceedings of the National Academy of Sciences*, *102*(32), 11131–11136. https://doi.org/10.1073/pnas.0504878102

Korenaga, J. (2006). Archean geodynamics and the thermal evolution of Earth. *Geophysical Monograph-American Geophysical Union*, *164*, 7.

Korenaga, J. (2010). Scaling of plate tectonic convection with pseudoplastic rheology. *Journal of Geophysical Research*, *115*(B11), B11405. https://doi.org/10.1029/2010jb007670

Kraal, P., Dijkstra, N., Behrends, T., & Slomp, C. P. (2017). Phosphorus burial in sediments of the sulfidic deep Black Sea: Key roles for adsorption by calcium carbonate and apatite authigenesis. *Geochimica et Cosmochimica Acta*, *204*, 140–158. https://doi.org/10.1016/j.gca.2017.01.042

Krause, A. J., Mills, B. J., Merdith, A. S., Lenton, T. M., & Poulton, S. W. (2022). Extreme variability in atmospheric oxygen levels in the late Precambrian. *Science Advances*, *8*(41), eabm8191. https://doi.org/10.1126/sciadv.abm8191

Krause, A. J., Mills, B. J., Zhang, S., Planavsky, N. J., Lenton, T. M., & Poulton, S. W. (2018). Stepwise oxygenation of the Paleozoic atmosphere. *Nature Communications*, *9*(1), 4081. https://doi.org/10.1038/s41467-018-06383-y

Kriest, I., & Oschlies, A. (2008). On the treatment of particulate organic matter sinking in large-scale models of marine biogeochemical cycles. *Biogeosciences*, *5*(1), 55–72. https://doi.org/10.5194/bg-5-55-2008

Krissansen-Totton, J., Arney, G. N., & Catling, D. C. (2018). Constraining the climate and ocean pH of the early Earth with a geological carbon cycle model. *Proceedings of the National Academy of Sciences*, *115*(16), 4105–4110. https://doi.org/10.1073/pnas.1721296115

Krissansen-Totton, J., Buick, R., & Catling, D. C. (2015). A statistical analysis of the carbon isotope record from the Archean to Phanerozoic and implications for the rise of oxygen. *American Journal of Science*, *315*(4), 275–316. https://doi.org/10.2475/04.2015.01

Krissansen-Totton, J., & Catling, D. C. (2020). A coupled carbon-silicon cycle model over Earth history: Reverse weathering as a possible explanation of a warm mid-Proterozoic climate. *Earth and Planetary Science Letters*, *537*, 116181. https://doi.org/10.1016/j.epsl.2020.116181

Krissansen-Totton, J., Kipp, M. A., & Catling, D. C. (2021). Carbon cycle inverse modeling suggests large changes in fractional organic burial are consistent with the carbon isotope record and may have contributed to the rise of oxygen. *Geobiology*, *19*(4), 342–363. https://doi.org/10.1111/gbi.12440

Krom, M. D., & Berner, R. A. (1980). The diffusion coefficients of sulfate, ammonium, and phosphate ions in anoxic marine sediments. *Limnology and Oceanography*, *25*(2), 327–337. https://doi.org/10.4319/lo.1980.25.2.0327

Lambers, H. (2022). Phosphorus acquisition and utilization in plants. *Annual Review of Plant Biology*, *73*(1), 11–126. https://doi.org/10.1146/annurev-arplant-102720-125738
Lenton, T. M. (2000). Land and ocean carbon cycle feedback effects on global warming in a simple Earth system model. *Tellus B: Chemical and Physical Meteorology*, *52*(5), 1159–1188. https://doi.org/10.3402/tellusb.v52i5.17097
Lenton, T. M., Dahl, T. W., Daines, S. J., Mills, B. J., Ozaki, K., Saltzman, M. R., & Porada, P. (2016). Earliest land plants created modern levels of atmospheric oxygen. *Proceedings of the National Academy of Sciences*, *113*(35), 9704–9709. https://doi.org/10.1073/pnas.1604787113
Lenton, T. M., Daines, S. J., & Mills, B. J. (2018). COPSE reloaded: An improved model of biogeochemical cycling over Phanerozoic time. *Earth-Science Reviews*, *178*, 1–28. https://doi.org/10.1016/j.earscirev.2017.12.004
Lenton, T. M., & Watson, A. J. (2004). Biotic enhancement of weathering, atmospheric oxygen and carbon dioxide in the Neoproterozoic. *Geophysical Research Letters*, *31*(5), L05202. https://doi.org/10.1029/2003GL018802
Li, G., & Elderfield, H. (2013). Evolution of carbon cycle over the past 100 million years. *Geochimica et Cosmochimica Acta*, *103*, 11–25. https://doi.org/10.1016/j.gca.2012.10.014
Libes, S. (2011). *Introduction to marine biogeochemistry*. Academic Press.
Liss, P. S., & Slater, P. G. (1974). Flux of gases across the air-sea interface. *Nature*, *247*(5438), 181–184. https://doi.org/10.1038/247181a0
Lodders, K., Fegley, B., & Lodders, F. (1998). *The planetary scientist's companion*. Oxford University Press on Demand.
Lovelock, J. (1972). Gaia as seen through the atmosphere. *Atmospheric Environment*, *6*(6), 579–580. https://doi.org/10.1016/0004-6981(72)90076-5
Lovelock, J. E., & Margulis, L. (1974). Atmospheric homeostasis by and for the biosphere: The Gaia hypothesis. *Tellus*, *26*(1–2), 2–10. https://doi.org/10.1111/j.2153-3490.1974.tb01946.x
Lucking, R., Huhndorf, S., Pfister, D. H., Plata, E. R., & Lumbsch, H. T. (2009). Fungi evolved right on track. *Mycologia*, *101*(6), 810–822. https://doi.org/10.3852/09-016
Luo, G., Ono, S., Beukes, N. J., Wang, D. T., Xie, S., & Summons, R. E. (2016). Rapid oxygenation of Earth's atmosphere 2.33 billion years ago. *Science Advances*, *2*(5), e1600134. https://doi.org/10.1126/sciadv.1600134
Lyons, T. W., Reinhard, C. T., & Planavsky, N. J. (2014). The rise of oxygen in Earth's early ocean and atmosphere. *Nature*, *506*(7488), 307–315. https://doi.org/10.1038/nature13068
Mackenzie, F. T., Lerman, A., & Andersson, A. J. (2004). Past and present of sediment and carbon biogeochemical cycling models. *Biogeosciences*, *1*(1), 11–32. https://doi.org/10.5194/bg-1-11-2004
Marais, D. J. D., Strauss, H., Summons, R. E., & Hayes, J. M. (1992). Carbon isotope evidence for the stepwise oxidation of the Proterozoic environment. *Nature*, *359*(6396), 605–609. https://doi.org/10.1038/359605a0
Millero, F. J. (1995). Thermodynamics of the carbon dioxide system in the oceans. *Geochimica et Cosmochimica Acta*, *59*(4), 661–677. https://doi.org/10.1016/0016-7037(94)00354-o
Millero, F. J. (1996). *Chemical oceanography* (p. 469). CRC Press.
Mills, B., Lenton, T. M., & Watson, A. J. (2014). Proterozoic oxygen rise linked to shifting balance between seafloor and terrestrial weathering. *Proceedings of the National Academy of Sciences*, *111*(25), 9073–9078. https://doi.org/10.1073/pnas.1321679111
Mills, B., Watson, A. J., Goldblatt, C., Boyle, R., & Lenton, T. M. (2011). Timing of Neoproterozoic glaciations linked to transport-limited global weathering. *Nature Geoscience*, *4*(12), 861–864. https://doi.org/10.1038/ngeo1305
Montgomery, D. R., & Brandon, M. T. (2002). Topographic controls on erosion rates in tectonically active mountain ranges. *Earth and Planetary Science Letters*, *201*(3), 481–489. https://doi.org/10.1016/S0012-821X(02)00725-2
Müller, R. D., Sdrolias, M., Gaina, C., & Roest, W. R. (2008). Age, spreading rates, and spreading asymmetry of the world's ocean crust. *Geochemistry, Geophysics, Geosystems*, *9*(4), Q04006. https://doi.org/10.1029/2007GC001743
Noack, L., Godolt, M., von Paris, P., Plesa, A., Stracke, B., Breuer, D., & Rauer, H. (2014). Can the interior structure influence the habitability of a rocky planet? *Planetary and Space Science*, *98*, 14–29. https://doi.org/10.1016/j.pss.2014.01.003
Olson, J. M. (2006). Photosynthesis in the Archean era. *Photosynthesis Research*, *88*(2), 109–117. https://doi.org/10.1007/s11120-006-9040-5
Olson, S., Jansen, M. F., Abbot, D. S., Halevy, I., & Goldblatt, C. (2022). The effect of ocean salinity on climate and its implications for Earth's habitability. *Geophysical Research Letters*, *49*(10), e2021GL095748. https://doi.org/10.1029/2021gl095748
Ozaki, K., Cole, D. B., Reinhard, C. T., & Tajika, E. (2022). CANOPS-GRB v1. 0: A new Earth system model for simulating the evolution of ocean–atmosphere chemistry over geologic timescales. *Geoscientific Model Development*, *15*(20), 7593–7639. https://doi.org/10.5194/gmd-15-7593-2022
Ozaki, K., & Reinhard, C. T. (2021). The future lifespan of Earth's oxygenated atmosphere. *Nature Geoscience*, *14*(3), 138–142. https://doi.org/10.1038/s41561-021-00693-5
Ozaki, K., Tajika, E., Hong, P. K., Nakagawa, Y., & Reinhard, C. T. (2018). Effects of primitive photosynthesis on Earth's early climate system. *Nature Geoscience*, *11*(1), 55–59. https://doi.org/10.1038/s41561-017-0031-2
Ozaki, K., Thompson, K. J., Simister, R. L., Crowe, S. A., & Reinhard, C. T. (2019). Anoxygenic photosynthesis and the delayed oxygenation of Earth's atmosphere. *Nature Communications*, *10*(1), 3026. https://doi.org/10.1038/s41467-019-10872-z
Padhi, C. M., Korenaga, J., & Ozima, M. (2012). Thermal evolution of Earth with xenon degassing: A self-consistent approach. *Earth and Planetary Science Letters*, *341*, 1–9. https://doi.org/10.1016/j.epsl.2012.06.013
Palta, M. M., & Hartnett, H. (2018). Nitrogen cycle. In *Encyclopedia of Earth Sciences series* (pp. 987–991). Springer Netherlands.
Pavlov, A. A., Brown, L. L., & Kasting, J. F. (2001). UV shielding of NH_3 and O_2 by organic hazes in the Archean atmosphere. *Journal of Geophysical Research*, *106*(E10), 23267–23287. https://doi.org/10.1029/2000je001448
Pavlov, A. A., Kasting, J. F., Brown, L. L., Rages, K. A., & Freedman, R. (2000). Greenhouse warming by CH_4 in the atmosphere of early Earth. *Journal of Geophysical Research*, *105*(E5), 11981–11990. https://doi.org/10.1029/1999je001134
Peters, S. E., & Husson, J. M. (2017). Sediment cycling on continental and oceanic crust. *Geology*, *45*(4), 323–326. https://doi.org/10.1130/g38861.1
Planavsky, N. J., Fakhraee, M., Bolton, E. W., Reinhard, C. T., Isson, T. T., Zhang, S., & Mills, B. J. (2022). On carbon burial and net primary production through Earth's history. *American Journal of Science*, *322*(3), 413–460. https://doi.org/10.2475/03.2022.01
Porder, S. (2019). How plants enhance weathering and how weathering is important to plants. *Elements: An International Magazine of Mineralogy, Geochemistry, and Petrology*, *15*(4), 241–246. https://doi.org/10.2138/gselements.15.4.241
Redfield, A. C., Ketchum, B. H., & Richards, F. A. (1963). The influence of organisms on the composition of seawater. *The Sea*, *2*, 26–77.
Rego, E. S., Busigny, V., Lalonde, S. V., Rossignol, C., Babinski, M., & Philippot, P. (2023). Low-phosphorus concentrations and important ferric hydroxide scavenging in Archean seawater. *PNAS Nexus*, *2*(3), pgad025. https://doi.org/10.1093/pnasnexus/pgad025
Reimink, J. R., Davies, J. H., & Ielpi, A. (2021). Global zircon analysis records a gradual rise of continental crust throughout the Neoarchean. *Earth and Planetary Science Letters*, *554*, 116654. https://doi.org/10.1016/j.epsl.2020.116654

Reinhard, C. T., Planavsky, N. J., Gill, B. C., Ozaki, K., Robbins, L. J., Lyons, T. W., et al. (2017). Evolution of the global phosphorus cycle. *Nature*, *541*(7637), 386–389. https://doi.org/10.1038/nature20772

Ren, T., Amaral, J. A., & Knowles, R. (1997). The response of methane consumption by pure cultures of methanotrophic bacteria to oxygen. *Canadian Journal of Microbiology*, *43*(10), 925–928. https://doi.org/10.1139/m97-133

Rey, P. F., & Coltice, N. (2008). Neoarchean lithospheric strengthening and the coupling of Earth's geochemical reservoirs. *Geology*, *36*(8), 635–638. https://doi.org/10.1130/g25031a.1;

Ridgwell, A., Hargreaves, J. C., Edwards, N. R., Annan, J. D., Lenton, T. M., Marsh, R., et al. (2007). Marine geochemical data assimilation in an efficient Earth System Model of global biogeochemical cycling. *Biogeosciences*, *4*(1), 87–104. https://doi.org/10.5194/bg-4-87-2007

Rothman, D. H., Hayes, J. M., & Summons, R. E. (2003). Dynamics of the Neoproterozoic carbon cycle. *Proceedings of the National Academy of Sciences*, *100*(14), 8124–8129. https://doi.org/10.1073/pnas.0832439100

Rudnick, R. L., & Gao, S. (2003). Composition of the continental crust. *Treatise on Geochemistry*, *3*, 659.

Rushby, A. J., Johnson, M., Mills, B. J., Watson, A. J., & Claire, M. W. (2018). Long-term planetary habitability and the carbonate-silicate cycle. *Astrobiology*, *18*(5), 469–480. https://doi.org/10.1089/ast.2017.1693

Ruttenberg, K. C. (2003). The global phosphorus cycle. *Treatise on Geochemistry*, *8*, 682.

Sagan, C., & Chyba, C. (1997). The early faint sun paradox: Organic shielding of ultraviolet-labile greenhouse gases. *Science*, *276*(5316), 1217–1221. https://doi.org/10.1126/science.276.5316.1217

Sagan, C., & Mullen, G. (1972). Earth and Mars: Evolution of atmospheres and surface temperatures. *Science*, *177*(4043), 52–56. https://doi.org/10.1126/science.177.4043.52

Saito, M. A., Sigman, D. M., & Morel, F. M. (2003). The bioinorganic chemistry of the ancient ocean: The co-evolution of cyanobacterial metal requirements and biogeochemical cycles at the Archean–Proterozoic boundary? *Inorganica Chimica Acta*, *356*, 308–318. https://doi.org/10.1016/s0020-1693(03)00442-0

Sander, R. (2015). Compilation of Henry's law constants (version 4.0) for water as solvent. *Atmospheric Chemistry and Physics*, *15*(8), 4399–4981. https://doi.org/10.5194/acp-15-4399-2015

Sarmiento, J. L., & Gruber, N. (2006). *Ocean biogeochemical dynamics*. Princeton University Press.

Sauterey, B., Charnay, B., Affholder, A., Mazevet, S., & Ferrière, R. (2020). Co-evolution of primitive methane-cycling ecosystems and early Earth's atmosphere and climate. *Nature Communications*, *11*(1), 2705. https://doi.org/10.1038/s41467-020-16374-7

Schidlowski, M. (1988). A 3,800-million-year isotopic record of life from carbon in sedimentary rocks. *Nature*, *333*(6171), 313–318. https://doi.org/10.1038/333313a0

Schott, J., Berner, R. A., & Sjöberg, E. L. (1981). Mechanism of pyroxene and amphibole weathering—I. Experimental studies of iron-free minerals. *Geochimica et Cosmochimica Acta*, *45*(11), 2123–2135. https://doi.org/10.1016/0016-7037(81)90065-x

Schrag, D. P., Higgins, J. A., Macdonald, F. A., & Johnston, D. T. (2013). Authigenic carbonate and the history of the global carbon cycle. *Science*, *339*(6119), 540–543. https://doi.org/10.1126/science.1229578

Sleep, N. H., & Zahnle, K. (2001). Carbon dioxide cycling and implications for climate on ancient Earth. *Journal of Geophysical Research*, *106*(E1), 1373–1399. https://doi.org/10.1029/2000je001247

Sperling, E. A., Wolock, C. J., Morgan, A. S., Gill, B. C., Kunzmann, M., Halverson, G. P., et al. (2015). Statistical analysis of iron geochemical data suggests limited late Proterozoic oxygenation. *Nature*, *523*(7561), 451–454. https://doi.org/10.1038/nature14589

Swanner, E. D., Lambrecht, N., Wittkop, C., Harding, C., Katsev, S., Torgeson, J., & Poulton, S. W. (2020). The biogeochemistry of ferruginous lakes and past ferruginous oceans. *Earth-Science Reviews*, *211*, 103430. https://doi.org/10.1016/j.earscirev.2020.103430

Tajika, E., & Matsui, T. (1990). The evolution of the terrestrial environment. *Origin of the Earth*, *347*, 378.

Tajika, E., & Matsui, T. (1992). Evolution of terrestrial proto-CO_2 atmosphere coupled with thermal history of the earth. *Earth and Planetary Science Letters*, *113*(1–2), 251–266. https://doi.org/10.1016/0012-821x(92)90223-i

Talley, L. D. (2007). *Hydrographic Atlas of the World Ocean Circulation Experiment (WOCE): Volume 2: Pacific Ocean*. WOCE International Project Office.

Thompson, K. J., Kenward, P. A., Bauer, K. W., Warchola, T., Gauger, T., Martinez, R., et al. (2019). Photoferrotrophy, deposition of banded iron formations, and methane production in Archean oceans. *Science Advances*, *5*(11), eaav2869. https://doi.org/10.1126/sciadv.aav2869

Tiano, L., Garcia-Robledo, E., Dalsgaard, T., Devol, A. H., Ward, B. B., Ulloa, O., et al. (2014). Oxygen distribution and aerobic respiration in the north and south eastern tropical Pacific oxygen minimum zones. *Deep Sea Research Part I: Oceanographic Research Papers*, *94*, 173–183. https://doi.org/10.1016/j.dsr.2014.10.001

Treumann, R. A., LaBelle, J., & Bauer, T. M. (1995). Diffusion processes: An observational perspective. *Physics of the Magnetopause*, *90*, 331–341.

Tromp, T. K., Van Cappellen, P., & Key, R. M. (1995). A global model for the early diagenesis of organic carbon and organic phosphorus in marine sediments. *Geochimica et Cosmochimica Acta*, *59*(7), 1259–1284. https://doi.org/10.1016/0016-7037(95)00042-x

Tyrrell, T. (1999). The relative influences of nitrogen and phosphorus on oceanic primary production. *Nature*, *400*(6744), 525–531. https://doi.org/10.1038/22941

Van Cappellen, P., & Ingall, E. D. (1994). Benthic phosphorus regeneration, net primary production, and ocean anoxia: A model of the coupled marine biogeochemical cycles of carbon and phosphorus. *Paleoceanography*, *9*(5), 677–692. https://doi.org/10.1029/94pa01455

Voss, M., Bange, H. W., Dippner, J. W., Middelburg, J. J., Montoya, J. P., & Ward, B. (2013). The marine nitrogen cycle: Recent discoveries, uncertainties and the potential relevance of climate change. *Philosophical Transactions of the Royal Society B: Biological Sciences*, *368*(1621), 20130121. https://doi.org/10.1098/rstb.2013.0121

Walker, J. C. (1982). Climatic factors on the Archean Earth. *Palaeogeography, Palaeoclimatology, Palaeoecology*, *40*(1–3), 1–11. https://doi.org/10.1016/0031-0182(82)90082-7

Walker, J. C., Hays, P. B., & Kasting, J. F. (1981). A negative feedback mechanism for the long-term stabilization of Earth's surface temperature. *Journal of Geophysical Research*, *86*(C10), 9776–9782. https://doi.org/10.1029/jc086ic10p09776

Wallmann, K., & Aloisi, G. (2012). The global carbon cycle: Geological processes. *Fundamentals of Geobiology* (pp. 20–35).

Wallmann, K., Aloisi, G., Haeckel, M., Tishchenko, P., Pavlova, G., Greinert, J., et al. (2008). Silicate weathering in anoxic marine sediments. *Geochimica et Cosmochimica Acta*, *72*(12), 2895–2918. https://doi.org/10.1016/j.gca.2008.03.026

Warke, M. R., Di Rocco, T., Zerkle, A. L., Lepland, A., Prave, A. R., Martin, A. P., et al. (2020). The great oxidation event preceded a paleoproterozoic "snowball Earth". *Proceedings of the National Academy of Sciences*, *117*(24), 13314–13320. https://doi.org/10.1073/pnas.2003090117

Watanabe, Y., Tajika, E., & Ozaki, K. (2023). Biogeochemical transformations after the emergence of oxygenic photosynthesis and conditions for the first rise of atmospheric oxygen. *Geobiology*, *21*(5), 537–555. https://doi.org/10.1111/gbi.12554

Watson, A. J., & Orr, J. C. (2003). Carbon dioxide fluxes in the global ocean. In *Ocean biogeochemistry* (pp. 123–143). Springer.

Wedepohl, K. H. (1995). The composition of the continental crust. *Geochimica et Cosmochimica Acta*, *59*(7), 1217–1232. https://doi.org/10.1016/0016-7037(95)00038-2

West, A. J., Galy, A., & Bickle, M. (2005). Tectonic and climatic controls on silicate weathering. *Earth and Planetary Science Letters*, *235*(1–2), 211–228. https://doi.org/10.1016/j.epsl.2005.03.020

Wogelius, R. A., & Walther, J. V. (1992). Olivine dissolution kinetics at near-surface conditions. *Chemical Geology*, *97*(1–2), 101–112. https://doi.org/10.1016/0009-2541(92)90138-u

Wolf-Gladrow, D. A., Zeebe, R. E., Klaas, C., Körtzinger, A., & Dickson, A. G. (2007). Total alkalinity: The explicit conservative expression and its application to biogeochemical processes. *Marine Chemistry*, *106*(1–2), 287–300. https://doi.org/10.1016/j.marchem.2007.01.006

Wong, K., Mason, E., Brune, S., East, M., Edmonds, M., & Zahirovic, S. (2019). Deep carbon cycling over the past 200 million years: A review of fluxes in different tectonic settings. *Frontiers in Earth Science*, *7*, 263. https://doi.org/10.3389/feart.2019.00263

Yool, A., & Fasham, M. J. (2001). An examination of the "continental shelf pump" in an open ocean general circulation model. *Global Biogeochemical Cycles*, *15*(4), 831–844. https://doi.org/10.1029/2000gb001359

Zahnle, K. J., Gacesa, M., & Catling, D. C. (2019). Strange messenger: A new history of hydrogen on Earth, as told by Xenon. *Geochimica et Cosmochimica Acta*, *244*, 56–85. https://doi.org/10.1016/j.gca.2018.09.017

Zeebe, R. E. (2012). LOSCAR: Long-term ocean-atmosphere-sediment carbon cycle reservoir model v2. 0.4. *Geoscientific Model Development*, *5*(1), 149–166. https://doi.org/10.5194/gmd-5-149-2012

Zeebe, R. E., & Wolf-Gladrow, D. (2001). *CO_2 in seawater: Equilibrium, kinetics, isotopes*. Gulf Professional Publishing.

Zhang, S., Wang, X., Wang, H., Bjerrum, C. J., Hammarlund, E. U., Costa, M. M., et al. (2016). Sufficient oxygen for animal respiration 1,400 million years ago. *Proceedings of the National Academy of Sciences*, *113*(7), 1731–1736. https://doi.org/10.1073/pnas.1523449113